

Editor-in-Chief B.E.Paton

Editorial board:

Yu.S.Borisov	V.F.Khorunov
A.Ya.Ishchenko	I.V.Krivtsun
B.V.Khitrovskaya	L.M.Lobanov
V.I.Kirian	A.A.Mazur
S.I.Kuchuk	Yatsenko
Yu.N.Lankin	I.K.Pokhodnya
V.N.Lipodaev	V.D.Poznyakov
V.I.Makhnenko	K.A.Yushchenko
O.K.Nazarenko	A.T.Zelnichenko
I.A.Ryabtsev	

International editorial council:

N.P.Alyoshin	(Russia)
U.Diltey	(Germany)
Guan Qiao	(China)
D. von Hofe	(Germany)
V.I.Lysak	(Russia)
N.I.Nikiforov	(Russia)
B.E.Paton	(Ukraine)
Ya.Pilarczyk	(Poland)
P.Seyffarth	(Germany)
G.A.Turichin	(Russia)
Zhang Yanmin	(China)
A.S.Zubchenko	(Russia)

Promotion group:

V.N.Lipodaev, V.I.Lokteva
A.T.Zelnichenko (exec. director)

Translators:

A.A.Fomin, O.S.Kurochko,
I.N.Kutianova, T.K.Vasilenko
PE «Melnik A.M.»

Editor

N.A.Dmitrieva
Electron galley:
I.S.Batasheva, T.Yu.Snegiryova

Address:

E.O. Paton Electric Welding Institute,
International Association «Welding»,
11, Bozhenko str., 03680, Kyiv, Ukraine

Tel.: (38044) 287 67 57

Fax: (38044) 528 04 86

E-mail: journal@paton.kiev.ua

http://www.nas.gov.ua/pwj

State Registration Certificate
KV 4790 of 09.01.2001

Subscriptions:

\$324, 12 issues per year,
postage and packaging included.
Back issues available.

All rights reserved.

This publication and each of the articles
contained herein are protected by copyright.
Permission to reproduce material contained in
this journal must be obtained in writing from
the Publisher.

Copies of individual articles may be obtained
from the Publisher.

CONTENTS

SCIENTIFIC AND TECHNICAL

<i>Labur T.M., Taranova T.G., Grigorenko G.M. and Kostin V.A.</i> Influence of thermal conditions of welding on the features of crack initiation in the HAZ of joints of aluminium alloys V96 and V96tss	2
<i>Ryabtsev I.I., Kondratiev I.A., Kostin V.A., Novikova D.P., Bogajchuk I.L. and Babinets A.A.</i> Structure of phosphorus-containing deposited metal of the tool steel type	8
<i>Nosov D.G. and Razmyshlyayev A.D.</i> Effectiveness of application of combined magnetic fields in submerged-arc welding	16
<i>Alapati R. and Dwivedi D.K.</i> Microstructure and hardness of Al-Cu alloy (A2218) welded joints produced by GTAW	21
<i>Pashchenko V.N.</i> Effect of the composition of plasma air-gas mixture on parameters of the plasmatron jet	27

INDUSTRIAL

<i>Tsybulkin G.A.</i> Control of manipulation robot force action	32
<i>Ilyushenko V.M., Butakov G.A., Ganchuk A.V., Ostapchenko V.A. and Goryajnov N.A.</i> Comparative tests of welding-technological properties of inverter and thyristor power sources	34
<i>Reisgen U. and Olschok S.</i> Laser-submerged arc hybrid welding	38
<i>Dzykovich V.I.</i> Effect of the centrifugal thermal spraying process on properties of spherical tungsten carbide particles	43

BRIEF INFORMATION

<i>Murashov A.P., Demianov I.A., Grishchenko A.P., Burlachenko A.N. and Vigilyanskaya N.V.</i> Application of protective extension in thermal spraying of quasi-crystalline coatings	46
News	48

NEWS

Ukrainian-Belarusian Meeting-Presentation of the Technology of Live Tissue Welding	49
Developed at PWI	15



INFLUENCE OF THERMAL CONDITIONS OF WELDING ON THE FEATURES OF CRACK INITIATION IN THE HAZ OF JOINTS OF ALUMINIUM ALLOYS V96 AND V96tss

T.M. LABUR, T.G. TARANOVA, G.M. GRIGORENKO and V.A. KOSTIN
E.O. Paton Electric Welding Institute, NASU, Kiev, Ukraine

The influence of thermal impact in nonconsumable electrode and electron beam welding on the features of cracking in different sections of the HAZ of high-strength complex-alloyed aluminium alloys V96 and V96tss at off-center tension has been analyzed. It is shown that the used temperature-time parameters of the welding mode change the volume fraction of particles contained in the alloy, their dimensions, shape and morphology of inclusion location on the boundary between the grains have an essential influence on the local stressed state in the HAZ metal and determine the associated mechanism of fracture site initiation.

Keywords: *high-strength aluminium alloys, welding, nonconsumable electrode, electron beam, thermal impact, structure, heat-affected zone, off-center tension, crack initiation, fracture*

Development of aircraft construction is inseparably linked with application of new structural materials of an improved composition and mechanical properties, one of which is V96 alloy of Al–Zn–Mg–Cu alloying system. It was highly appreciated by specialists as a material allowing structure weight to be reduced without decreasing its rigidity, thus making it attractive for flying vehicle manufacture [1]. On the other hand, welded joints of this alloy are characterized by unsatisfactory ductile properties and low resistance to cold cracking in the HAZ of welded joints in fusion welding, which is associated with running of irreversible physico-chemical processes, accompanying the thermal cycle of fusion welding. The welded joint HAZ develops six characteristic structural sections, differing by grain and boundary dimensions, phase and inclusion composition [2–5]. Formation of final structures and physico-mechanical properties of the HAZ metal depend on decomposition kinetics of metastable phases and are determined by heat input into the used welding process [1].

V96 alloy mechanical properties are improved by adding scandium, which has a high (1814 K) melting temperature and minimum (3.05 N/m^3) specific weight [6–8]. Dispersed particles of Al_3Sc phase form not as a result of special strengthening treatment, but are a product of high-temperature decomposition of oversaturated solid solution of scandium in aluminium at melt solidification. Al_3Sc particles are coherent with the matrix, they are uniformly distributed in the grain bulk and preserve their stability at comparatively high temperature, and, thus, stabilize the structure and suppress recrystallization, which runs in the metal. The main factor, explaining the unique influence of scandium on the structure and properties of aluminium and aluminium alloys, is the dimensional-structural similarity of crystalline lattices of aluminium (4.405)

and Al_3Sc phase (4.407). Owing to such a similarity, Al_3Sc particles formed at initial solidification are effective grain nuclei, thus ensuring a maximum refinement of the cast grains (down to the dendrite cell size).

The mechanism of decomposition of aluminium solid solution, formed at weld metal solidification, is also determined by the principle of the above dimensional-structural similarity, namely the decomposition products (Al_3Sc particles) precipitate by the homogeneous mechanism. They feature a high density and short distance between the particles, respectively. Here, the strengthening and anti-recrystallization impact of scandium compared to other transition metals is noted.

To determine the causes for lowering of ductility of V96 alloy welded joints (wt. %: 2.3 Mg, 2.1 Cu, 8.1 Zn, 0.2 Zr), it is necessary to study the influence of thermal conditions of welding on the structural features of different HAZ sections, establish the mechanism of crack initiation in them, and compare it with similar sections of V96tss alloy of the same composition, but with scandium additives (0.3 wt. %). Presence of the latter in the alloy composition accelerates solid solution decomposition during thermal operations and promotes formation of finely-dispersed particles of intermetallic phases [5], which, being located in the grain bulk and along grain boundaries, strengthen the alloy and prevent metal recrystallization at heating during welding, while mechanical properties of the alloy are improved [8].

The purpose of this work is determination of the influence of structural and physical inhomogeneity found in the welded joint HAZ, on crack initiation in nonconsumable-electrode (TIG) and electron beam (EB) welding [5]. Scanning electron microscope JSM-840 with «Link-860/500» microanalyzer system (at accelerating voltage of 15, 20 and 30 kV) was used for investigations, allowing determination of the features of crack initiation and nature of damage of welded joints in the studied alloys.



Model samples were used to obtain a complete picture of structural changes in different sections of the HAZ of the studied alloy welded joints at TIG and EB welding. Samples were heated in a thermal furnace, creating the conditions for simulation of metal structure, which is formed in fusion welding in different sections of the HAZ: overheating ($T = 550\text{ }^{\circ}\text{C}$); quenching ($T = 460\text{ }^{\circ}\text{C}$); annealing ($T = 370\text{ }^{\circ}\text{C}$); short-term tempering ($T = 340\text{ }^{\circ}\text{C}$); ageing ($T = 140\text{ }^{\circ}\text{C}$). Samples were cooled at the rate of 10–20 and 30–50 $^{\circ}\text{C}/\text{s}$ in air and in water, thus corresponding to the conditions of metal cooling after TIG and EB welding. This allowed revealing the influence of structural features and ductility level of the metal of individual HAZ sections, as well as correlating the limit strain and stresses, accompanying crack initiation during testing. The obtained results were compared with similar ones for the base metal.

The most widely spread method of ductility evaluation is testing samples with deep notches, for instance, at off-center tension, simulating typical conditions of welded structure stressed state, when their tension and bending occur simultaneously [9, 10]. With such a loading pattern, the sample central part experiences monotonic deformation, which determines the start of the crack initiation process. In the limit state at sufficiently deep notches, the sample metal develops three-axial tension, as the stress level in the plastic flow zone depends on the notch tip radius. Ductility in individual sections of the HAZ of welded joints on V96 and V96tss alloys in different structural state, was studied using Kahn samples 3 mm thick with 11 mm depth of the notch and 0.1 mm radius in its tip (Figure 1). Such a notch geometry ensures crack initiation at a relatively low energy value, thus increasing the accuracy of its determination [10]. According to [9], the theoretical coefficient of stress concentration at the tip is equal to 10. Testing of five samples (in each studied structural state) was conducted at room temperature in an all-purpose RU-5 machine with the tension rate of 2 mm/min ($3.35 \cdot 10^{-5}\text{ m/s}$).

Load–deformation diagram generated using an oscillograph during testing (Figure 2) represents important moments of crack initiation and propagation up to complete fracture of the studied samples. It allows not only evaluation of stress intensity during plastic deformation under the conditions of off-center tension, but also determination of the duration of metal stable flow stage and the energy consumed at different stages of crack propagation. The curve in the individual sections of the diagram contains in the integral form the information on the condition of metal structure, which determines the processes of its plastic flow at sample deformation, stress increase and cracking.

Evaluation of ductility at uniaxial tension λ_t is traditionally performed using the characteristics of relative elongation δ and relative transverse reduction ψ [10]. Ductility is expressed through value δ as follows:

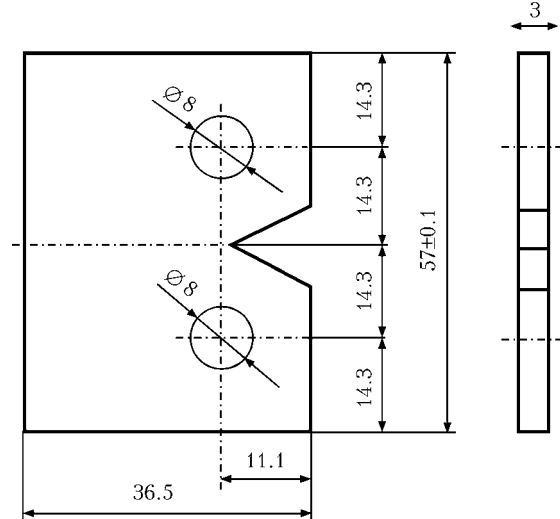


Figure 1. Schematic of a sample of welded joints of high-strength aluminium alloys V96 and V96tss for testing at off-center tension

$$\lambda_t = 1.73 \ln [100 / (100 - \delta)].$$

Under the conditions of non-uniform tension value ψ is used:

$$\lambda_t = 1.73 \ln [100 / (100 - \psi)].$$

Lowering of rigidity of the stressed state in the notch tip at its opening during testing may lead to an incorrect determination of the level of metal relative ductility. In this connection the data on ductility characteristics of the studied alloys V96 and V96tss after thermal impact were obtained using the ratio of stress and strain values (Figure 2). Based on the above approaches, they may be presented for δ and ψ evaluation in the form of a function of plastic deformation change under off-center tension of the studied samples:

$$(f_{\max} - f_y) / f_{\max} \cdot 100 \%,$$

where f_{\max} is the total (maximum) deformation at the avalanche crack formation; f_y is the deformation corresponding to 0.2 % stress, which is conditionally taken to be the yield point of the metal in the studied HAZ sections. In this case, ductility values λ_t were calculated by the following formula:

$$\lambda_t = 1.73 \ln \{100 / [100 - (f_{\max} - f_y) / f_{\max} \cdot 100 \%]\}.$$

Figure 2 combines the load–deformation diagram of the studied alloys with the fractograph of the fracture section of metal plastic deformation zone under the notch tip. Point A corresponds to the start of microcrack initiation in alloys V96 and V96tss, point B — to final coalescence of microcracks into a macrocrack, point C denotes a region, in which spontaneous propagation of the main crack occurs up to complete fracture of the sample.

It should be noted that the plastic deformation zone under the notch tip (see Figure 2) is the initial stage of the main crack initiation. As follows from [11–14], the influence of alloy structure on its performance and mechanical properties is manifested indirectly, as the material structural sensitivity can be

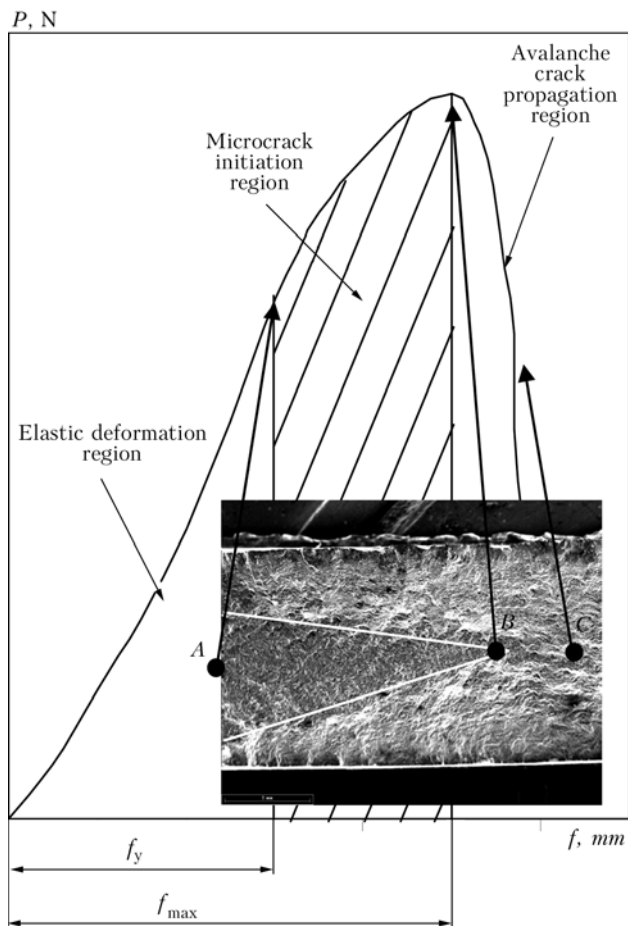


Figure 2. Load–deformation diagram (P – f) derived under the conditions of off-center tension of the studied samples and fractograph of fracture section (plastic deformation zone marked by a triangle is located under the notch tip) ($\times 27$)

described by a ratio of the extent of this zone to the dimensions of structural components. Essential differences of geometrical dimensions of the plastic deformation zone in the studied samples are indicative of the ambiguity of the metal initial stressed state under the same testing conditions.

Analysis of the obtained results showed (Figure 3, *b*, *d*) that welded joints of V96tss alloy produced by EBW differ by a higher susceptibility to plastic deformation (from 81 to 89 %) compared to V96 alloy (53–91 %). Microcrack initiation occurs both by the tough mechanism, and by shear fracture. Metal structure formed at fracture is determined by grain size and inclusion spacing. Proceeding from the available results, V96tss alloy features a greater (1.5 times) force of adhesion of elementary particles.

A similar dependence is also observed in welded joints produced by TIG welding (Figure 3, *a*, *c*). With this welding process, V96tss alloy is also characterized by a more pronounced susceptibility to plastic deformation (from 80 to 89 %) than V96 alloy (53–94 %). As is seen from Figure 2, V96tss alloy, irrespective of the welding process, has an area (hatched) of preservation of plastic deformation. Ductility of V96tss alloy in the studied HAZ sections, where the process of welding heating is accompanied by high temperatures,

is determined by migration of grain boundaries, changes of inclusion shape, recrystallization phenomena and activation of grain boundary slipping, the degree of manifestation of which is connected with the presence of scandium, alongside the temperature-time conditions.

Regularities found in V96 alloy are different. An essential dependence of welded joint metal structure on the temperature-time parameters of the welding mode is revealed. With both the welding processes V96 alloy shows a lowering of ductility in the overheated and annealed sections. Long-term heating of metal at TIG welding influences the increase of the intergranular space due to precipitation of elements from the grain and subsequent formation of eutectic-type compounds in it [6, 8]. This leads to ductility lowering as a result of eutectic formation along the grain boundaries (see Figure 3, *a*). At EBW under the conditions of a short-term heat application phase transformations do not have enough time to develop, so that only dissolution of low-melting compounds located near the grain boundaries, occurs (Figure 3, *b*, *d*). In this case, the nature of inclusion distribution has a strong influence on ductility.

Figure 3, *c*, *d* shows a decrease of strength properties of both the alloys with the two welding processes, that may be due to non-uniformity of inclusion distribution, differences in their shape and dimensions. Strength lowering is observed to a greater degree in alloy V96tss, which is related to the presence of coarse insoluble inclusions in the HAZ metal structure. Their refinement during semi-finished product fabrication will promote an improvement of the alloy strength with preservation of its ductility.

Fractographic analysis of fractures of broken samples simulating different sections of the HAZ of welded joints on V96 and V96tss alloys was performed to reveal crack initiation sites. Obtained results showed that thermal conditions of welding cause particle growth and phase formation, this way determining the nature of crack initiation in the studied alloys (Figures 4, 5). At testing the ductile matrix deforms with increase of tensile stresses, thus leading to an increase of stress gradient in the sections located at grain boundaries, as well as in inclusion sections in the intergranular spacing. The weaker particles crack, forming microcracks, the length of which does not exceed particle size.

According to the obtained experimental results, the length and quantity of embryo microcracks, as well as the nature of local stress are caused by a change of the dimensions of particles precipitating at welding heating, as well as their volume fraction in relation to other structural components. As the notch radius in the samples is the same ($R = 0.1$ mm), there is ground to state that the size of the plastic deformation zone, and, therefore, also the ductility of the studied samples, are determined by local stresses related to the thermal conditions of heating and cooling in welding. The source of crack initiation are particles, located

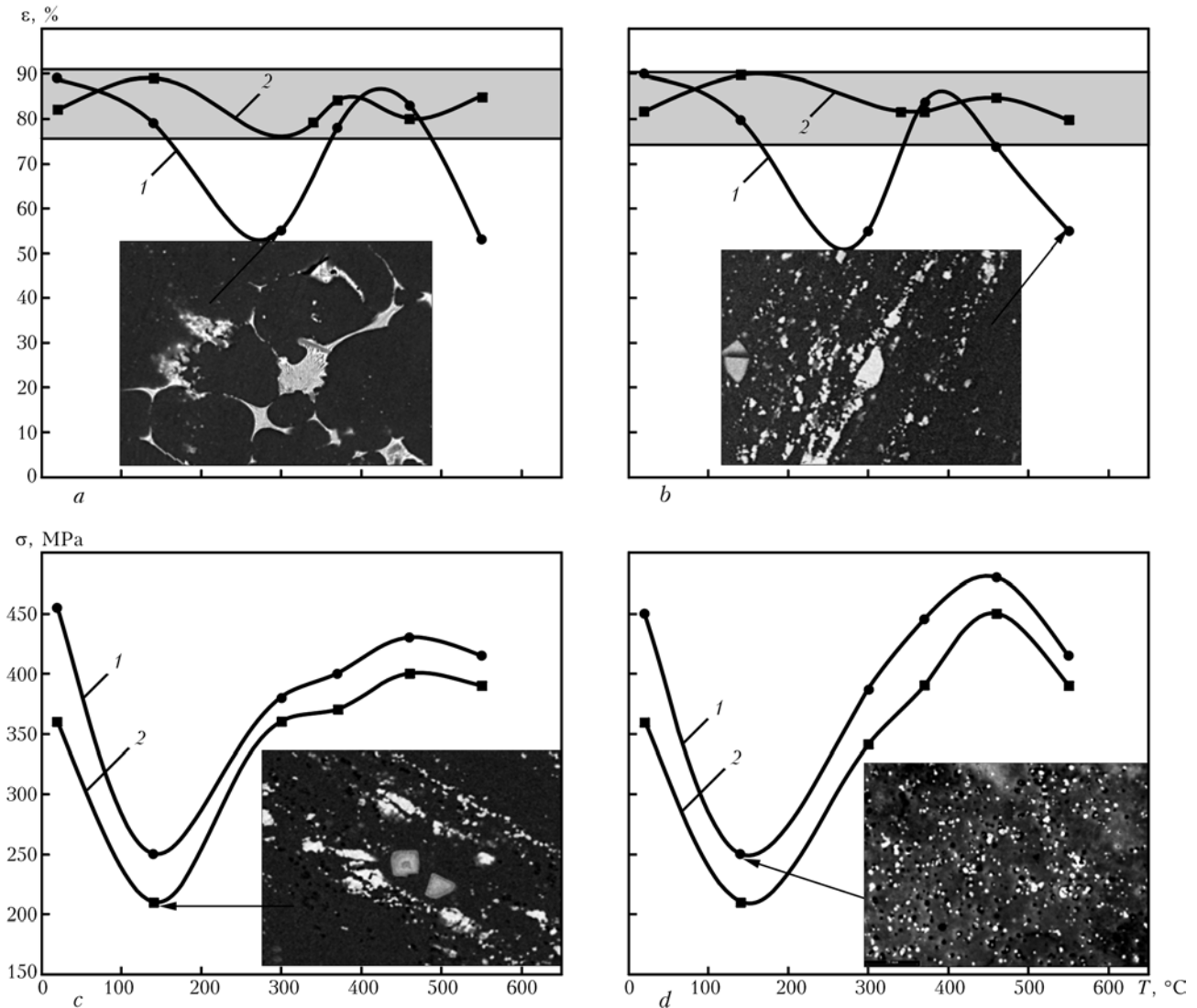


Figure 3. Influence of heating conditions at TIG (*a, b*) and EB (*b, d*) welding on ductility (*a, b*) and strength (*c, d*) of HAZ metal of welded joints of V96 (*1*) and V96tss (*2*) alloys

along the grain boundaries. During fracture irregular particles crack, and the round ones delaminate (Figure 4).

In V96tss alloy the plastic deformation zone is readily revealed, and in V96 alloy the boundary contour is blurred, being indicative of a more brittle state of metal structure. In the region of high (550 °C) homologous temperatures, simulating the conditions of metal overheating on the boundary of the weld fusion with the base metal, high values of the relative ductility index ($\lambda_t = 81\%$) of V96tss alloy are due to dissolution of structural elements located in the intergranular space, and formation of a uniform liquid phase (Figure 5, *b, d, f*). This is attributable to the presence of phases on the intergranular boundaries, which contain sufficiently strong elements (manganese, chromium, zirconium, scandium), causing microcrack slowing down. A considerable (from 2.8 to 5.0 mm) extent of the plastic deformation zone of V96tss alloy is indicative of its susceptibility to active plastic deformation at microcrack initiation. Presence of pits, forming near the inclusions through initiation

and growth of pores, allows this alloy to be characterized as tough, although the fracture surface also shows brittle fracture fragments (Figure 5, *II*). At the temperature of 460 °C the alloying elements go into the solid solution [6]. Relative ductility index of V96tss alloy preserves its values.

Shortening of the plastic deformation zone to 2.0 and 1.7 mm is found in samples in the initial condition and after artificial ageing, respectively, which is indicative of a greater metal brittleness and development of conditions for the action of elastic deformation, as the relaxed energy is insufficient for realization of plastic deformation. Crack initiation sites appear near the coarse inclusions. Crack extent increases as the local stress on the grain boundary grows. Formation of finely dispersed particles of metastable phases as a result of partial decomposition of the solid solution leads to formation of a structure, containing intermediate compounds, differing by their crystallographic structure from the solid solution and equilibrium phases. Their volume fraction in the structure depends on the heated metal cooling rate. Both inclusion sepa-

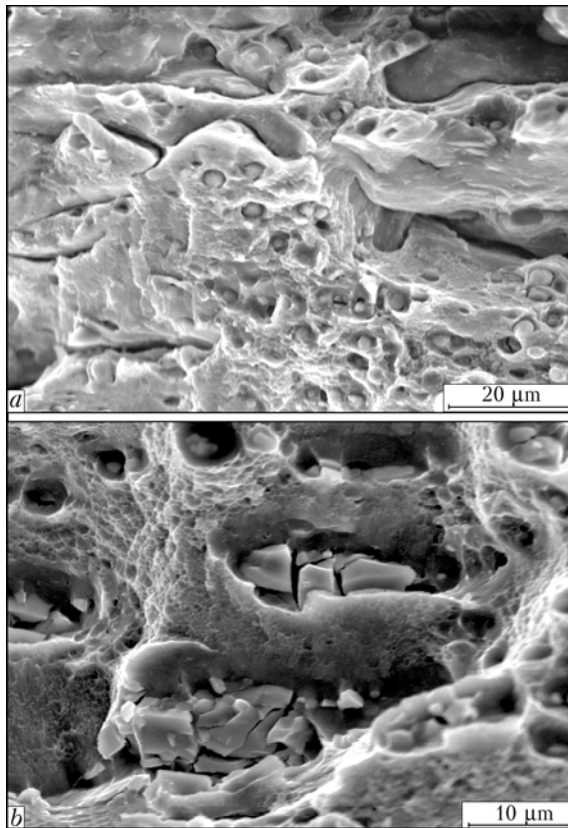


Figure 4. Fractographs of crack initiation sites at fracture of alloys V96 (a) and V96tss (b)

ration along the boundary with the matrix and delamination of primary inclusions containing modifiers, i.e. zirconium and scandium, are observed on the fracture surface of V96tss alloy. The non-uniform dimensions of microvoids formed at cracking of the coarse inclusions point to a step-by-step development of fracture of the studied alloys during plastic deformation of the matrix up to the moment when the microcrack length has reached a critical size. Local stress causing microcrack initiation on the boundary between the grains, depends on the dimensions of the low-melting eutectic in the intergranular space and matrix capability to deform near the inclusion under the influence of the thermal cycle of welding.

Fracture pattern of V96 alloy samples is different. It is characterized by smaller ductility values ($\lambda_t = 53\%$), which is attributable to a variable solubility of phases as a result of the absence of scandium additives in the alloy (Figure 5, a, c, e). The extent of the plastic deformation zone varies in the range from 1 to 3 mm. In the metal overheated condition this zone is not clear-cut, that may be due to presence of tangential stresses at fracture. No grain boundaries are manifested in the fracture section, but microcracks having the same direction and normal to the fracture surface are visible. The magnitudes of stresses which should be applied during initial microcrack initiation

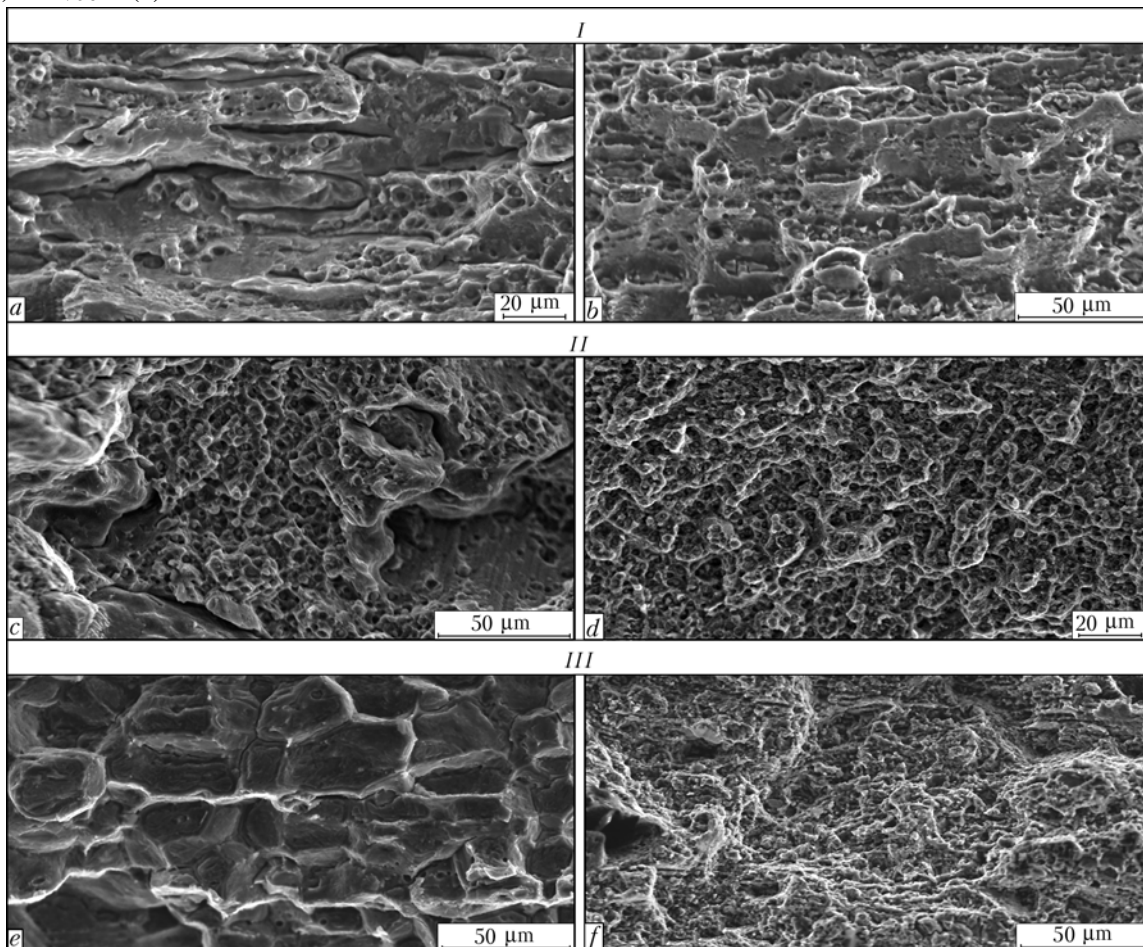


Figure 5. Fractographs of fracture sections of V96 (a, c, e) and V96tss (b, d, f) samples derived at overheating (I), after annealing (II) and tempering (III)



in V96tss alloy, are much smaller after welding heating compared to the initial condition of the base metal.

In fractures of V96 alloy samples heated up to 460 °C, the fracture surface is similar to that of V96tss alloy. The relative ductility index preserves its values only after TIG welding. Formation of disperse precipitates, smaller scatter of their dimensions, as well as lower content of solid solution decomposition products along the boundaries and in the grain bulk at EBW, promote a 1.5 times increase of V96 alloy ductility compared to the cooling rate at TIG welding. After quenching and cooling in water the plastic deformation zone is equal to 1 mm, and after cooling in air it is 2 mm. In as-annealed and as-tempered condition plastic deformation develops slowly (0.8–1.5 mm). However, an oblique fracture forms at complete fracture of such samples in the shear mode. This may be caused by grain softening and simultaneous embrittlement of the low-melting component in the intergranular space under thermal impact. It is indicated by the characteristic location of cracks along the grain boundaries, where low-melting eutectics form during welding heating, the presence of which lowers the ductility index (see Figure 3). A slight (up to 2 mm) increase of plastic deformation zone is noted in base metal samples in the initial and as-aged condition. Sample fracture proceeds by the mechanism of normal tear with formation of straight fracture.

CONCLUSIONS

1. A dependence is established between the nature of crack initiation in the HAZ at fracture under the conditions of off-center tension of high-strength complex-alloyed aluminium alloys V96 and V96tss and degree of thermal impact at TIG and EB welding.

2. Scandium additive (0.2–0.4 wt.%) to V96 alloy allows preserving the HAZ metal ductile properties owing to formation of fine intermetallic precipitates of strengthening particles, which slow down embrittlement of eutectic interlayer at annealing at $T = 360$ °C, and coagulation of non-metallic inclusions.

3. Microcracks initiate on coarse inclusions with increase of local stress on grain boundary. Inclusion separation along the boundary with the matrix is found on the studied alloy fracture surface, and in V96tss

alloy --- delamination of primary inclusions, containing modifiers, namely zirconium and scandium. Non-uniform dimensions of microvoids, formed at cracking of coarse phase inclusions, are indicative of step-by-step nature of their fracture during plastic deformation of the matrix up to the moment, when microcrack length has reached a critical size. Local stress, which causes microcrack initiation on the boundary between the grains, depends on dimensions of low-melting eutectic in the intergranular space and matrix capability to deform near the inclusion under the influence of thermal cycle of welding.

1. (1998) *Welding in aircraft construction*. Ed. by B.E. Paton. Kiev: MIIVTs.
2. Ishchenko, A.Ya., Labur, T.M. (1999) *Weldable aluminium alloys with scandium*. Kiev: MIIVTs.
3. Labur, T.M., Taranova, T.G., Kostin, V.A. et al. (2006) Influence of structural transformations in welding of aluminium alloy V96 on fracture resistance parameters. *The Paton Welding J.*, **11**, 17–21.
4. Labur, T.M., Taranova, T.G., Kostin, V.A. et al. (2007) Nature of fracture of V96 alloy depending on heating conditions in welding. *Ibid.*, **2**, 9–15.
5. Labur, T.M., Ishchenko, A.Ya., Taranova, T.G. et al. (1997) Influence of thermophysical conditions of welding on fracture resistance of the HAZ metal in the joints of aluminium alloy V96tss. *Ibid.*, **4**, 25–30.
6. Berezina, A.L., Monastyrskaya, T.A., Chekh, E. et al. (1997) Comparative analysis of the effectiveness of Al₃Sc and Al₃Zr particles in Al–Mg alloys. *Metallfizika i Nov. Tekhnologii*, **19**(9), 22–31.
7. Elagin, V.I., Zakharov, V.V., Rostova, T.D. (1994) Effect of scandium on structure and properties of alloy Al–5.5 % Zr–2.0 % Mg. *Metallovedenie i Term. Obrab. Metallov*, **7**, 25–27.
8. Fujikawa, S. (1999) Scandium in pure aluminum and aluminum alloys --- its behavior and addition effects. *J. Japan Institute of Light Metals*, **49**(3), 361–365.
9. Davidenkov, N.N. (1981) *Mechanical properties of materials and methods of measurement of deformations*. Vol. 2. Kiev: Naukova Dumka.
10. (1977) *Plasticity and fracture*. Ed. by V.L. Kolmogorov. Moscow: Metallurgiya.
11. Klevtsov, G.V. (1993) Kinetics of formation of plastic deformation zones near the crack tip in fracture of structural materials in the plane stressed state and at plane deformation. *Problemy Prochnosti*, **4**, 57–63.
12. Gordeeva, T.A., Zhegina, I.P. (1978) *Analysis of ruptures in evaluation of material reliability*. Moscow: Mashinostroenie.
13. Ivanova, V.S., Kudryashov, V.G., Shtovba, Yu.K. et al. (1974) Fractography and toughness of aluminium and titanium alloys. *Tekhnologiya Lyog. Splavov*, **3**, 65–70.
14. (1982) *Fractography and atlas of fractographs*: Refer. Book. Moscow: Metallurgiya.



STRUCTURE OF PHOSPHORUS-CONTAINING DEPOSITED METAL OF THE TOOL STEEL TYPE

I.I. RYABTSEV, I.A. KONDRATIEV, V.A. KOSTIN, D.P. NOVIKOVA, I.L. BOGAJCHUK and A.A. BABINETS
E.O. Paton Electric Welding Institute, NASU, Kiev, Ukraine

Peculiarities of structure of the deposited metal of the type of tool steels 30Kh4V2M2FS, 30Kh2M2NSGF and 35V9Kh3GSF, alloyed with 0–1.5 wt.% P, were investigated. Complex phosphides of the globular shape, containing vanadium, molybdenum, chromium, manganese and tungsten, i.e. metals the phosphides of which exhibit the highest thermodynamic stability, were found to form in the high-alloy deposited metal. The presence of such phosphides does not deteriorate crack resistance of the investigated types of the deposited metal.

Keywords: arc cladding, high-alloy deposited metal, phosphorus alloying, microstructure, X-ray microanalysis, phosphides, phosphide eutectics, crack resistance

Perspective of application of phosphorus as an alloying element in low-alloy cladding consumables, which are used for repair and hardening of parts working in conditions of the metal to metal friction at room temperature is shown in studies [1, 2]. The presence of phosphorus in these materials increases their wear resistance and reduces the coefficient of sliding friction. The insufficient level of knowledge of the phosphorus effect on structure and properties of cladding consumables, as well as the common opinion on its negative influence on crack resistance of the welds, though metals with a phosphorus content of not higher than 0.05 wt.% [3, 4] are considered, prevent the application of phosphorus as an alloying element in the cladding consumables. However, as determined in study [5], up to 1 wt.% P can dissolve in low-alloy deposited metal, and free phosphides in the form of boundary phosphide eutectics, which are the major reason of crack formation, are absent in structure of the deposited metal. At the same time, the presence in its structure of a small amount of globular refractory phosphides is acceptable.

This study presents results of investigations of the phosphorus influence on structure of the metal deposited with PP-Np-30Kh4V2M2FS, PP-Np-30Kh2M2NSGF and PP-Np-35V9Kh3FSG high-alloy flux-cored wires. These wires are used for repair and hardening of tools for hot and cold deforming of metals and alloys [6]. The distribution of phosphorus between structural components of a high-alloy deposited metal was also investigated. The aim of the present study is to determine the limits of phosphorus alloying of the deposited metal of chosen alloying systems, within which the low-melting point boundary phosphide eutectics are absent in structure of the deposited metal, and no cracks are formed in it.

12 flux-cored wires of 2 mm diameter (4 of each grade) were manufactured to carry out the investigations. The content of phosphorus in the deposited metal of each type was varied within a range of 0–

1.5 wt.%. Samples to measure hardness and chemical composition of the deposited metal (Table 1), as well as for microstructure and X-ray microanalysis, were deposited by the submerged arc method using experimental wires and flux AN-26. The cladding mode was as follows: $I = 250\text{--}270$ A; $U_a = 24\text{--}26$ V; $v_c = 28$ m/h. The data given in Table 1 show that, in contrast to a low-carbon low-alloy deposited metal [2], phosphorus has almost no influence on hardness of the carbon high-alloy deposited metal, carbon exerting the main effect on it.

Microstructure of the deposited metal samples of 12 compositions was examined. It is known that structure of the high-alloy deposited metal in many respects depends on the cladding thermal cycle. Therefore, continuous cooling transformation (CCT) diagrams of austenite decomposition in 30Kh4V2M2FC, 30Kh2M2NSGF and 35V9Kh3GSF deposited metals were used for analysis of structural state of these materials [7–9].

As stated in study [7], bainite and martensite transformations take place in deposited metal 30X4V2M2FC in a wide range of cooling rates, which do not occur to the end during the cladding thermal cycles, owing to which retained austenite persists in structure of the deposited metal.

In accordance with this, microstructure of the phosphorus-free deposited metal 30Kh4V2M2FS (Figure 1, *a*; sample No. 1, Table 1) is a martensite-bainite mixture (microhardness $HV_{0.5}$ 3860 MPa) and retained austenite ($HV_{0.5}$ 2320 MPa).

At alloying deposited metal 30Kh4V2M2FS with 0.45 wt.% P (sample No.2, Table 1), microhardness of martensite increases to $HV_{0.5}$ 4120 MPa, and that of retained austenite grows to $HV_{0.5}$ 257 MPa. Some increase of microhardness is likely to be related to dissolution of phosphorus in structural components of the deposited metal (Figure 1, *b*).

In deposited metal 30Kh4V2M2FS, containing 0.93 wt.% P (sample No. 3, Table 1), microhardness of retained austenite increases to $HV_{0.5}$ 3860 MPa, and that of the martensite regions — up to $HV_{0.5}$ 4730–5090 MPa. Deep-etching inclusions of different



Table 1. Chemical composition (wt.%) and hardness *HRC* of the metal deposited with experimental flux-cored wires

Type of deposited metal	Sample No.	C	Mn	Si	P	Cr	Mo	W	Ni	V	<i>HRC</i>
30Kh4V2M2FC	1	0.30	0.98	0.83	--	4.31	2.14	2.32	--	0.37	53–56
	2	0.29	1.18	1.12	0.45	3.94	2.35	1.95	--	0.45	53–56
	3	0.33	1.05	0.97	0.93	4.17	2.43	2.14	--	0.29	55–57
	4	0.28	0.93	1.02	1.52	4.35	2.15	1.89	--	0.42	53–55
30Kh2M2NSGF	5	0.24	0.97	0.81	--	2.29	1.92	--	1.20	0.43	51–52
	6	0.28	0.89	0.62	0.57	1.98	2.11	--	0.96	0.37	53–55
	7	0.27	0.92	0.76	0.89	2.13	2.01	--	1.03	0.52	49–51
	8	0.31	0.78	0.83	1.42	2.32	1.99	--	0.93	0.47	57–59
35V9Kh3GSF	9	0.33	1.08	0.63	--	2.56	--	9.17	--	0.36	53–54
	10	0.35	0.96	0.75	0.47	2.31	--	8.93	--	0.52	53–55
	11	0.30	0.98	0.73	1.02	2.85	--	8.97	--	0.47	51–53
	12	0.27	1.02	0.81	1.39	2.43	--	9.21	--	0.42	46–50

sizes occur in structure of the deposited layer on sample No. 3 (Figure 1, *c*).

With increase in the content of phosphorus to 1.52 wt.% (sample No. 4, Table 1), deposited metal 30Kh4V2M2FC has a cellular structure (microhardness *HV*0.5 3030 MPa). Fringes, in which phosphide inclusions are situated, are formed along the cell boundaries (microhardness *HV*0.5 4120 MPa) (Figure 1, *d*).

Analysis of the CCT diagram of deposited metal 30Kh2M2NSGF [8] shows that in a range of the cooling rates corresponding to the cladding thermal cycle, at first bainite and then martensite transformation takes place. Deposited metal 30Kh2M2NSGF is characterized by a high (390 °C) temperature of beginning of the martensite transformation. Because of a significant cooling rate during cladding the martensite trans-

formation is not completed, and retained austenite persists in structure of the deposited metal. Hence, microstructure of the phosphorus-free deposited metal 30Kh2M2NSGF (Figure 2, *a*; sample No.5, Table 1) is a martensite-bainite mixture (microhardness *HV*0.5 3030 MPa) with different crystallographic axes falling on the section surface (light- and dark-colored needles have similar hardness). Retained austenite is also present in structure of this metal (microhardness *HV*0.5 2290 MPa).

At a phosphorus content of 0.57 wt.% in deposited metal 30Kh2M2NSGF (sample No. 6, Table 1), its martensite-bainite structure coarsens, and its microhardness increases to *HV*0.5 3860–4410 MPa. The volume content of austenite remains approximately at the same level. Light-colored compact inclusions of a developed shape, which were preliminarily identified

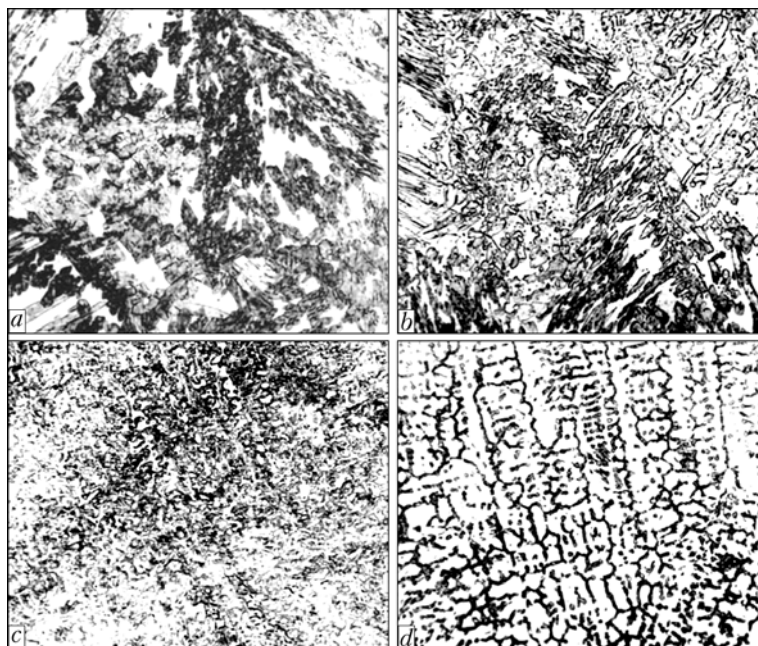


Figure 1. Microstructure (×200) of samples of deposited metal 30Kh4V2M2FS without phosphorus (*a*) and with 0.45 (*b*), 0.93 (*c*) and 1.52 wt.% P (*d*) (here, and also in Figures 2 and 3 --- electrolytic etching in chromic acid)

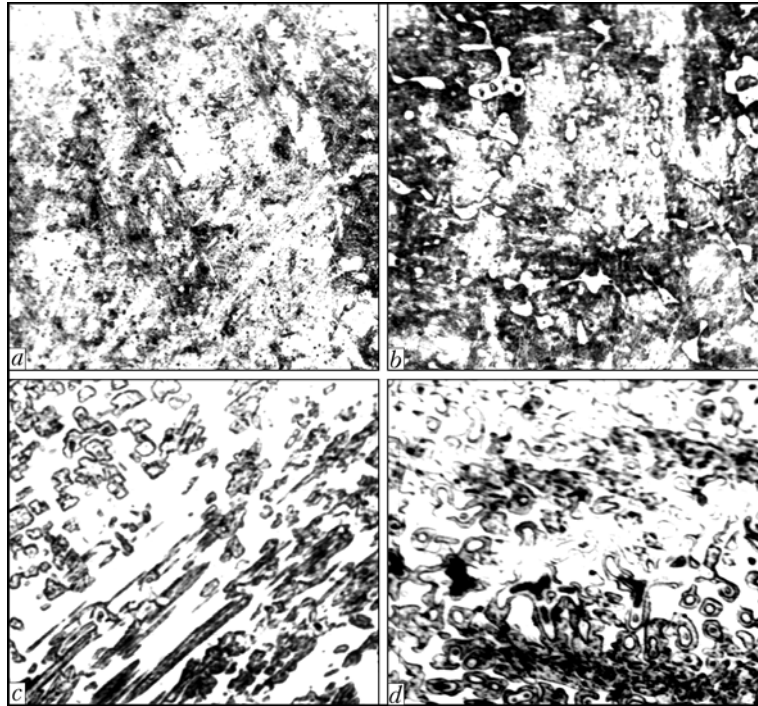


Figure 2. Microstructure ($\times 200$) of samples of deposited metal 30Kh2M2NSGF without phosphorus (*a*) and with 0.57 (*b*), 0.89 (*c*) and 1.42 wt.% P (*d*)

as δ -ferrite, also occur in structure of the deposited metal (Figure 2, *b*).

Structure of deposited metal 30Kh2M2NSGF with 0.89 wt.% P (sample No.7, Table 1) contains martensite, bainite and retained austenite (Figure 2, *c*). Microhardness of the martensite-bainite component is $HV_{0.5}$ 4120 MPa, and that of retained austenite is $HV_{0.5}$ 3210 MPa.

With further increase in the content of phosphorus to 1.42 wt.% (sample No.8, Table 1), microhardness of retained austenite grows to $HV_{0.5}$ 3620 MPa. The

martensite-bainite component has microhardness $HV_{0.5}$ 5490 MPa. The chains of phosphides form, and microcracks propagating from phosphide to phosphide initiate in structure of the deposited metal (Figure 2, *d*).

As follows from the CCT diagram, structure of deposited metal 35B9Kh3GSF at a cooling rate corresponding to cladding thermal cycle, must consist of acicular troostite, martensite, retained austenite and carbides [9]. At slow cooling characteristic of isothermal annealing, occurrence of ferrite is possible in

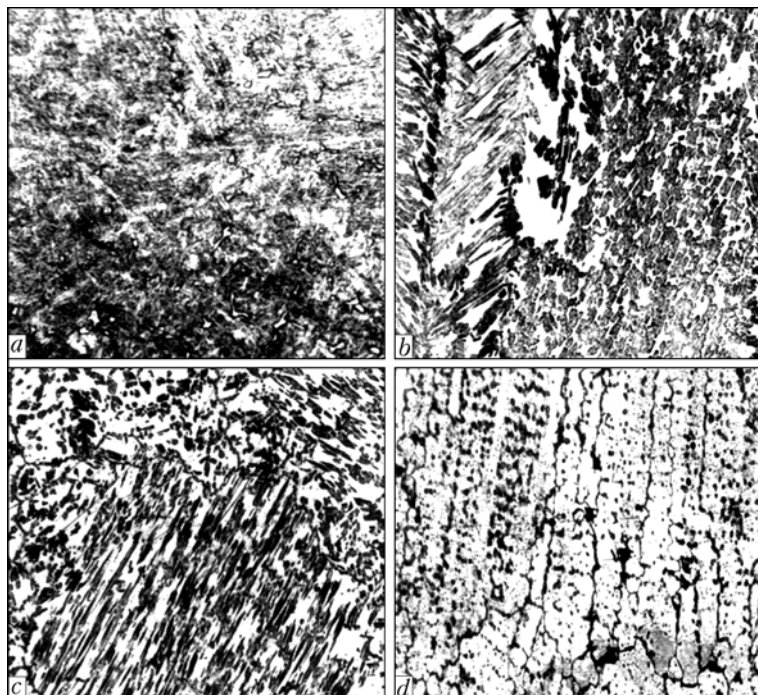


Figure 3. Microstructure ($\times 200$) of samples of deposited metal 35V9Kh3GSF without phosphorus (*a*) and with 0.47 (*b*), 1.02 (*c*) and 1.39 wt.% P (*d*)

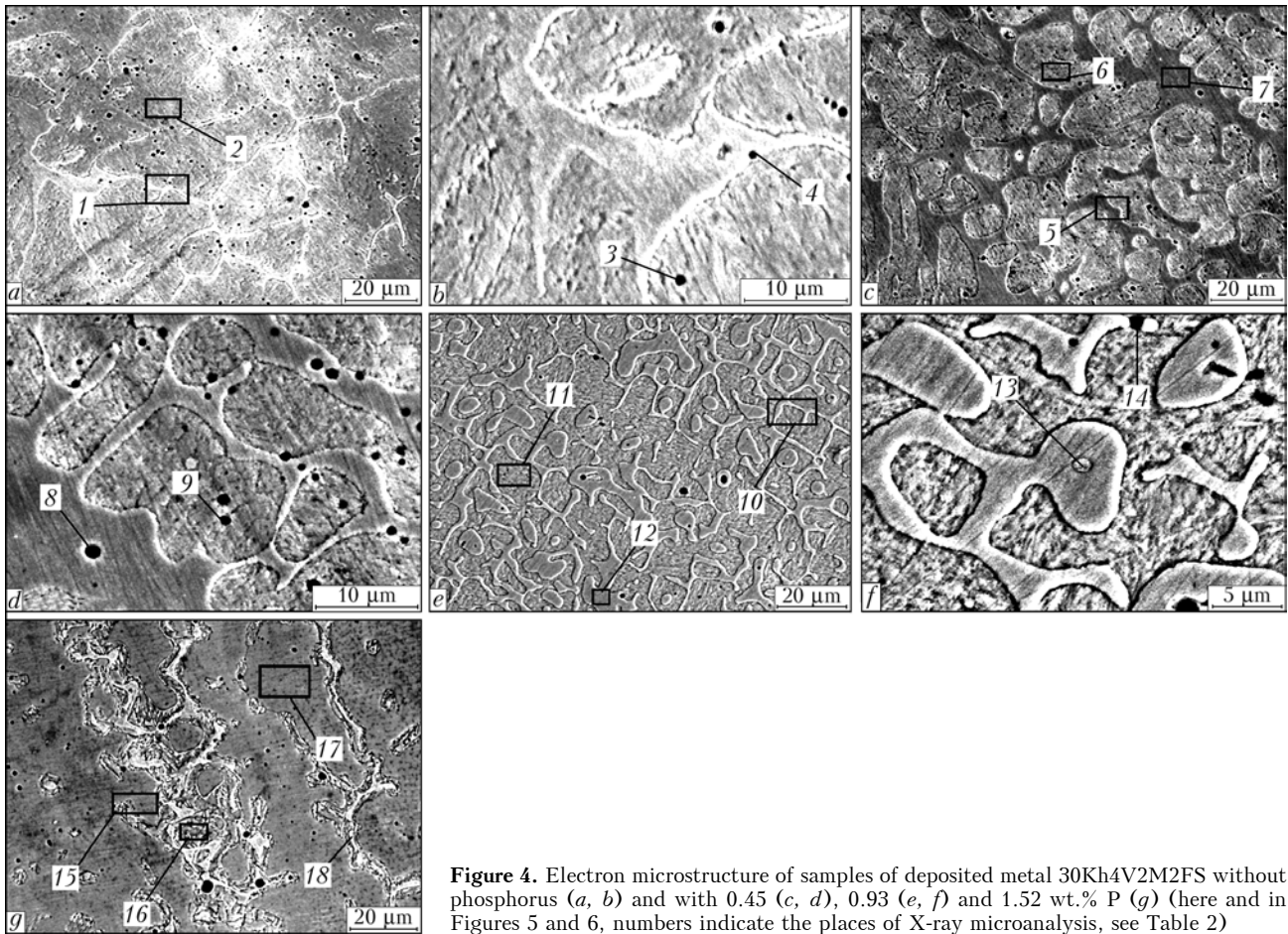


Figure 4. Electron microstructure of samples of deposited metal 30Kh4V2M2FS without phosphorus (*a, b*) and with 0.45 (*c, d*), 0.93 (*e, f*) and 1.52 wt.% P (*g*) (here and in Figures 5 and 6, numbers indicate the places of X-ray microanalysis, see Table 2)

structure of deposited metal 35V9Kh3GSF. This type of metal is also characterized by a high (410 °C) temperature of beginning of martensite transformation.

Structure of phosphorus-free deposited metal 35V9Kh3GSF (sample No. 9, Table 1) is a martensite-troostite mixture, having microhardness $HV_{0.5}$ 4730 MPa, the needles being oriented mainly at an angle of 60° (Figure 3, *a*). The regions of retained austenite ($HV_{0.5}$ 3620 MPa) and carbides inclusions are formed.

Structure of deposited metal 35V9Kh3GSF containing 0.47 wt.% P (sample No. 10, Table 1) is similar to that of sample No. 9 (Figure 3, *b*). Microhardness of the martensite-troostite matrix is $HV_{0.5}$ 4730 MPa, and that of retained austenite is $HV_{0.5}$ 3860 MPa.

Increasing phosphorus content up to 1.02 wt.% in deposited metal 35V9Kh3GSF (sample No. 11, Table 1) the structure consisting of martensite, acicular troostite and retained austenite is remained. Microhardness of martensite and austenite is kept at the same level. Circular inclusions, possibly, phosphides, were detected in the separate regions of the structure of deposited metal (Figure 3, *c*).

Deposited metal 35V9Kh3GSF with a phosphorus content of 1.39 wt.% has a cellular structure (Figure 3, *d*; sample No. 12, Table 1), in which the inclusions of carbides and, probably, phosphides are presented. Formation of microcracks was also fixed.

The distribution of the main alloying elements and, first of all, phosphorus in structure of the deposited metal of all samples (Figures 4–6, Tables 2–5) was investigated by means of X-ray microanalysis. The integrated analysis covered a region of several tens of micrometers, which allowed determining the composition of matrix of the deposited metal and its structure components. The point by point analysis was carried out in a region of 1 μm diameter, primarily, for detection of different inclusions.

The results of X-ray microanalysis show that the deposited metal of all alloying systems has a sufficiently high chemical microheterogeneity for certain elements. Thus, in phosphorus-free deposited metal 30Kh4V2M2FS, heterogeneity for silicon and tungsten was detected (Figure 4, *a, b*; Nos. 1–4, Table 2), in 30Kh2M2NSGF — for silicon and nickel (Figure 5, *a*; Nos. 1–3, Table 3), and in 35V9Kh3GSF — for tungsten and vanadium (Figure 6, *a*; Nos. 1, 2, Table 4).

Alloying of the deposited metal with phosphorus (0.5 wt.%) reduces to some extent the chemical microheterogeneity for these elements. In such a case heterogeneity in deposited metal 30Kh4V2M2FS was fixed only for tungsten (Figure 4, *c, d*; Nos. 5–9, Table 2), in 30Kh2M2NSGF — only for nickel (Figure 5, *b*; Nos. 4–6, Table 3), and in 35V9Kh3GSF — only for silicon (Figure 6, *b, c*; Nos. 4–7, Table 4). Phosphorus is in solid solution in almost all structural

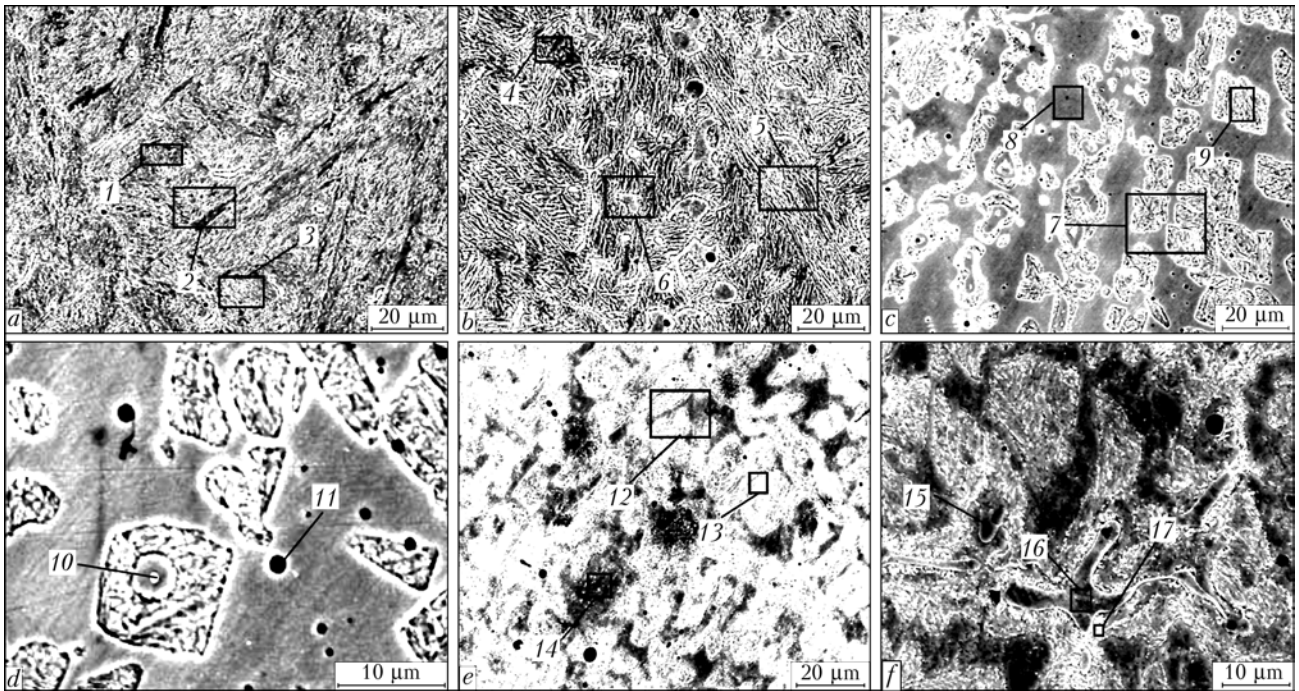


Figure 5. Microstructure of samples of deposited metal 30Kh2M2NSGF without phosphorus (a) and with 0.57 (b), 0.89 (c, d) and 1.42 wt.% P (e, f) (see Table 3)

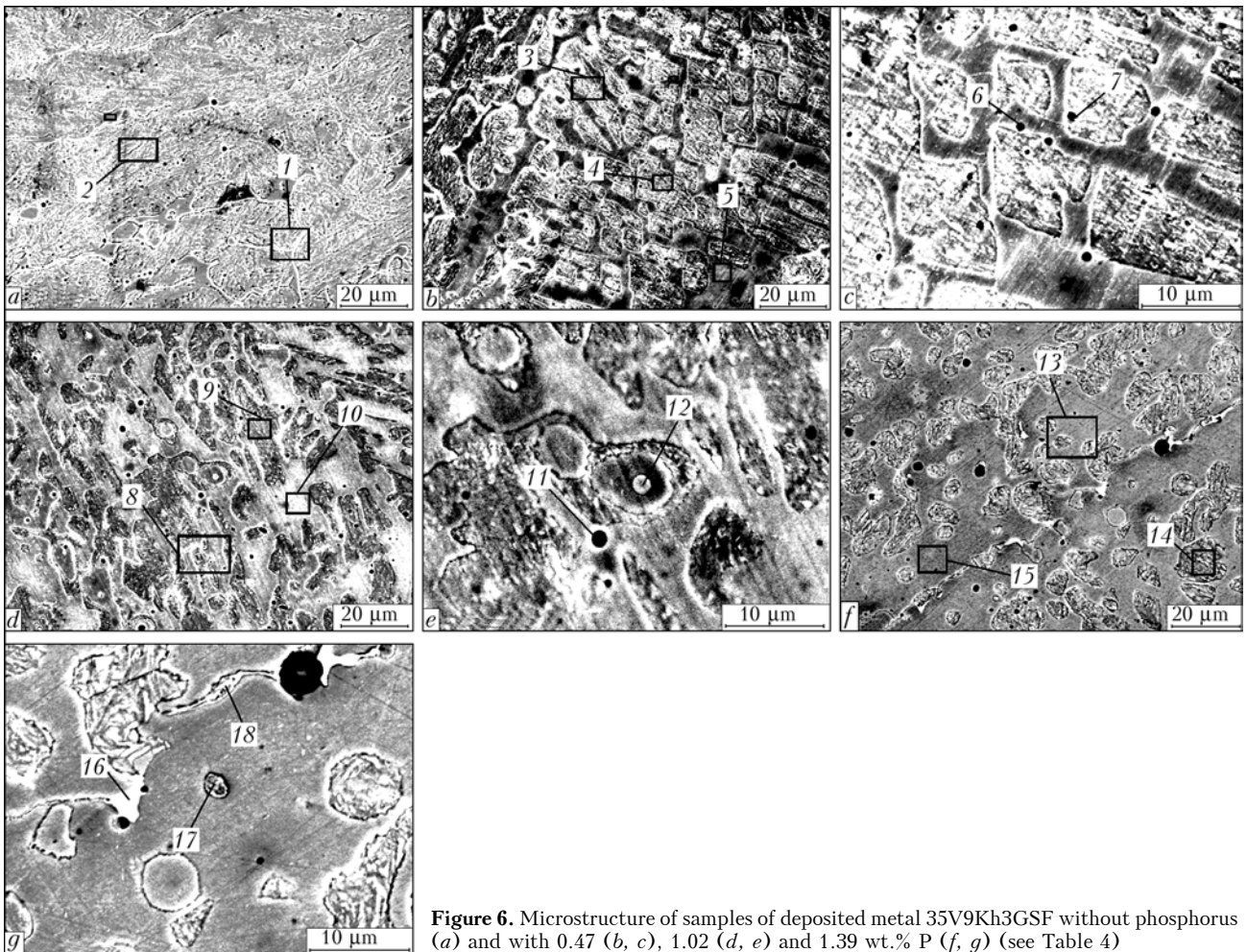


Figure 6. Microstructure of samples of deposited metal 35V9Kh3GSF without phosphorus (a) and with 0.47 (b, c), 1.02 (d, e) and 1.39 wt.% P (f, g) (see Table 4)



Table 2. Results of X-ray microanalysis of the metal deposited with flux-cored wire PP-Np-30Kh4V2M2FS

Phosphorus content, wt.%	Place of analysis	No. of investigated region according to Figure 4	Elements content, wt.%							
			Fe	Mn	Si	P	Cr	Mo	W	V
Without phosphorus	Matrix	1	90.38	1.33	1.23	0	4.31	1.33	0.68	0.23
	Same	2	89.74	1.28	0.70	0	3.37	1.77	2.41	0.37
	Inclusion	3	70.92	11.84	2.00	0.30	3.37	8.19	3.18	0.16
	Same	4	81.52	5.52	2.53	0.29	3.66	3.24	3.03	0.20
0.45	Matrix	5	87.83	1.95	0.50	0.42	3.49	2.51	2.92	0.37
	Same	6	88.27	1.58	0.81	0.66	3.86	2.24	1.71	0.31
	»	7	91.48	1.32	1.12	0	3.59	1.44	0.86	0.20
	Inclusion	8	60.41	18.54	4.43	0.47	3.37	9.10	3.01	0.63
	Same	9	79.52	7.20	4.55	0.37	3.46	2.06	2.55	0.31
0.93	Matrix	10	90.60	1.41	0.83	0.69	2.29	2.43	0.46	0.31
	Same	11	92.93	1.02	0.89	0.32	2.68	1.00	0	0.18
	»	12	88.20	1.26	0.39	1.31	2.16	3.73	0.80	0.72
	Inclusion	13	35.16	39.24	7.71	0.88	1.06	5.77	9.04	0.78
	Same	14	68.63	2.39	0.25	8.14	5.15	11.56	1.46	1.67
1.52	Matrix	15	85.53	1.13	0.01	1.64	3.71	2.51	4.87	0.34
	Same	16	89.06	1.14	0.79	0.81	4.37	1.47	1.69	0.68
	»	17	87.15	1.66	0.37	0.95	4.02	1.97	3.74	0.17
	Phosphide film	18	67.81	2.63	0.53	6.63	8.22	7.94	4.82	1.42

Table 3. Results of X-ray microanalysis of the metal deposited with flux-cored wire PP-Np-30Kh2M2NSGF

Phosphorus content, wt.%	Place of analysis	No. of investigated region according to Figure 5	Elements content, wt.%							
			Fe	Mn	Si	P	Cr	Mo	Ni	V
Without phosphorus	Matrix	1	91.95	1.25	0.66	0	2.21	2.43	1.21	0.29
	Same	2	90.64	1.27	0.13	0	2.28	2.80	1.33	0.47
	»	3	90.21	0.98	0.12	0.18	2.21	3.43	0.40	0.34
0.57	»	4	91.24	1.12	0.75	0.61	2.47	1.99	1.27	0.17
	»	5	91.68	1.36	0.45	0.12	1.84	2.32	1.18	0.17
	»	6	93.81	0.94	0.49	0.04	2.25	1.49	0.60	0.24
0.89	»	7	87.88	1.67	0.92	0.76	4.30	2.20	0	0.31
	»	8	86.87	1.99	1.18	0.87	3.65	1.32	0.30	0.27
	»	9	86.97	1.24	0.75	0.69	4.40	2.11	0.40	0.23
	Inclusion	10	83.82	1.62	1.44	2.57	5.22	3.10	0	0.76
	Same	11	69.14	11.43	6.57	0.94	3.82	4.27	0	0.36
1.42	Matrix	12	90.21	2.08	0.56	0.95	2.19	2.22	1.15	0
	Same	13	91.70	1.04	0.77	0.89	2.33	2.33	0.75	0.20
	»	14	88.77	1.54	0.39	1.24	1.82	2.41	1.50	0.35
	Inclusion	15	69.21	3.19	0.39	8.95	5.07	9.63	1.64	1.39
	Same	16	72.19	2.60	0.59	8.17	4.86	8.71	1.67	1.21
	»	17	71.29	2.76	0.60	8.72	4.69	9.42	1.13	1.23

**Table 4.** Results of X-ray microanalysis of the metal deposited with fluxed-cored wire PP-Np-35V9Kh3GSF

Phosphorus content, wt.%	Place of analysis	No. of investigated region according to Figure 6	Elements content, wt.%						
			Fe	Mn	Si	P	Cr	W	V
Without phosphorus	Matrix	1	88.87	1.38	0.30	0	2.45	6.20	0
	Same	2	90.84	1.25	0.18	0	1.74	5.39	0.60
0.47	»	3	88.44	1.35	0	0.23	1.72	7.38	0.38
	»	4	90.36	1.36	0	0	1.49	5.93	0.53
	»	5	88.16	1.75	0.33	0.45	2.09	5.71	0.37
	Inclusion	6	88.82	1.33	0.25	0.33	2.31	6.45	0.51
	Same	7	88.10	2.39	0.32	0.27	1.76	6.16	0.25
1.02	Matrix	8	89.51	1.63	1.22	0.70	1.96	3.67	0.45
	Same	9	87.84	1.82	0.54	0.80	2.11	5.37	0.46
	»	10	87.40	1.42	0.44	0.70	1.96	3.67	0.45
	Inclusion	11	72.53	11.22	3.09	0.73	1.31	7.35	1.50
	Same	12	79.23	3.22	0.13	6.07	4.72	5.49	0.75
1.39	Matrix	13	85.10	1.12	0	1.56	2.07	9.17	0.37
	Same	14	90.05	1.35	0.40	0.48	2.06	5.42	0.21
	»	15	87.78	0.64	0	0.89	2.04	8.26	0.36
	Inclusion	16	70.98	2.39	0	7.59	5.86	11.53	1.41
	Same	17	73.75	4.52	0.23	9.73	6.28	3.63	1.57
	Phosphide film	18	72.28	3.68	0.61	12.24	7.70	2.06	1.34

components of all the three types of the deposited metal, and no free phosphides were fixed.

At the same time, a significant heterogeneity was fixed for phosphorus: in deposited metal 30Kh4V2M2FS the phosphorus content varied in a range of 0.37–0.66 wt.%; in 30Kh2M2NSGF it is 0.12–0.61 wt.%; in 35V9Kh3GSF — 0.23–0.45 wt.%. Apparently, this can be explained by a different level of dissolution of phosphorus in α - and γ -iron [10].

With increase in the content of phosphorus to 1 wt.%, heterogeneity for tungsten and molybdenum was fixed in deposited metal 30Kh4V2M2FS (Figure 4 *e, f*; Nos. 10–14, Table 2); for nickel in 30Kh2M2NSGF (Figure 5, *c, d*; Nos. 7–11, Table 3); and for silicon and tungsten in 35V9Kh3GSF (Figure 6, *d, e*; Nos. 8–12, Table 4). Formation of globular phosphide inclusions takes place in deposited metal 30Kh4V2M2FS with 8.14 wt.% P (see Figure 4, *f*; No. 14, Table 2) and in 35V9Kh3GSF with 6.07 wt.% P (Figure 6, *e*; No. 12, Table 4). Phosphides contain an increased weight fraction of manganese, chromium, molybdenum and tungsten. Free phosphides were not detected in deposited metal 30Kh2M2NSGF with a weight fraction of phosphorus equal to about 1%. In deposited metal 30Kh4V2M2FS the phosphorus content in different structural components of the matrix varies in a range of 0.32–1.31 wt.%, in 30Kh2M2NSGF — in a range of 0.69–0.88 wt.% P, and in 35V9Kh3GSF it makes up 0.70–0.80 wt.%.

Heterogeneity for silicon and tungsten was detected in deposited metal 30Kh4V2M2FS with a phosphorus content of about 1.5 wt.% (Figure 4, *g*; Nos. 15–18, Table 2), for vanadium in 30Kh2M2NSGF (Figure 5, *e*; Nos. 12–14, Table 3), and for silicon, manganese and tungsten — in 35V9Kh3GSF (Figure 6, *f*; Nos. 13–15, Table 4). In the deposited metal of all the three types the occurrence of isolated phosphide inclusions of a compact shape, as well as of phosphide films, was fixed (Figure 4, *g*; No. 18, Table 2; Figure 5, *f*; Nos. 15–17, Table 3; Figure 6, *g*; Nos. 16–18, Table 4). The content of phosphorus in them varies from 5.93 (30Kh4V2M2FS) to 12.24 wt.% (35V9Kh3GSF). Phosphides and phosphide films contain an increased weight fraction of manganese, chromium, molybdenum and vanadium. Phosphorus in different structural components of the matrix is distributed in the following way: in deposited metal 30Kh4V2M2FS — 0.81–1.64 wt.%, in 30Kh2M2NSGF — 0.95–1.64 wt.%, and in 35V9Kh3GSF — 0.48–1.57 wt.%.

The X-ray microanalysis confirmed the earlier thermodynamic calculations of equilibrium of chemical reactions of formation of phosphides for the main alloying elements [11]. The calculations showed that first of all the formation of phosphides of vanadium, molybdenum, chromium, manganese and tungsten (in a decreasing order), i.e. the elements the increased content of which were detected in phosphides of the



investigated types of deposited metal, might be expected.

Thus, the X-ray microanalysis showed that increase in the phosphorus content of up to 1.5 wt.% causes an increase in the weight fraction of dissolved phosphorus in the matrix of the deposited metal of the investigated alloying systems. Inclusions of globular phosphides are formed in the deposited metal of the investigated types at a phosphorus content of about 1 wt.%. At a phosphorus content of about 1.5 wt.% a significant increase of compact phosphide inclusions, as well as of phosphide films, takes place, this leading to cracking of the deposited metal.

The investigations determined that a high-alloy deposited metal is characterized by formation of complex phosphides, which contain, depending on the alloying system, vanadium, molybdenum, chromium, manganese and tungsten, i.e. the metals the phosphides of which exhibit the highest thermodynamic stability and have a rather high melting temperature. The presence of such globular phosphides does not cause deterioration of crack resistance of the investigated types of the deposited metal.

1. Ryabtsev, I.I., Kuskov, Yu.M. (2003) Prospects for applying phosphorus in iron-base surfacing consumables (Review). *The Paton Welding J.*, **1**, 12–16.
2. Ryabtsev, I.I., Kuskov, Yu.M., Grabin, V.F. et al. (2003) Tribological properties of the Fe–Cr–Si–Mn–P system deposited metal. *Ibid.*, **6**, 16–20.
3. Alekseev, A.A., Yaydoshchin, I.R., Vojtkevich, V.G. et al. (1989) Influence of phosphorus on structure and properties of weld metal in welding of low-alloy steels. *Avtomatich. Svarka*, **4**, 7–10.
4. Pokhodnya, I.K., Vojtkevich, V.G., Alekseev, A.A. et al. (1992) Influence of phosphorus on impact toughness and chemical microheterogeneity of weld metal. *Ibid.*, **2**, 3–7.
5. Ryabtsev, I.I., Kuskov, Yu.M., Novikova, D.P. (2006) Effect of phosphorus on crack resistance of low-carbon deposited metal of alloying system Fe–Mn–Si–Cr. *The Paton Welding J.*, **5**, 12–15.
6. Ryabtsev, I.A., Kondratiev, I.A. (1999) *Mechanized electric arc surfacing of metallurgical equipment parts*. Kiev: Ekotekhnologiya.
7. Kondratiev, I.A., Vasiliev, V.G., Dovzhenko, V.A. (1990) Structure and properties of metal deposited by flux-cored wires of PP-Np-25Kh5FMS and PP-Np-30Kh4V2M2FS grades. In: *Equipment and materials for surfacing*. Kiev: PWI.
8. Kondratiev, I.A., Gladky, P.V. (1996) Flux-cored wire PP-Np-30Kh2M2NF for surfacing of hot rolling cylinders. In: *Means of development of machine-building complex of Magnitogorsk Metallurgical Works*. Magnitogorsk: Mars.
9. Frumin, I.I. (1961) *Automatic electric arc surfacing*. Kharkov: Metallurgizdat.
10. Lunev, V.V., Averin, V.V. (1988) *Sulphur and phosphorus in steel*. Moscow: Metallurgiya.
11. Ryabtsev, I.I. (2008) Calculation-experimental evaluation of the efficiency of alloying the high-alloy deposited metal with phosphorus. *The Paton Welding J.*, **5**, 13–17.

FLUX-CORED WIRE AND TECHNOLOGY FOR ARC SURFACING OF RAILROAD FROGS OF HADFIELD STEEL 110G13L

Technology of semiautomatic arc surfacing and self-shielding flux-cored wire PP-AN105 were developed for reconditioning of parts from Hadfield steel 110G13L (railroad frogs, components of crushing-milling equipment) and repair of casting defects. Metal deposited with this wire is characterised by high ductility and toughness. Its hardness after deposition amounts to *HB* 180–200, and after cold working – to *HB* 350–400. In the cold worked state, the deposited metal has very high wear resistance under conditions where wear is accompanied by heavy impacts or high contact pressure.

Semiautomatic devices PSh-107, PDO-517, etc., providing feed of flux-cored wire with a diameter of up to 3 mm and equipped with power supply VDU-506 or other type having similar characteristics, are used for surfacing railroad frogs. The frogs are prepared for surfacing by removing films, metal rolls and upper layer with microcracks from wing rails and cores using abrasive wheels. The layer deposited in one pass is 4–5 mm thick. In multilayer surfacing, it is necessary to apply forging for each deposited layer. Treated frogs are subjected to grinding using a suspended rail grinding machine tool.

The developed technology provides high-quality deposited layers in repair of frogs with a vertical wear of wing rails and cores down to 25 mm (allowing for removal of cracks, spallings and other defects). The experience shows that it is possible to successfully deposit frogs with individual defects removed to a depth of down to 40 mm. Depending upon the depth of wear, the frogs repaired by surfacing can be used in main, approach and other tracks.

Other parts of Hadfield steel can be repaired by the similar technology.

Application. Surfacing of railroad frogs, components of crushing-milling equipment, recovery of sizes and repair of casting defects.

Proposals for co-operation. Supply of flux-cored wire on a contract base, application of the surfacing technology.

Contacts: Ryabtsev I.A.
E-mail: ryabtsev@paton.kiev.ua



EFFECTIVENESS OF APPLICATION OF COMBINED MAGNETIC FIELDS IN SUBMERGED-ARC WELDING

D.G. NOSOV¹ and A.D. RAZMYSHLYAEV²

¹Dneprodzerzhinsk State University, Dneprodzerzhinsk, Ukraine

²Priazovsky State Technical University, Mariupol, Ukraine

It is suggested that a combination of three magnetic fields be applied to widen the possibilities of controlling the shape and size of the penetration zone in submerged-arc wire hardfacing. Mathematical models establishing a relationship between induction of components of a combined magnetic field (CMF) and cross-section size of the deposited beads were developed by employing the experimental design and regression analysis methods. Software with a friendly interface was developed for computation and optimization of technological modes of arc hardfacing in CMF, and the extent of impact of the induction of components, as well as a combination of these components of magnetic fields on cross-section sizes of the deposited beads is shown.

Keywords: arc hardfacing, deposited bead, bead size, controlling magnetic fields, asymmetry, mathematical models, dispersion analysis

Under the conditions of saving the energy resources, deficit and expensive materials, of greatest interest is development of such a hardfacing process, which would permit addressing the following technological problems: reduce the fraction of base metal in the deposited metal; improve hardfacing efficiency; reduce machining costs and improve product performance.

The posed task can be solved by controlling the configuration and geometrical dimensions of the deposited bead cross-section. Realization of the process of bead deposition with its controllable configuration is possible with simultaneous action of several magnetic, i.e. combined magnetic fields (CMF), in arc hardfacing.

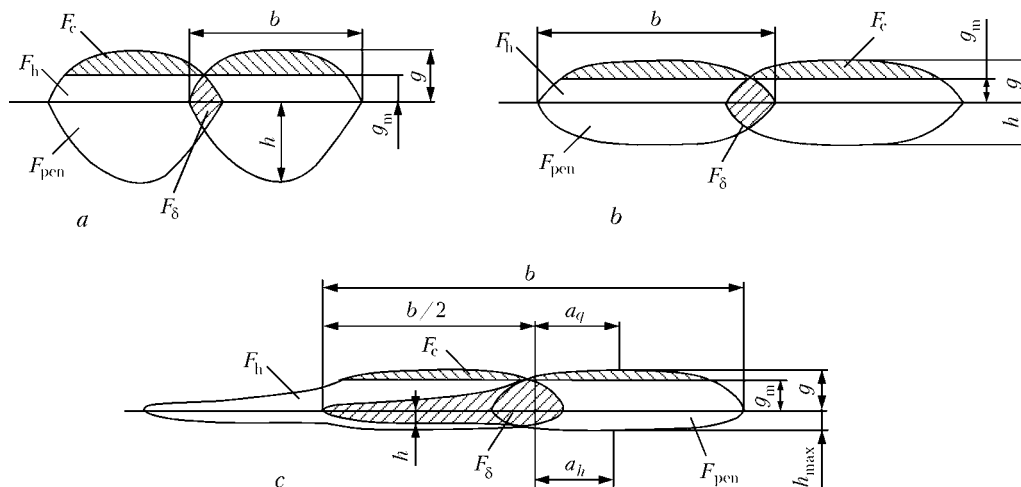
Figure 1 schematically presents transverse sections of beads deposited by the classical technology without using magnetic fields (MF) (Figure 1, a), using just

the longitudinal MF (Figure 1, b) and with CMF system proposed in this work (Figure 1, c).

Hardfacing requires the bead in the transverse section to have minimum values F_{pen} , F_c , h at maximum values of F_h , F_δ , g , b (Figure 1, a). In addition, difference $(g - g_m)$ showing the allowance for machining of the hardfaced surface should be the smallest. This is partially achieved at hardfacing using just one longitudinal MF (Figure 1, b), but the bead section shape given in Figure 1, c meets these conditions in the most complete fashion.

It was assumed that the above bead shape can be achieved using in hardfacing a combination of three MF acting simultaneously on the welding arc and weld pool liquid metal: axial constant, transverse pulsed unipolar and axial variable of a set frequency.

Irreversible displacements of the melt pool are achieved under the impact of a constant axial MF coaxial with the electrode. The arc revolves about its axis and acquires a conical bell shape [1–3]. Dimensions of the arc active spot on the product become greater. The bead width also increases as a result of





«eroding» of the pool side surfaces by hot flows of the melt, which is a positive factor at hardfacing.

The impact of a transverse pulsed unipolar MF on the arc generates an electromagnetic force, which deflects the arc normal to the deposition rate vector. This allows, as shown in [4], ensuring a transverse deflection of the arc active spot on the product up to 10–12 mm. Transverse deflections of the arc will allow changing the bead section shape, influencing the melt flow rate, guiding it along the fusion line, and in view of their unipolarity they will lead to an asymmetry of the penetration zone, required for deposition of adjacent beads and of the bead reinforcement shape, as shown in Figure 1, c.

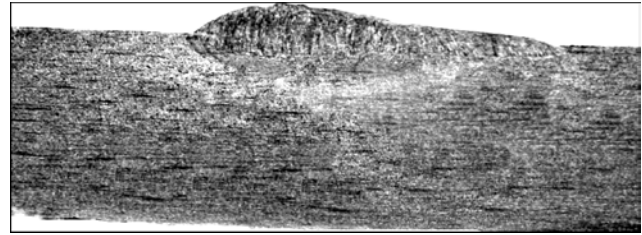
By applying axial alternating MF to the pool tail part, it is possible to prevent the undesirable increase of the penetration depth in the asymmetry zone. The action of this field results in formation of eddy flows of the melt, forming the effect of a «stable wave», increasing the thickness of the liquid interlayer under the arc, as the massive wave has a considerable inertia, and at a fast variation of MF polarity the pool does not develop any reversible melt motions.

A series of experimental beads were deposited to confirm the above assumptions and develop a mathematical model, which allows establishing induction parameters of each field in the above combination of three MF, providing the required bead section shape. In order to reduce the number of the beads, a central composite rotatable five-level full-factor experimental plan consisting of 20 series was used. Experiments were conducted in random fashion to avoid appearance of a systematic error in the procedure.

Beads were deposited on sheets of St3sp (killed) steel (GOST 380–90) 50 mm thick by ADS-1004 welding tractor powered from VDU-1001 arc power source with Sv-08A wire of 3, 4 and 5 mm diameter using AN-348A flux. MF was generated by a special device, consisting of three independent electric magnets. The following parameters of hardfacing mode in CMF were used: deposition current of 450–750 A, arc voltage of 26–34 V, electrode extension of 25–30 mm, and deposition rate of 0.8–1.6 cm/s. The distance from the electric magnet edges to the product was equal to 10–15 mm. Inductance of axial constant MF, symmetrical relative to the electrode axis, $B_z = 30$ –60 mT; inductance of the transverse pulsed unipolar MF B_y was 50–100 mT. An axial alternating MF of set frequency with inductance B_x of 40–80 mT acts in the pool tail part. The above range of CMF inductions with the optimized hardfacing modes provides a satisfactory quality of the deposited bead.

Bead parameters (width b , height g , maximum penetration depth h_{max} , penetration depth of even section h , deviation of bead height a_g and penetration depth a_h) were determined from deposit macrosections. As an example, Figure 2 gives the macrosection of the bead produced at hardfacing using CMF.

A regression method was used to forecast the bead geometrical dimensions. The function of the response



surface, representing any dimension in the bead section, can be expressed as $y = f(B_z, B_y, B_x)$, and the selected dependence, which is the response surface of the second order, can be given by [5]

$$y = b_0 + b_1B_z + b_2B_y + b_3B_x + b_{11}B_z^2 + b_{22}B_y^2 + b_{33}B_x^2 + b_{12}B_zB_y + b_{13}B_zB_x + b_{23}B_yB_x, \quad (1)$$

where b_0, b_1, b_2, b_3 are the constant term and the coefficients of linear terms, respectively; b_{11}, b_{22}, b_{33} are the coefficients of square terms of the second order; b_{12}, b_{13}, b_{23} are the coefficients of the interacting terms of the second order.

The coefficients of the above polynomial equation were determined using Nonlinear Models STATISTICA 6.0 software package.

The coefficient value was checked using t -test, as well as a method of reverse exclusion. The adequacy of the developed model was verified by regression analysis.

The following equations were obtained for the bead geometrical parameters:

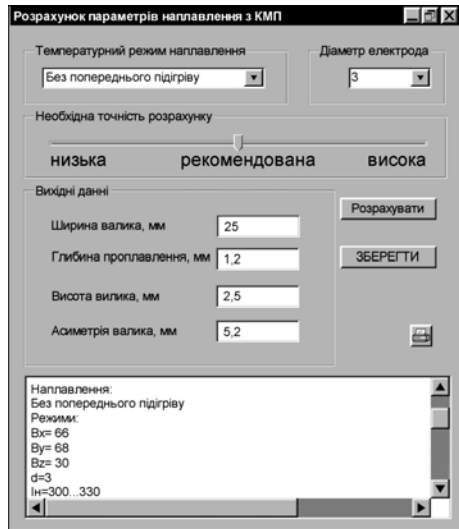
$$b = 24.12614 - 0.27163B_z - 0.03248B_y - 0.21372B_x + 0.00474B_z^2 + 0.00115B_y^2 + 0.00204B_x^2 + 0.00083B_zB_y + 0.00113B_zB_x + 0.00053B_yB_x;$$

$$a_g = -0.211365 - 0.031212B_z + 0.086273B_y - 0.022159B_x + 0.00052B_z^2 - 0.000433B_y^2 + 0.000105B_x^2 + 0.000533B_zB_y - 0.000417B_zB_x + 0.0008B_yB_x;$$

$$a_h = 0.03066 - 0.051477B_z + 0.076114B_y - 0.002983B_x + 0.000545B_z^2 - 0.000484B_y^2 - 0.000162B_x^2 + 0.000767B_zB_y - 0.000208B_zB_x + 0.000675B_yB_x;$$

$$h_{max} = 2.813634 - 0.017145B_z + 0.007273B_y - 0.027784B_x - 0.000369B_z^2 + 0.000187B_y^2 + 0.000199B_x^2 - 0.000333B_zB_y + 0.00075B_zB_x - 0.0002B_yB_x;$$

$$h = 0.64659 - 0.010114B_z + 0.023432B_y + 0.007415B_x + 0.000328B_z^2 + 0.000118B_y^2 + 0.000247B_x^2 - 0.0005B_zB_y - 0.000208B_zB_x - 0.000375B_yB_x;$$



$$g = 0.82159 + 0.039053B_z + 0.013432B_y + 0.013665B_x - 0.000727B_z^2 + 0.000198B_y^2 - 0.000097B_x^2 - 0.000033B_zB_y + 0.000125B_zB_x - 0.000275B_yB_x.$$

Model accuracy was subjected to evaluation by making deposits in the same experimental equipment. It is established that the geometrical dimensions of the beads made experimentally correspond to the dimensions obtained by the above equations with sufficient accuracy.

Geometrical parameters of the bead deposited in CMF depend on electrode wire diameter, d_{el} . Therefore, mode correction was performed in blocks for electrodes of 3, 4 and 5 mm diameter. Correction coefficients allowing for the change of deposited bead shape at the change of the main parameters of the hardfacing mode, were determined experimentally.

Base metal share γ was taken to be the optimization parameter, alongside the deposited bead dimensions. The authors proposed a formula for determination of

bead configuration, allowing for its variation under the CMF impact:

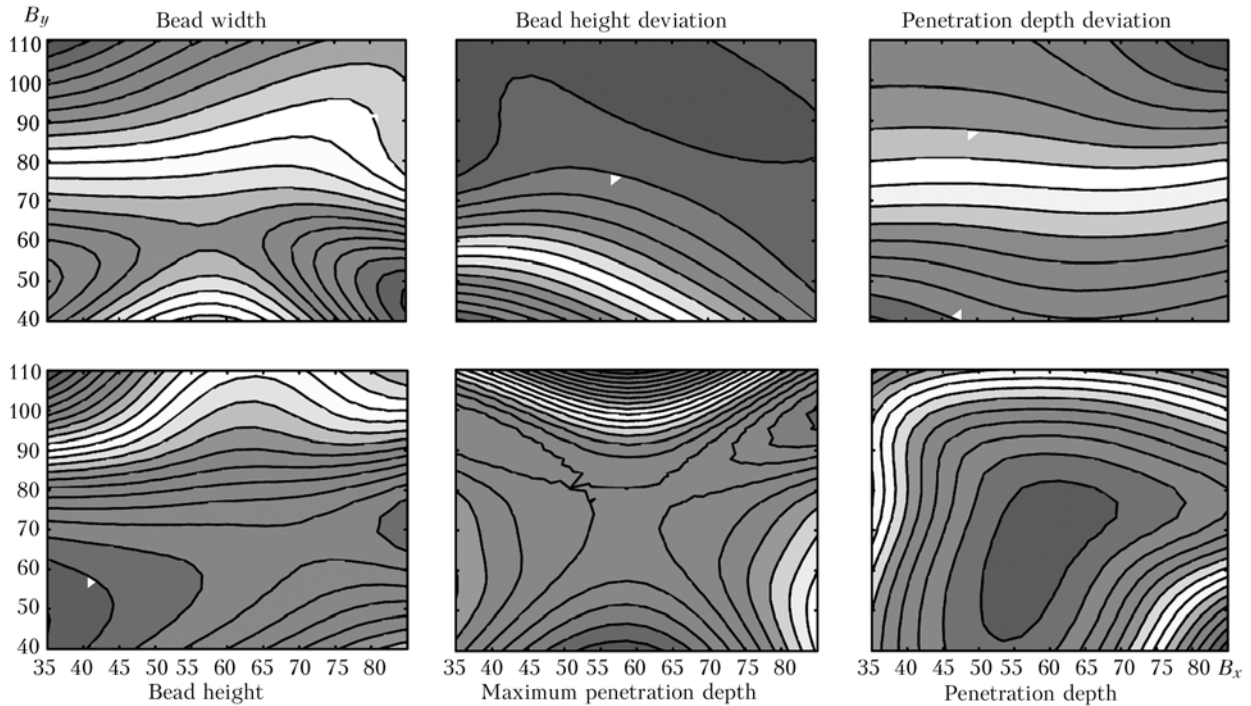
$$\gamma = \frac{F_{i\delta}}{F_i + F_{i\delta}} = \frac{\frac{\pi}{4} h_{\max} (b - 2a_h) + 2a_h h}{\frac{\pi}{4} (g_{\max}(b - 2a_g) + h_{\max}(b - 2a_h)) + \frac{2}{3} a_g g + 2a_h h}. \quad (2)$$

Data processing by formula (2) showed that in bead deposition with CMF the share of base metal in the deposited metal decreases 1.6 to 1.8 times.

A program in Delphi language version 7.0 was written for calculation of optimum values of induction of each of the three CMF components, at which the specified dimensions of bead section can be produced. Calculation program interface is given in Figure 3. Examples of protocols generated using this program, are given in the Table. The following parameters were assigned: bead width $b = 25$ mm; penetration depth $h = 1.2$ mm; bead height $g = 2.5$ mm; bead asymmetry $a_h = 5.2$ mm. Correspondence matching showed that CMF parameters, calculated using the program, ensure coincidence of calculated dimensions of bead section with experimental values with a sufficient degree of accuracy.

The above equations correlating the induction of CMF, applied at electric arc hardfacing, with geometrical dimensions of bead section, were used to plot the graphs of the response surface given in Figures 4–6. These data allow analyzing the influence of induction values of MF, included into the CMF composition, on bead section dimensions.

The data showed that at the minimum value of induction B_y bead width increases only slightly in the range of induction values B_x from 40 to 57 mT. Such a tendency can be due to the positive influence of the axial MF on hydrodynamics of the surface layer of



the pool liquid metal. Maximum increase of bead width is observed at induction B_y starting from 90 mT, if B_x values are equal to 35–70 mT. This is attributed to a significant deviation of the arc to one of the sides normal to the deposition vector and its reciprocal motion under the impact of induction B_x .

At simultaneous increase of inductions B_y and B_x a stable increase of bead asymmetry along its height is observed, whereas induction value B_y is the main factor affecting bead asymmetry along its depth. Induction value B_y in the range from 80 to 110 mT can be taken as the optimum one.

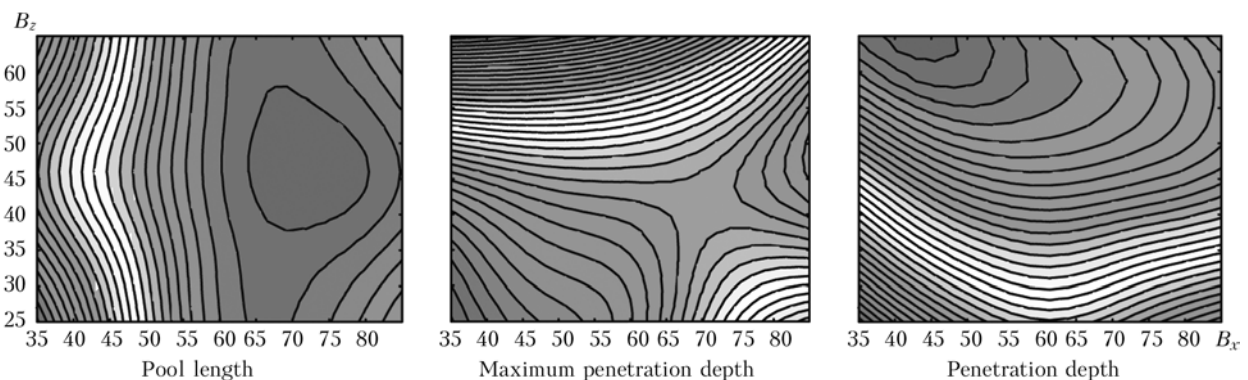
Characteristic variations of bead height and maximum penetration depth under the impact of B_y and B_x are shown in Figure 4. Bead height becomes smaller, and penetration depth in its shifted part increases at simultaneous impact of transverse pulsed unipolar MF in the range from 92 to 110 mT and axial variable MF in the range from 35 to 62 mT.

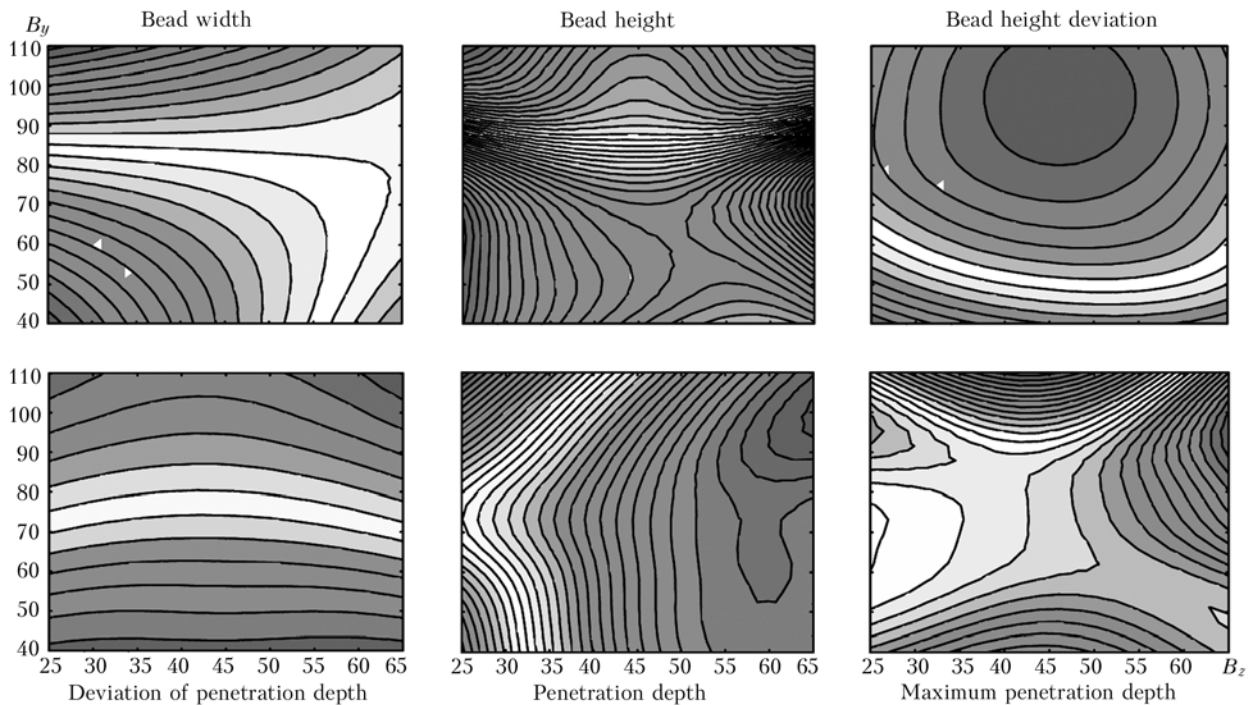
A minimum value of penetration depth can be achieved in a rather broad range of B_y – B_x parameters.

B_x range of 45 to 76 mT at induction $B_y = 66$ –88 mT can be taken as the optimum one.

Group of inductions B_y – B_x strongly influences the base metal penetration depth, and, therefore, also the share of base metal in the deposited metal. Range of inductions B_z from 55 to 65 mT at induction B_x in the range from 35 to 70 mT is the optimum one. Influence of this induction group on other dimensions of bead section is negligible.

Group of inductions B_y – B_z has an essential influence on bead width and leads to an increase of this parameter in the entire induction range (Figure 6). Maximum value of bead width is observed at change of induction B_y in the range from 94 to 110 mT, if induction B_z is in the range of 25–55 mT. It should be noted that in this range of inductions B_y , increase of induction B_z leads to a small narrowing of the bead. The latter is, obviously, related to the stabilizing impact of the axial constant MF (with induction B_z) on the arc.





Bead height increases at the impact of a transverse MF of induction 86–110 mT on the pool. Now, the influence of a constant axial component of CMF of induction B_z on this parameter is negligible. However, in the induction range $B_z = 42\text{--}47$ mT a tendency to reduction of bead height by 8–10 % is observed at a considerable increase of bead asymmetry a_g . It is established that the maximum influence on bead asymmetry both by height and by depth is made by a pulsed unipolar transverse MF B_y . Moreover, at induction B_y of the order of 100–110 mT an increase of base metal penetration depth by 30–35 % is observed (Figures 4 and 6). MF component B_z at the value of its induction of 40 mT and higher allows compensating the increase of penetration depth by bead section undesirable at hardfacing.

Thus, MF combination proposed in this work at optimum induction parameters of each of the components of these fields, established by design-experimental methods, allows a significant widening of the possibilities of controlling the shape and dimensions of base metal penetration zone in arc hardfacing, and reducing the share of base metal in the deposited metal.

CONCLUSIONS

1. MF combination proposed in the work allows a more efficient control of the geometrical dimensions of the deposited bead section that when one longitudinal MF is used.
2. The proposed procedure and equations for calculation of bead section dimensions at hardfacing with CMF impact, depending on induction of the components of this combined MF, provide a good combination of the calculated and experimental data.
3. At optimum CMF parameters it is possible to 1.6–1.8 times reduce the share of the base metal in the deposited metal, which may be the basis for development of new resources-saving hardfacing technologies.

1. Chernysh, V.P., Kuznetsov, V.D., Briksman, A.N. et al. (1983) *Welding with electromagnetic stirring*. Kiev: Tekhnika.
2. Budnik, N.M., Kulagin, A.P. (1979) Shape of arc between carbon electrodes in longitudinal magnetic field. *Avtomatich. Svarka*, **3**, 59–60.
3. Brizhev, V.A., Boldyrev, A.M. (1982) About effect of longitudinal magnetic field on straight polarity welding arc. *Ibid.*, **1**, 15–19.
4. Razmyshlyayev, A.D. (2000) *Magnetic control of weld formation in arc welding*. Mariupol: PGU.
5. Novik, F.S., Arsov, Ya.B. (1980) *Optimization of metal technology processes by planning experiment methods*. Moscow: Mashinostroenie; Sofia: Tekhnika.



MICROSTRUCTURE AND HARDNESS OF Al-Cu ALLOY (A2218) WELDED JOINTS PRODUCED BY GTAW

R. ALAPATI and D.K. DWIVEDI

Indian Institute of Technology, Roorkee, India

This paper describes the microstructure, phase analysis and microhardness of Al-Cu (A2218) alloy welded joints produced by pulse gas tungsten arc welding process in as welded and heat-treated condition. Welded joints were produced by two combinations of pulse parameters. Decrease in hardness was observed with postweld heat treatment of welded joints. Higher pulse frequency of 100 Hz showed finer grain structure of weld metal as compared with that at low pulse frequency 50 Hz. Heat treatment led to significant reduction in fraction of second phase constituents in HAZ and weld metal, and spheroidization of the eutectic silicon took place.

Keywords: aluminium 2218 alloy, pulse TIG welding, pulse frequency, microstructure, microhardness, postweld heat treatment (T6), HAZ softening

The heat treatable Al-Cu alloys are widely used in aircraft and automobile parts. Therefore, Al-Cu alloys are frequently fabricated by welding processes like gas metal arc welding or gas tungsten arc welding (GTAW) processes. Wider solidification temperature range and precipitation hardening tendency associated with these alloys make them sensitive to welding thermal cycle which is experienced by the base metal during welding [1, 2]. It is not uncommon to encounter the problems of cracking tendency and softening of HAZ of Al-Cu alloy joints [1, 3].

Recently some of the studies [3-10] on cracking tendency of Al-Cu alloy welded joint have been reported. Rao et al. [4, 5] reported that the use of different grain refinement techniques led to enhance the performance of Al-Cu welded joints and to reduce the cracking tendency. Haung and Kou [6, 7] observed that the liquation cracking is influenced by copper content and there is an optimum level of copper to avoid specific type of cracking. Gupta et al. [8] found that the cracking in Al-Cu alloys (A2219) occurs due to the lack of back filling liquid for healing the cracks.

Since, the microstructure of Al-Cu welded joints affects both types of problems (cracking and softening of HAZ). Therefore, better understanding on metallographic aspects of weld metal, HAZ and base metal of Al-Cu welded joint would assist the aluminium welding industry to produce sound welded joints. In view of above, the present investigation was carried out to study the effect of pulse GTAW parameters and postweld heat treatment (PWHT) on metallographic aspects and hardness of coarse grained cast Al-Cu alloys (which are more prone to cracking) welded by GTAW process.

Experimental procedure. *Materials.* In present investigation, Al-Cu alloy, namely A2218 was selected from 2xxx series. The alloy was prepared by sand mould casting in the form of plates (100 × 50 × 7 mm) from master alloys of Al-10 % Mg, Al-

30 % Ni, Al-50 % Cu, and Al-50 % Si and pure Al (99.99 %). Nominal composition of the Al-Cu alloy 2218 was as follows, wt. %: 4.0 Cu; 1.5 Mg; 2.0 Ni; 92.5 Al (no Si). A-405 (Al-5 % Si) filler was used as filler material for welding both Al-Cu alloys as Al-Si alloy filler reduces the cracking tendency of the Al-Cu alloys.

Welding. Butt joint welding of Al-Cu alloy was performed with an arc travel speed of 60 mm/min at base current 125 A, peak current 282 A, pulse frequency 100 (specimen 1) and 50 (specimen 2) Hz, duty cycle 30 (specimen 1) and 35 (specimen 2) %. Welding was carried out on CEBORA 360 semi-automatic machine. A BUG-O system for moving the torch at constant speed was used during welding. Following parameters were kept maintained during the welding with 2 % thoriated tungsten electrode: $d_{el} = 3.0$ mm; $U_a = 18$ V; $l_a = 2.5$ mm; shielding gas --- argon.

Estimation of energy input E was done for bead-on-plate welding of Al-Zn-Mg alloy welds using following equation [9]: E (J/mm) = U_a (V) · I_{mean} (A) / v_w (mm/s), where $I_{mean} = ((I_b T_b) + (I_p T_p)) / (T_b + T_p)$.

PWHT of welded joints was carried out to study the effect of mode T6 on their hardness and microstructure. Heat treatment consisted of solutionizing of welded joints at 510 °C for 4 h, followed by water quenching at room temperature and artificial aging at 175 °C for 6 h.

Metallographic study. Specimens were cut from the welded joint, the transverse cross section of which was polished using standard metallographic procedure. Then polished specimens were etched with Keller's reagent before microscopic examination. Micrographs of different regions like weld bead, fusion line, HAZ and base metal were taken using Leitz MM-6 microscope at different magnifications. Phase analysis was carried out using ImageJ software.

Hardness testing. Vickers microhardness was measured on one side of the welded joint from weld center to base metal at an interval of 1 mm distance with a load of 100 g using Leitz microhardness tester. Hardness was measured in both as welded condition and heat-treated condition.

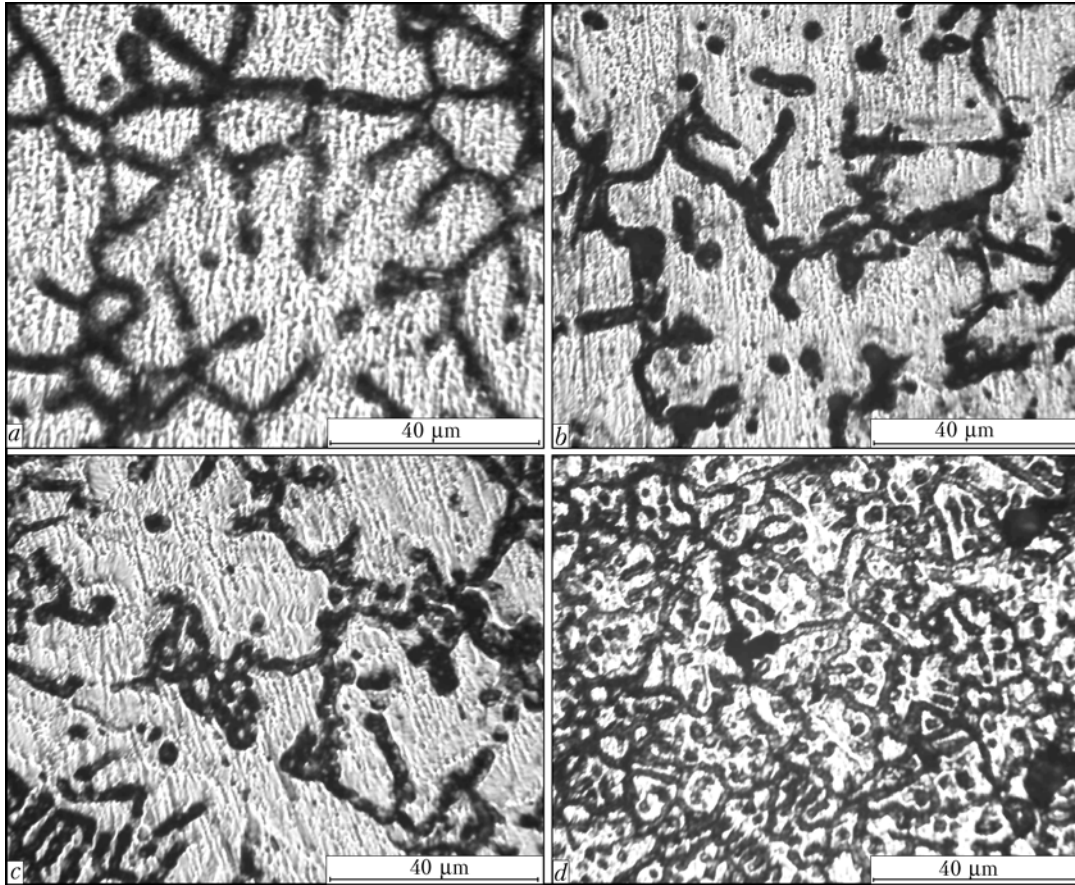


Figure 1. Microstructure of base metal (a), HAZ (b), fusion boundary (c) and weld metal (d)

Results and discussion. The microstructures of different zones of welded joints are shown in Figure 1, *a-d*. It can be observed that there is significant variation in microstructure from base metal to weld metal. Micrographs exhibited reduction in fraction of low melting phases along the grain boundary in HAZ as compared with that of base metal. This decrease in the fraction of second phase along the grain boundary can be attributed to the dissolution of second phase particles under the effect of welding thermal cycle

Table 1. Microstructural details of 2218 alloy in as welded and heat-treated condition

Specimen number	f_{pulse} , Hz (duty cycle, %)	Average α -Al grain size, μm	α -Al fraction area, %	Average eutectic grain size, μm	Eutectic fraction area, %
1	100 (35)	28.5	42.1	32.0	47.9
	100 (35)	23.64	68.2	8.9	30.6
2	50 (30)	24.82	35.5	42.4	59.3
	50 (30)	14.1	46.8	16.4	56.9
3	100 (30)	51.36	47.7	28.48	55.3
	100 (30)	19.9	51.2	17.9	48.6
4	50 (35)	50.11	57.3	20.3	36.2
	50 (35)	12.65	16.3	51.5	73.7

Notes. Data for specimens of weld 1, 2 and HAZ metal 3, 4 in as welded conditions are given in numerator, and in heat-treated conditions — in denominator.

experienced by the metal near the fusion boundary in the HAZ. The grain structure at weld center was found finer than that near the fusion boundary. This is primarily due to changing solidification conditions (constitutional supercooling) from weld fusion boundary to weld center. High G/R ratio (where G is the actual temperature gradient, and R is the growth rate) at weld fusion boundary results in coarse columnar structure compared to that at the weld center [2, 10]. Intergranular cracks are also visible in weld metal. These cracks are formed largely due to shrinkage stress experienced by the solidifying low melting phases along the grain boundary because grain boundary area is generally prone to localization of the residual shrinkage stresses. Further, the lack of amount of low melting point phases in large quantity, especially near the terminal stage of solidification, can be another important reason for intergranular cracks in weld metal which prevents the healing of incipient cracks by back filling of molten metal [11].

The light etched area in these micrographs was identified as aluminum solid solution (α -Al), and EDAX analysis (Figure 2, *a*) of the same showed that it contains primarily aluminium and other elements in very small quantity. The EDAX analysis of second phase at grain boundary showed that it is rich of alloy elements. Low melting phase along the grain boundary contains, %: 14.32 Cu, 8.26 O₂, 1.57 Mg, 12.66 Ni and balance aluminium (Figure 2, *b*).

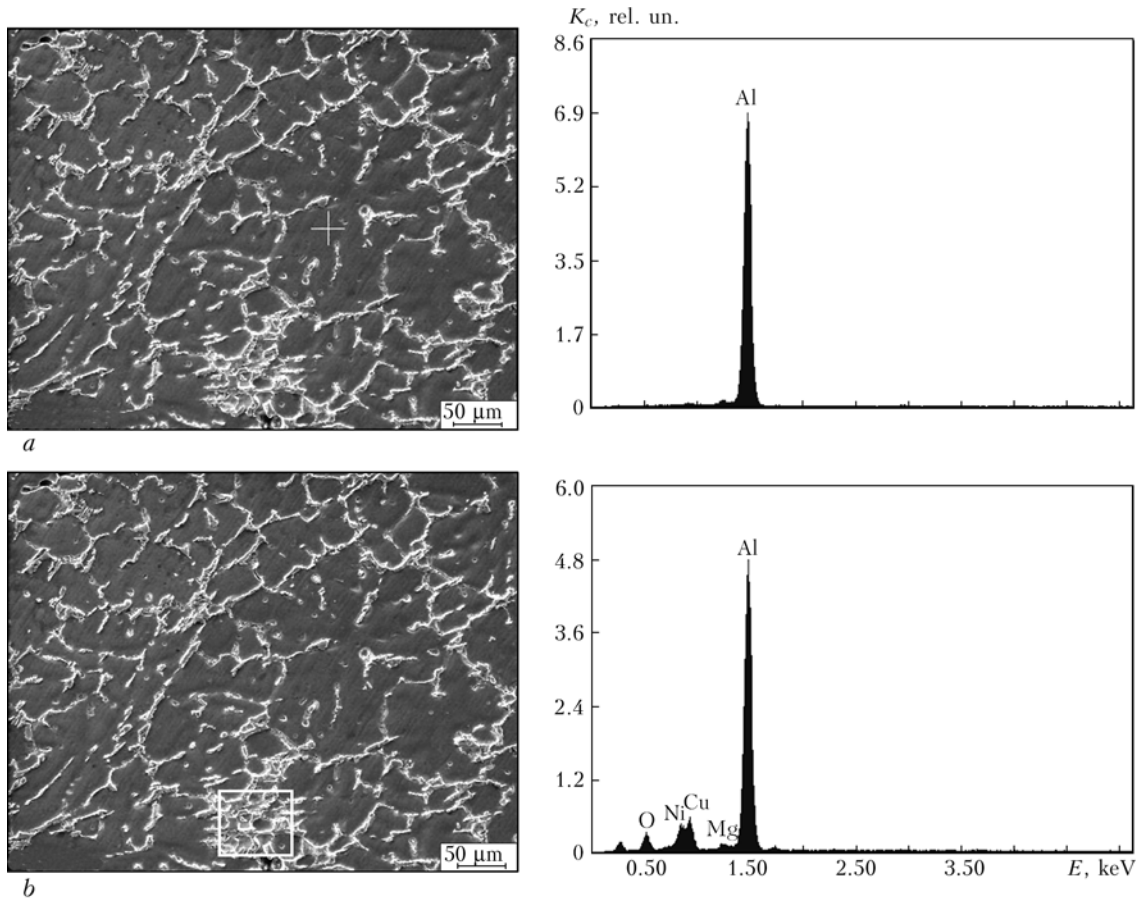


Figure 2. Microstructure and results of EDAX analysis of base metal zone: aluminium solid solution (a) and low melting phases at the grain boundary (b)

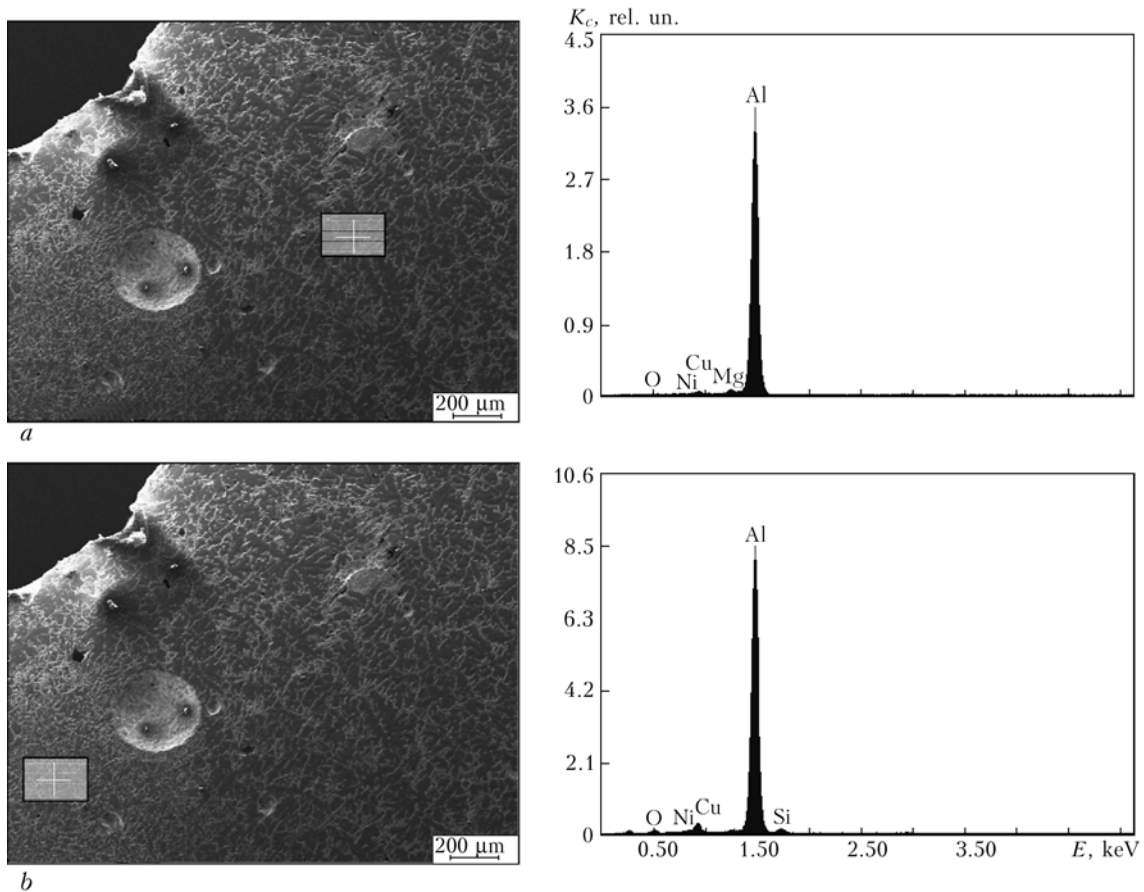


Figure 3. Microstructure and results of EDAX analysis of HAZ (a) and weld metal (b)

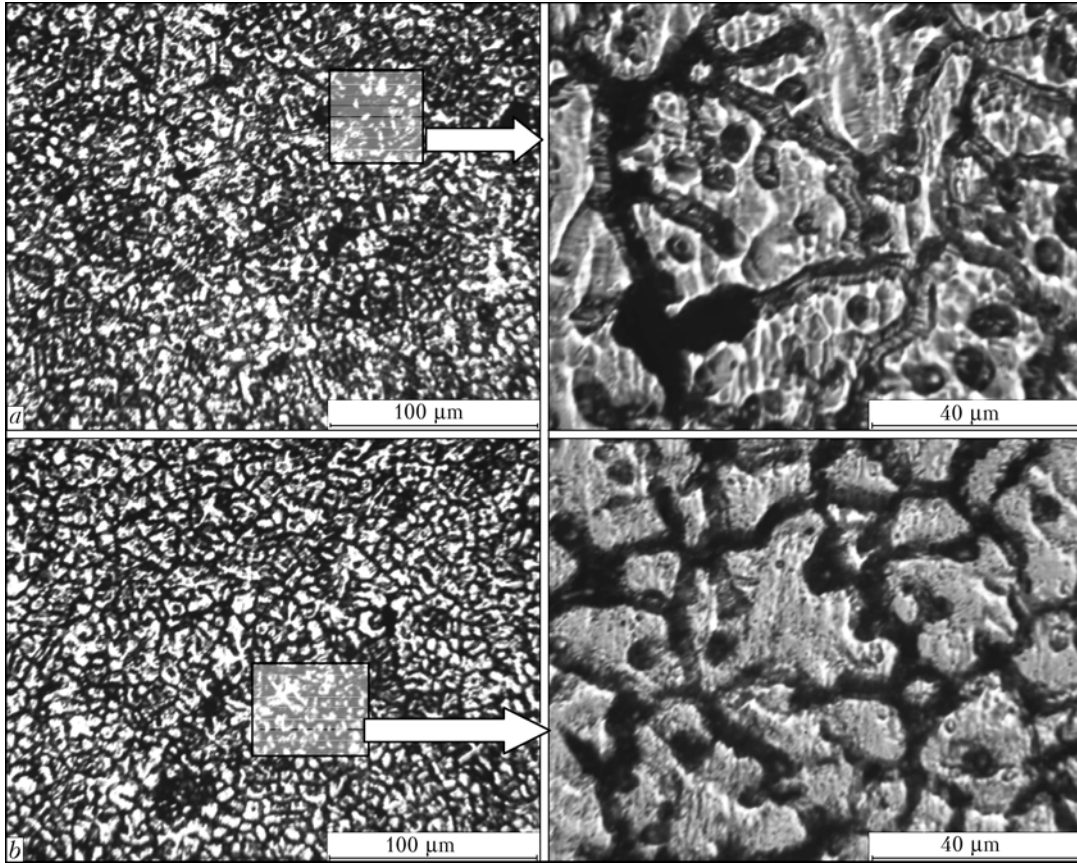


Figure 4. Weld metal optical micrographs at 50 (a) and 100 (b) Hz pulse frequency

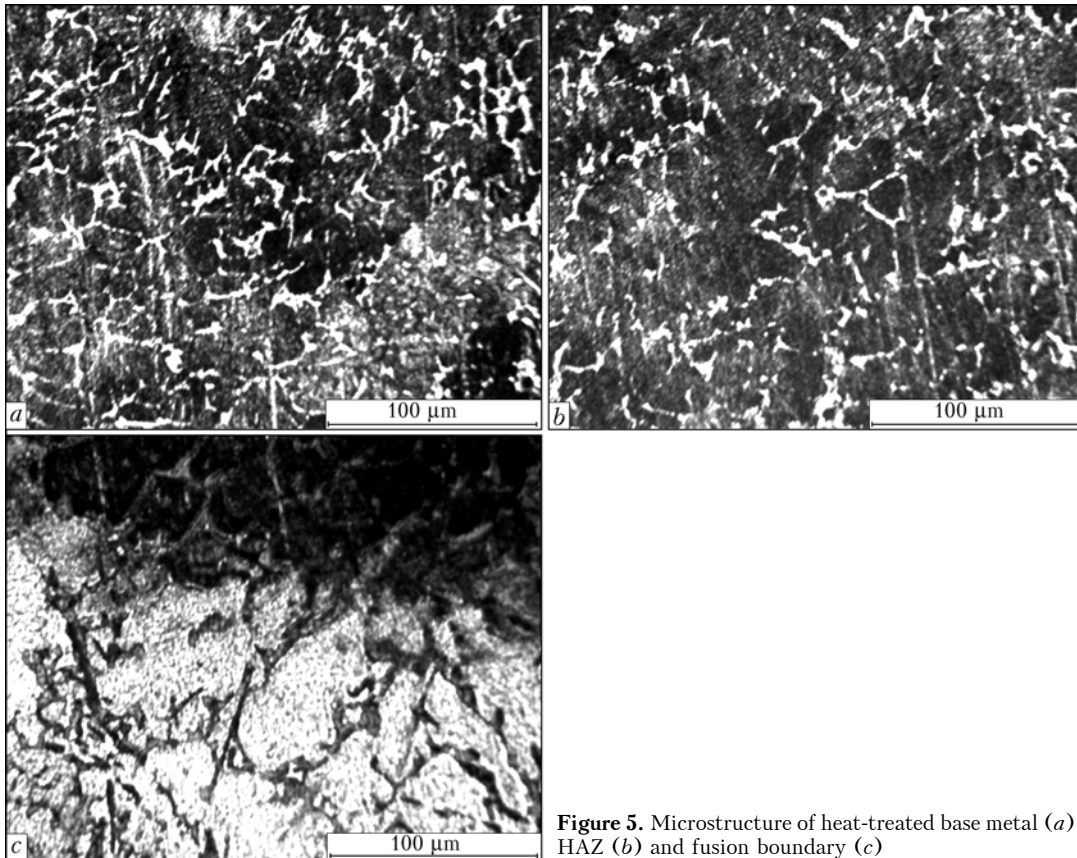


Figure 5. Microstructure of heat-treated base metal (a), HAZ (b) and fusion boundary (c)

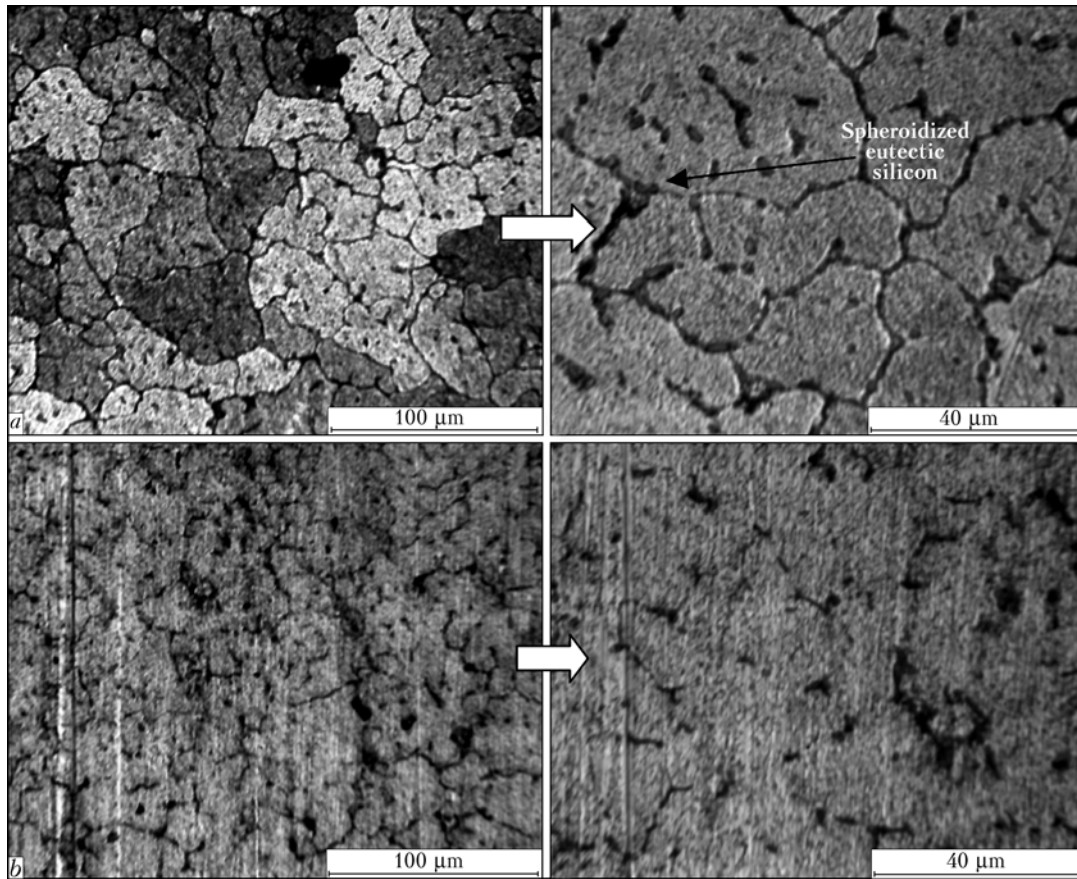


Figure 6. Microstructure of heat-treated weld metal produced at 50 (a) and 100 (b) Hz pulse frequency

EDAX analysis of HAZ and weld metal is shown in Figure 3. Results of image analysis of different regions of welded joints in as welded and heat-treated conditions are shown in Table 1. EDAX analysis of HAZ (94.89 % Al, 2.0 % Cu, 1.10 % O₂, 1.55 % Mg, 0.46 % Ni) (see Figure 3, a) is indicating somewhat lower concentration of alloying elements probably due to homogenization and dissolution of alloying element rich phases (Figure 1, b). EDAX analysis of weld bead (84.29 % Al, 6.41 % Cu, 3.37 % O₂, 0.60 % Mg, 1.99 % Ni, 3.16 % Si) showed evidence of silicon and copper in weld metal indicating dilution caused by melting of base metal and mixing with filler metal (Figure 3, b).

Pulse parameters have also been found to affect the microstructure of welded metal. Joints produced using 100 Hz pulse frequency showed finer structure than that at 50 Hz as evident from both low and high magnification micrographs (Figure 4). These observations are in agreement of earlier finding [2–4, 9–11]. PWHT-T6 of welded joints showed significant change in microstructure of all the regions, namely base metal, HAZ, fusion boundary and weld metal (Figures 5 and 6). In general, heat treatment led to the reduction in fraction of second phase crystals (see Figure 6). The microstructure of postweld heat-treated samples showed that it leads to dissolution of low melting phases along the grain boundary, at the same time spheroidization of eutectic silicon in weld metal also

takes place. Reduction in fraction of second particles and fine precipitates from weld metal and HAZ should reduce the microhardness.

The microhardness of weld bead produced by using 100 Hz pulse frequency was found to be higher compared to that produced by using 50 Hz pulse frequency (Table 2). The increase in weld bead hardness can be due to the refinement of α -Al grains of weld metal at higher pulse frequency. The hardness variation with distance from weld center is shown in Figures 7, 8. It can be seen from Figure 7 that the effect of pulse

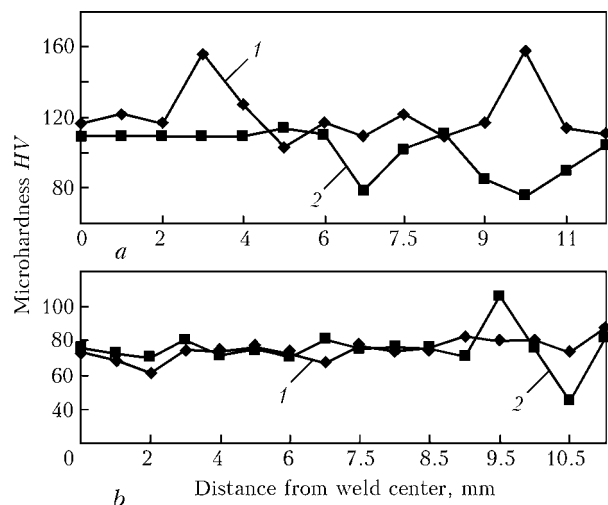


Figure 7. Variation in microhardness of welded joint produced using 100 (1) and 50 (2) Hz pulse frequencies in as welded (a) and postweld heat-treated conditions (b)

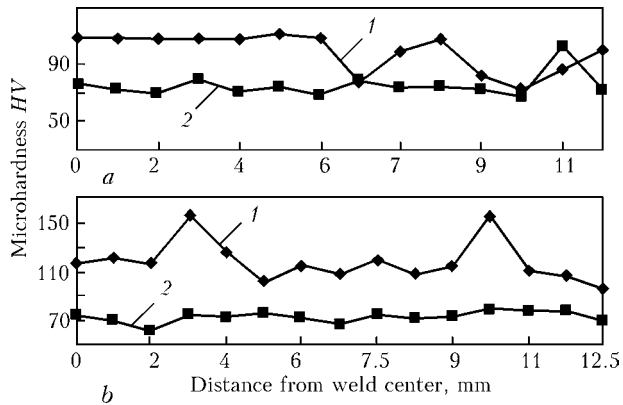


Figure 8. Variation in microhardness of welded joint in as welded (1) and heat-treated conditions produced using 50 (a) and 100 (b) Hz pulse frequency

frequency on microhardness is more in as welded condition than that in heat-treated conditions. However, effect of PWHT on microhardness from the weld center to the base metal was clear and predominant (see Figure 8). It can be observed that hardness decreases appreciably after PWHT. The reduction in hardness can be attributed to the reversion and overaging of the precipitates close to the fusion line and in the HAZ, as Al-Cu alloys are known to have a tendency to overage during welding [2]. The reduction in hardness can also be attributed to the coarsening of aluminium grains and dissolution of second phase particles in matrix of aluminium. The hardness of weld bead in heat-treated condition was found lower compared to that in as welded condition for both pulse frequencies. Moreover, PWHT increased the uniformity in hardness values of weld bead and HAZ.

CONCLUSIONS

Fraction of alloying element rich low melting second phase present along the grain boundary decreases approaching from the base metal to the fusion boundary.

Higher pulse frequency of 100 Hz showed finer grain structure of weld metal as compared with that at low pulse frequency 50 Hz.

Table 2. Microhardness of weld metal of 2218 alloy welded joint

Specimen number	f_{pulse} , Hz	Duty cycle, %	Microhardness, HV	
			As welded	Heat-treated
1	100	35	122.2	71.2
2	50	30	109.8	74.25

Heat treatment led to significant reduction in fraction of second phase constituents in HAZ and weld metal, and spheroidization of the eutectic silicon took place.

PWHT results in significant reduction in hardness of weld metal and HAZ but it increases the uniformity in hardness distribution from base metal to fusion boundary.

- Dudas, J., Handins, F.R. (1966) Preventing weld cracks in high strength aluminum alloys. *Welding J.*, **6**, 241-249.
- Kou, S. (2003) *Welding metallurgy*. 2nd ed. New York: John Wiley & Sons, 263-294, 303-313.
- Ma, T., Den Ouden, G. (1999) Softening behaviour of Al-Mg-Zn alloys due to welding. *Materials Sci. and Eng. A*, **266**, 198-204.
- Rao, K.P. (2001) Fusion zone grain refinement in GTA welds using magnetic arc oscillation and current pulsing. In: *Proc. of Nat. Conf. on Recent Advances in Materials* (2001, Sept. 7-8), 176-196.
- Rao, K.S.R., Reddy, M.G., Kamaraj, M. et al. (2005) Grain refinement through arc manipulation techniques in Al-Cu welds. *Materials Sci. and Eng. A*, **404**, 227-234.
- Haug, C., Kou, S. (2004) Liquefaction cracking in full penetration Al-Cu welds. *Welding J.*, **2**, 50-58.
- Haug, C., Kou, S. (2004) Liquefaction mechanisms in multi component aluminum alloys during welding. *Ibid.*, **10**, 211-222.
- Gupta, R.K., Narayan Murty, S.V.S. (2006) Analysis of crack in aluminium alloy AA2219 weldment. *Engineering Failure Analysis*, **13**, 1370-1375.
- Manti, R., Dwivedi, D.K., Agarwal, A. Pulse TIG welding of two Al-Mg-Si alloys. *Materials Eng. and Performance* (accepted).
- Manti, R., Dwivedi, D.K., Agarwal, A. (2008) Microstructure and hardness of Al-Mg-Si weldments produced by pulse GTA welding. *Int. J. Advance Manufacturing Techn.*, **36(3/4)**, 269-263.
- Manti, R., Dwivedi, D.K. (2006) Influence of pulse TIG welding parameters on microstructure and microhardness of Al-Mg-Si alloys weld joints. In: *Proc. of Int. Conf. on Advances in Materials Processing and Characterization* (Chennai, Aug. 28-30, 2006), 524-531.



EFFECT OF THE COMPOSITION OF PLASMA AIR-GAS MIXTURE ON PARAMETERS OF THE PLASMATRON JET

V.N. PASHCHENKO

National Technical University of Ukraine «Kiev Polytechnic Institute», Kiev, Ukraine

The possibility of controlling energy parameters of plasmatrons with a combined energy supply is studied. It is shown that changing the content of a hydrocarbon component in the initial plasma mixture allows changing over a wide range the absolute value of the plasmatron power and its specific energy parameters during operation, as well as influencing the oxidation-reduction potential of a working medium and conditions of electrode operation. Several possible modes of operation of plasmatrons with the hydrocarbon component in the initial plasma mixture are proposed, allowing changing conditions of the technological process by using the same unchanged design.

Keywords: *deposition of coatings, surface treatment, plasmatrons, combined energy supply, control of plasmatron power, oxidation-reduction potential of environment*

Plasma heat sources (plasmatrons) are widely applied in surface engineering processes for deposition of coatings and surface treatment of parts to control properties of the surface layer and restore initial dimensions of worn out parts.

Arc plasmatrons have received the widest acceptance. While interacting with a gas flowing about the arc, the electric arc discharge gives part of its energy to the gas, which is sufficient to transform material into a state of the low-temperature plasma. Traditionally, for this the use is made of neutral and inert plasma gases, as well as their mixtures with gas components that increase the general level of enthalpy of the plasma flow.

In the 1960s, the Gas Institute of the National Academy of Sciences of Ukraine started the efforts on development of heating devices using electric amplification of flame, i.e. electric gas torches, and then arc plasmatrons operating with the fuel mixtures of air and hydrocarbon gases (air-gas mixtures). Utilisation of mixtures of air with the hydrocarbon gases (methane, propane-butane, natural gas) allows controlling the oxidation-reduction potential of an environment wherein a material is treated, and supplying an extra energy with a fuel component of the plasma gas.

The noted property of the plasma flows generated from air-hydrocarbon gas mixtures makes the plasma processes for treatment of materials and surfaces of parts advantageous over the traditional processes realised by using inert and neutral gases.

Plasma jets of the air-gas plasmatrons have more filled temperature and velocity profiles at all distances of material treatment, which is provided by a heat released in burning down of fuel components (CO, H₂) of a high-temperature gas flow with inflow of air from the environment. Uniform distribution of the above parameters within the work volume of the jet permits a more efficient utilisation of the initial ma-

terial and its active protection from interaction with oxygen of the air inflow. Spraying with air-gas plasmatrons can be a realistic alternative to supersonic flame processes. Dramatic increase of a temperature level of the process allows substantial widening of ranges of the materials used to form coatings. At the same time, this process retains the possibility of controlling the oxidation-reduction potential of the material treatment environment, which is characteristic of the flame processes, as well as the high rates of the high-temperature gas flow typical of the supersonic flame processes.

Plasmatrons using fuel components in a composition of the initial plasma mixture are high-temperature heat sources with a combined energy supply. The total energy is fed to a working medium (gas flow) from the electric energy source via the electromagnetic field, as well as from the products of combustion of the fuel components of the plasma mixture in the form of a thermal energy.

The process of transfer of the electric energy is determined by the arc current, volt-ampere characteristic of the device and efficiency, and is realised mostly within the plasmatron structure. The share of this component of the energy flow amounts, as a rule, to 85–95 %, and is decisive for the energy balance of the working medium.

There is also the thermal combustion energy, which is formed along with the main component of the energy flow. Both components of the energy balance are greatly affected by the content of a hydrocarbon (fuel) component of the initial plasma mixture.

Effect of the fuel component on power of the air-gas plasmatrons was studied in [1–4].

Dependence of variations in the intensity of the electric field along the arc column upon the content of the hydrocarbon components in the initial plasma mixture was experimentally determined. Formula of a generalised volt-ampere characteristic allows for the integrated effect of the hydrocarbon content on the arc voltage through complex of the type of $(1 + n)^m$, where n is the hydrocarbon content of the mixture, vol.%, and m is the empirical coefficient, whose value varies from 0.530 to 0.778 depending upon the design



of a plasmatron [1]. It was noticed that increment of the arc voltage depends upon the point of entry of the hydrocarbon component. It is on this fact that the method put forward in study [4] is based on. Study [5] presents a quantitative estimation of the effect of the hydrocarbon component on the integrated value of the arc voltage (including at a low content of hydrocarbon).

However, no comprehensive analysis of the effect on energy parameters of the plasma jet by the hydrocarbon component is available, and no basic principles of control of these parameters have been formulated, including those allowing for the oxidation-reduction capabilities of a working medium.

The possibility of controlling energy parameters of the plasmatrons by changing the amount and point of entry of the hydrocarbon component of the plasma mixture was investigated on an experimental bench using natural gas as a hydrocarbon (up to 16 vol.%, or 4–5 vol.% propane-butane). Investigations were carried out by using linear two-electrode plasmatrons with vortex space stabilisation of the arc and auto-gas-dynamic stabilisation of its length. It was established [5] that adding the natural gas (methane) to the initial plasma air substantially changes the arc burning conditions. This shows up both in rise of a general level of the arc voltage and in variations of the character of distribution of heat losses and arc current along the arc channel. The above effects occur even at an insignificant content (less than 1 vol.%) of the natural gas in the initial plasma mixture.

Figure 1 shows characteristic stages (*I–IV*) of variations in the arc voltage with increase in the natural gas content of the plasma mixture.

Dramatic (10–16 %) increase in the arc voltage takes place at stage *I* with transition from air to a mixture with a hydrocarbon content of not more than 0.2–0.7 vol.%.

At the hydrocarbon content of the mixture increased to 4–5 vol.% (stage *II*), the rate of growth of the voltage considerably decreases, and at 5–9 vol.%

(stage *III*) the value of the voltage remains almost unchanged.

Enrichment of the mixture with hydrocarbon by more than 10 vol.% (stage *IV*) causes increase in the arc voltage at a rate of about 3 % of the voltage per 5 vol.% of the hydrocarbon. Such a dramatic increase in the arc voltage with an addition of the insignificant amount (vol.%) of the hydrocarbon component may have several explanations [6, 7]. The most probable explanation is the effect on the intensity of the electric field by changes in the arc burning conditions as a result of a radial distribution of components of the plasma mixture under the influence of thermal diffusion [6].

Assuming the presence of the substantial effect on distribution of components in the arc channel by thermal diffusion in the case of application of the N–C–O–H system gas mixtures, it can be considered that the arc transforms from the «nitrogen» into «hydrogen» one with an addition of hydrocarbon. This causes restructuring of a conducting region of the gas flow: diameter of the arc columns increases, while the temperature and specific heat flow decrease. Drop of electrical conductivity of the near-wall layer of gas changes the arc shunting conditions. The arc elongates, other conditions being equal [7].

Therefore, it can be stated that increase in the arc voltage with an addition of the hydrocarbon component occurs in two ways: by predicted increase in the intensity of the electric field (the arc has become the «hydrogen» one), and by increase in the arc length.

Results of investigation into the effect of the arc length on drop of the arc voltage indicate that elongation of the arc by fixed 20–40 % can lead only to a 4–6 % increase in integrated value of the voltage (allowing for a 20–25 % increase in the intensity of the electric field in the main region of the arc column), compared with operation in plasma-forming air. Therefore, the experimentally established 7–25 % growth of the arc voltage with an addition of the hydrocarbon component occurs mostly because of a change in local values of the intensity of the electric field in characteristic regions of the electric arc.

It can be concluded on the basis of the above-said that the first energy mode of operation of the plasmatron with a combined energy supply can be a mode with an addition of about 1 vol.% hydrocarbon (about 0.3 vol.% propane-butane) to the initial plasma-forming air. At the same time, the coefficient of consumption of oxidiser of the initial plasma mixture is $\alpha = 15–20$, i.e. increase in power has almost no effect on the oxidation-reduction potential of the plasma jet — the jet of the plasmatron remains oxidising. Transition to such a plasma mixture due to a change in the conditions of existence of the arc discharge allows a stepwise increase in the arc voltage (and, hence, the plasmatron power) by 8–16 % without increase in the current load on electrodes. The hydrocarbon component of the plasma-forming environment

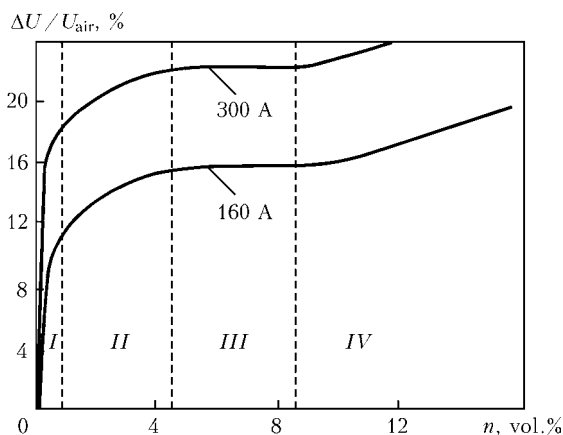


Figure 1. Dependence of the degree of increase in plasmatron arc voltage, $\Delta U/U_{\text{air}}$, upon hydrocarbon content n of initial plasma mixture: ΔU — increase in the arc voltage with addition of the fuel component, compared with its initial value in air; U_{air} — arc voltage in operation in air; *I–IV* — see explanations in the text

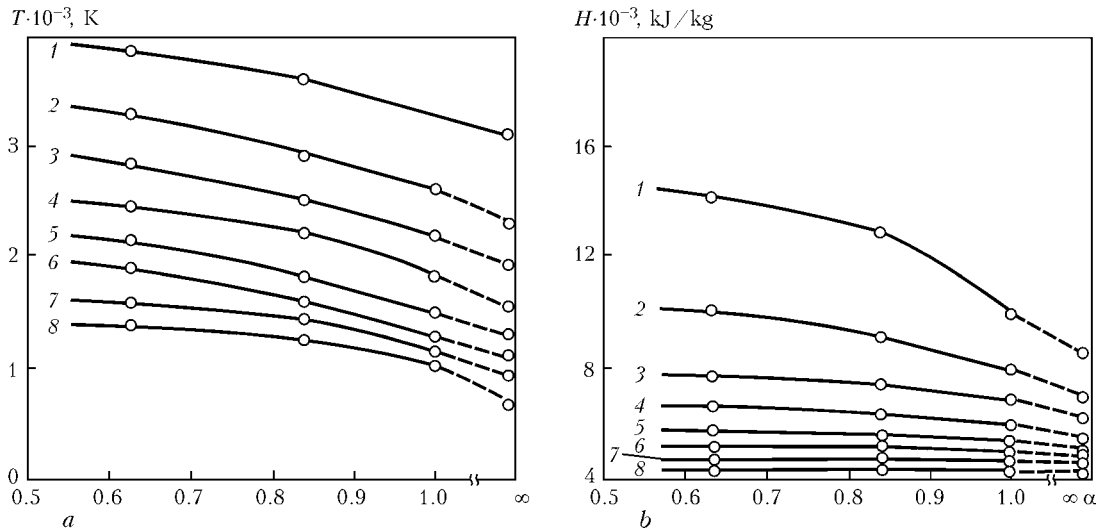


Figure 2. Dependence of temperature T (a) and enthalpy H (b) upon coefficient α of consumption of oxidiser in the plasma mixture at longitudinal axis of the plasma jet (current $I = 200$ A, plasma mixture flow rate $Q = 6.25$ m³/h, plasmatron power $P = 24$ kW) at distances $L = 40$ (1), 60 (2), 80 (3), 100 (4), 120 (5), 140 (6), 160 (7) and 180 (8) mm

in this case is just a tool to control the overall power of the generator.

Addition of up to 1 vol.% hydrocarbon to the plasma mixture has no substantial effect on the level of a heat flow to the thermochemical cathode (within the measurement error), although its operation conditions change because of a change in chemical composition of components of the gas mixture in the near-electrode arc region.

The heat flow to an output electrode grows, this being related to elongation of the arc within the anode region. In this case, no intensification of erosion of the anode material within the zone of fixation of the electrode spot takes place.

In the case under consideration the rate of growth of the plasmatron power can be controlled by using a separate supply of components of the plasma mixture, or by changing the point of entry of hydrocarbon to the arc channel.

Application of plasmatrons with a combined energy supply for deposition of coatings from the materials characterised by a sufficiently high coefficient of difficulty of melting [8] and sensitivity to chemical composition of the environment, wherein they are heated and accelerated, is expedient with increase in the content of the hydrocarbon component up to the values close to the stoichiometric ones (8–10 vol.% methane, or $\alpha = 1$). This is the second energy mode of operation of the plasmatron.

In addition to a predicted 16–20 % increase in power, this mode makes it really possible to control size of the active zone of the plasma jet, its chemical composition and process of transfer of energy to the material that forms a coating. For example, a change in the coefficient of consumption of oxidiser of the plasma mixture from $\alpha = \infty$ (air) to 1 leads to a 3–8 % increase in enthalpy at the longitudinal axis of the plasma jet at distance $L = 50$ –200 mm from exit section of the plasmatron nozzle, and 20–25 % increase at $L < 40$ mm (Figure 2). This is accompanied by increase

in temperature of the plasma jet, and at $L = 50$ –130 mm it is 8–10 % of the initial one (in air).

The proportion of fuel and oxidation components in the initial plasma mixture close to the stoichiometric one allows the content of oxygen in the active zone of the plasma jet (zone of heating of a spraying material) to be decreased to some extent. However, the content of the reduction components in the high-temperature gas flow is obviously insufficient to protect a spraying material from oxygen, which leaks in from the environment (Figure 3).

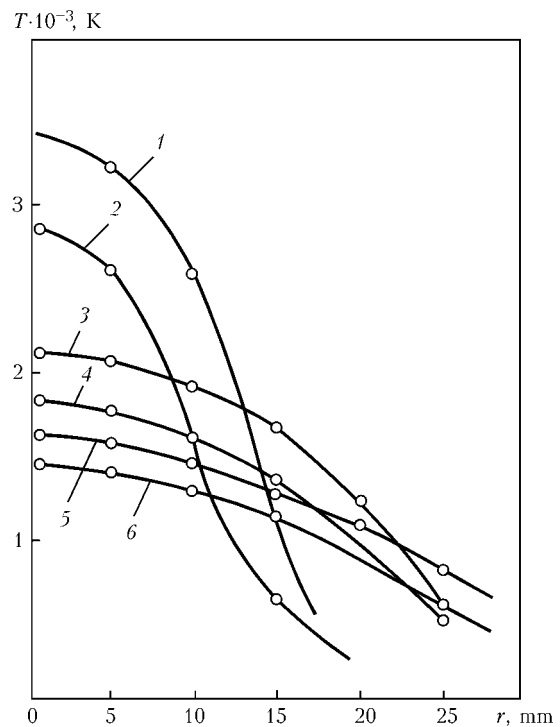


Figure 3. Distribution of temperature in transverse section of the plasma jet with variations in composition of the plasma mixture and distance $L = 50$, 100 and 150 mm ($I = 200$ A, $Q = 6.25$ m³/h, $P = 24$ kW): 1, 3, 5 — $\alpha = 0.63$; 2, 4, 6 — $\alpha = 1$; r — distance from longitudinal axis of the plasma jet to a point under investigation

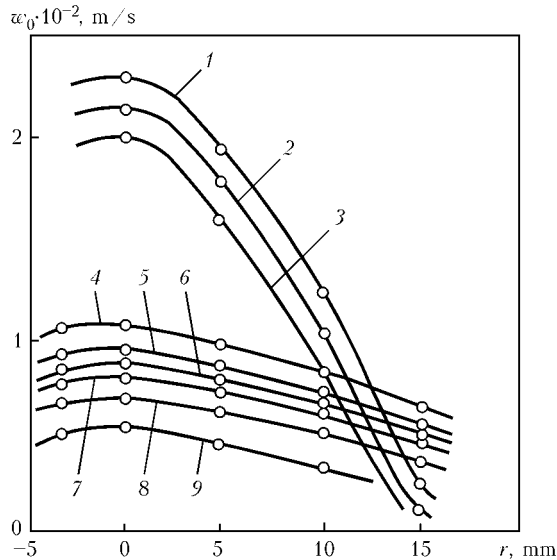


Figure 4. Transverse profile of plasma velocity ω_0 at $L = 50$ mm, $\alpha = 0.63$ (1), $\alpha = 1$ (2), $\alpha = \infty$ (3); $L = 100$ mm, $\alpha = 0.63$ (4), $\alpha = 1$ (5), $\alpha = \infty$ (6); $L = 150$ mm, $\alpha = 0.63$ (7), $\alpha = 1$ (8); $\alpha = \infty$ (9)

Change from the plasma air to its mixture with hydrocarbon with the approximately stoichiometric proportion between the components changes conditions of operation of the plasmatron electrodes. For instance, the absolute value of the heat flow to the thermochemical cathode grows by 6–7 %, while this may lead to intensification of its erosion in the case of insufficient cooling.

And on the contrary, the anode operation conditions become more favourable in terms of erosion, which is attributable to a substantial deceleration of the process of oxidation of copper within the zone of fixation of the reference arc spot. According to the opinion of authors of study [4], this also leads to a change in the character of fixation of the arc to the

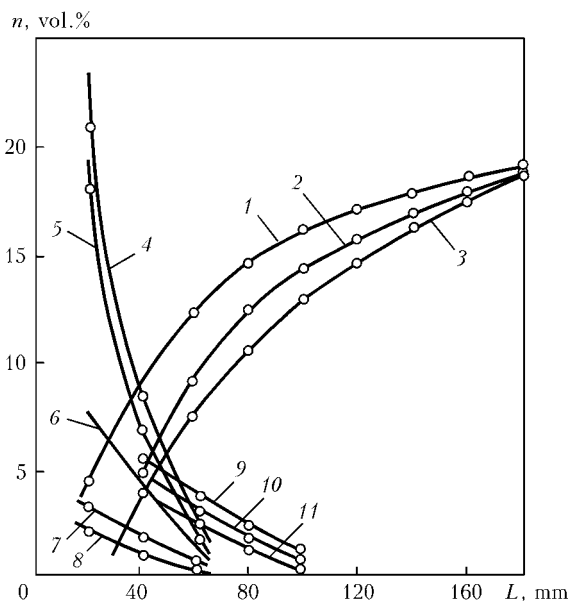


Figure 5. Effect of initial composition of the gas mixture on content of characteristic components in plasma — O_2 (1, 2, 3), [H] (4, 5, 6), H_2 (7, 8), CO (9, 10, 11) in longitudinal section of the plasma jet: $\alpha = 1$ (1, 6, 9); $\alpha = 0.84$ (2, 5, 7, 10); $\alpha = 0.63$ (3, 4, 8, 11)

anode, where a considerable part of the current is short-circuited via the diffusion discharge.

Further increase in the content of hydrocarbon in a mixture (rich mixtures) leads to increase in a general level of enthalpy (the third characteristic energy mode of operation of a plasma heater). Change in the oxidiser consumption coefficient from 1 to 0.63 leads to an 8–10 % increase in enthalpy at a distance from 50 to 200 mm, and to a 30–40 % increase at $L \leq 40$ mm (see Figure 2).

At this stage the plasma jet temperature substantially grows (by 30–40 % of the initial value) at a distance of 50–130 mm, which can be explained by an extra heat released in combustion of the mixture components with an inflow of oxygen from the environment.

Despite a lower calculated mean-weight temperature of plasma at the exit section of the plasmatron nozzle, gas mixtures with a higher hydrocarbon content are characterised by an increase in values of the local temperature of enthalpy in a cross section of the jet (see Figure 3) at a distance of 3–5 outer diameters of the nozzle to 20–25 ones.

Velocity of the plasma jet grows with increase in the hydrocarbon content because of increase in volume of the initial mixture dissociation products. Increase in the velocity persists at all distances of the material treatment (Figure 4).

Therefore, change from a complex mixture of non-fuel molecular gases (air plasma jet) to a mixture with the fuel component causes increase in the active zone of the plasma jet, wherein increase in heating and acceleration of movement of the dispersed material may amount to 1.5–2 times, and increase in its volume may amount to 4–5 times.

Along with increase in energy characteristics of the plasma jet, a rich mixture of hydrocarbon with air makes it possible to promptly, during the coating deposition process, change the oxidation-reduction potential of the environment wherein a dispersed material is treated. This becomes possible because of a substantial increase in content of the reduction components (CO , H_2) in the plasma jet with enrichment of a mixture with hydrocarbon.

Figures 5 and 6 show variations in the content of the main components in longitudinal and transverse sections, respectively, of the plasma jet, which is generated from a mixture of air and methane. As seen from Figure 6, length of the reduction region of the plasma jet (dashed region) depends upon the content of the hydrocarbon component in the initial mixture. In this case, the oxygen content decreases with increase in the volume fraction of hydrocarbon in the initial mixture.

The presence of a substantial volume fraction of hydrocarbon in the initial plasma mixture changes the total energy balance of the process of conversion of the electric energy and energy of a fuel component into the thermal energy of the plasma jet. Transition to enriched mixtures ($\alpha < 1$) does not only lead to a



further increase in value of the thermal energy of the jet, but even causes its decrease due to a consumption of heat for chemical transformations in the high-temperature gas flow. This energy is released outside the plasmatron in the bulk of the plasma jet with burning down of the plasma mixture components.

Decrease in the oxidiser consumption coefficient causes a marked increase of the heat flow to the thermochemical cathode. Whereas transition from air to a stoichiometric mixture raises the level of the overall heat flow to the cathode by 6–7 %, with a decrease in the oxidiser consumption coefficient from 0.5 to 0.4 this raising amounts to 25–37 %. Cooling conditions being kept unchanged, the high level of the heat flow leads, as a rule, to a 20–25 % decrease in life of the thermochemical cathode.

As noted above, the anode operation is characterised by a dramatic decrease in the rate of erosion [4]. The common opinion is that it is the oxide films on the surface of the arc channel that cause an increased erosion of copper electrodes in oxygen-containing plasma-forming environments [2]. The reduction components of the gas flow (CO, H₂) combine oxygen, thus preventing oxidation of copper within the reference arc spot fixation zone.

CONCLUSIONS

1. Combined energy supply to the plasma gas considerably widens the possibilities of controlling size, structure and absolute values of parameters of the active zone of the plasma jet.

2. An insignificant (0.2–0.7 vol.%) content of hydrocarbon hardly affects chemical composition of a work medium, but at a 10–16 % change in the arc burning conditions it increases the plasmatron power within the ranges of the existing design (the current load on electrodes being preserved).

3. Increasing the energy input into the plasma gas by 15–20 % due to increase in the fuel component content of the plasma mixture causes a 30–40 % increase in the gas temperature at a distance of 50–130 mm (compared with operation in air), and almost 4–5 times increase in volume of its active zone.

4. For efficient application of plasmatrons with a combined energy supply in surface engineering, it is necessary to further investigate the effect of hydro-

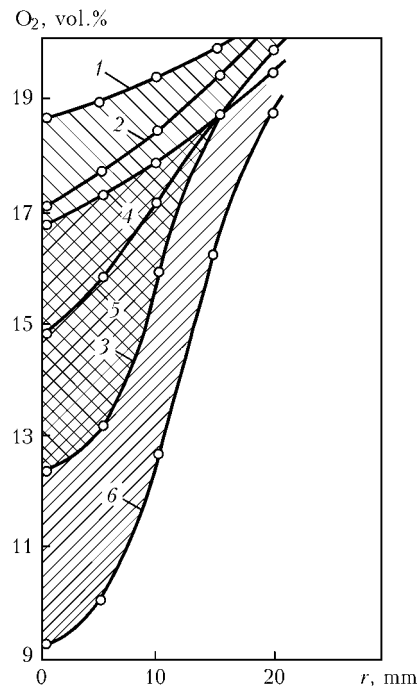


Figure 6. Effect of initial composition of the gas mixture on content of oxygen in transverse section of the plasma jet: $\alpha = 1$ at $L = 150$ (1), 100 (2), 50 (3) mm; $\alpha = 0.63$ at $L = 150$ (4), 100 (5) and 50 (6) mm

carbon on the plasma jet temperature and velocity profiles at $\alpha = 15$ –20.

1. Pashchenko, V.M. (1998) Investigation of jets of the plasmatron functioning with plasma-forming mixtures of the C–N–O–H system for deposition of coatings. In: *Proc. of Int. Conf. on Advanced Engineering and Technology of Machine-Building, Instrument-Making and Welding Production* (Kyiv, 25–28 May, 1998). Vol. IV. Kyiv: NTUU KPI, 333–337.
2. Pashchenko, V.M. (2001) *Equipment for thermal deposition of coatings*: Manual. Kyiv: Politekhnika.
3. Pashchenko, V.N. (1998) Particularities of application of multi-component gas mixtures in plasmatrons for coating deposition. *Avtomatich. Svarka*, **6**, 23–26.
4. Petrov, S.V., Karp, I.N. (1993) *Plasma air-gas spraying*. Kiev: Naukova Dumka.
5. Pashchenko, V.M., Solodky, S.P. (2003) Influence of hydrocarbon component on energy parameters of plasma sprayers functioning with mixtures of air with hydrocarbon. *Visnyk Shhidnoukr. Nats. Un-tu im. V. Dala*, Issue 11(69), 64–68.
6. (1979) *Principles of calculation of linear-scheme plasmatrons*: Operative-inform. document. Ed. by M.F. Zhukov. Novosibirsk: ITF.
7. Donskoj, A.V., Klubnikin, V.S. (1979) *Electric-plasma processes and units in machine-building*. Leningrad: Mashinostroenie.
8. Borisov, Yu.S., Borisova, A.L. (1986) *Plasma powder coatings*. Kiev: Tekhnika.

CONTROL OF MANIPULATION ROBOT FORCE ACTION

G.A. TSYBULKIN

E.O. Paton Electric Welding Institute, NASU, Kiev, Ukraine

The non-traditional approach towards the solution of problem of control of the manipulation robot force action on contact surface under the conditions of its free location in the working space of robot has been proposed. The algorithm providing the stabilization of a force action at a desirable level has been outlined.

Keywords: manipulation robots, workpiece being treated, contact surface, force action stabilization, correcting algorithms

During many technological operations performed using manipulation robots it is necessary to realize the physical contact of a working element with a workpiece being treated. Sometimes, for example, during cutting of tacks before subsequent welding of parts or during grinding and subsequent etching of welds to reveal hot microcracks it is very important for the working element in the process of performance of such operations to be pressed against the contact surface with a certain force. To provide the above-mentioned condition, the necessity in the force action automatic control arises.

At least, two basically different approaches towards the solution of the problem are known. The first one is based on the so-called principle of movements separation [1, 2] consisting in the fact that one part of drives of robot-manipulator is supposed to be used to realize the movement along the preset trajectory, and another one — to organize the preset forced action. This approach envisages the increase in degrees of freedom of manipulator by adding links, that leads naturally to the significant complication of the robot.

The second approach is based on the idea of movements separation on the programme level [3–5], moreover, in a way to provide the robot movement along the preset trajectory and required force on the contact surface of the workpiece by the same drives. This approach is more attractive, however, there are another kind of problems here, connected with the fact that information about the force action F , coming from a force sensor, arranged in the working element of the robot, is sometimes insufficient for realisation of this force action control. This is due to the fact that force direction in a general case may not coincide with the direction of one of the axes of the robot coordinate system, in which the trajectory of its movement is programmed. Therefore, it becomes unclear how to «split» the signal being received about the real force action F into constituents on coordinates and how to correct it later.

In the present article the procedure was applied for the solution of this problem, which was used earlier by us in work [6] for the automatic correction of trajectory of the manipulation robot movement. Its

main principle consists in presetting the movement trajectory and required force during programming not in the coordinate system of a robot (as it is usually done), but in the coordinate system connected with the trajectory itself using the so-called Frenet reference point [7]. In this case the possibility is appeared to orient always one of the coordinate axes of reference point along the supposed force action and to plot the trajectory of movement or its fragments in the plane normal to the selected axis. To maintain the preset force at the certain level it is sufficient now to use a single-channel stabilization system independently of a spatial position of contact surface within the working space of the robot.

Let us consider this possibility more in detail. Frenet reference point is connected with the robot trajectory of movement so that in each nodal point P_i ($i = 1, 2, \dots$) of this trajectory the axis u_1 of the given reference point is directed along the tangent (Figure 1), axis u_2 — along the principal normal, axis u_3 — along the binormal. The coordinate vector $\mathbf{u}_i^R = [u_{i1}^R, u_{i2}^R, u_{i3}^R]^*$, characterizing the location of some point R in the system of reference of the i -th reference point $P_i u_{i1} u_{i2} u_{i3}$ and vector of c coordinates $\mathbf{x}^R = [x_1^R, x_2^R, x_3^R]^*$, characterizing the location of the same point R in the basic reference system of robot $Ox_1 x_2 x_3$ are connected by the relation

$$\mathbf{u}_i^R = \mathbf{T}_i \mathbf{x}^R,$$

in which the matrix of homogeneous transformation \mathbf{T}_i has a form

$$\mathbf{T}_i = \begin{bmatrix} \mathbf{L}_i & \mathbf{b}_i \mathbf{u}_i^R \\ 000 & \mathbf{1}_{\mathbf{q}} \end{bmatrix},$$

where \mathbf{L}_i is the orthogonal matrix specifying the orientation of Frenet reference point; \mathbf{b}_i is the column vector specifying the location of origin of coordinates of this reference point as regards to the system of reference $Ox_1 x_2 x_3$. Sign (*) in the upper right corner designates the operation of transposition.

Concerning the link between the coordinates of R point, specified in the basic reference system, and controllable (or so-called generalized) coordinates of robot q_j , $j = 1, 2, \dots, n$, then it is preset by relation $\mathbf{x}^R = \mathbf{A}(\mathbf{q}^R)$, where $\mathbf{q}^R = [q_1^R, q_2^R, \dots, q_n^R]^*$; n is the number of degrees of manipulator freedom; $\mathbf{A}(\cdot)$ is the function vector generated by its kinematics.

Now it is evident that if to orient the working element of a robot in a way that its axial line and force action $F(t)$ were directed parallel to the axis u_3 (Figure 1), then the real feasibility is appeared to realize the control of this force action by change of one coordinate u_3 only. The link between the force action $F(t)$ and location of working element relative to the contact surface can be expressed in the form of relationship

$$F(t) = \begin{cases} 0 & \text{at } u_3^R(t) \geq u_{30}^R, \\ -Ku_3^R(t) + F_* & \text{at } u_3^R(t) < u_{30}^R, \end{cases} \quad (1)$$

where $u_3^R(t)$, u_{30}^R are the coordinates of point R (located, for example, on the working element) characterizing, respectively, its current and preset location as regards to the plane u_1u_2 ; K , F_* are the positive constants; t is the current time (it is supposed that working element possesses a required degree of pliability, characterized by value K^{-1}).

It should be noted that in the process of robot movement along the contact surface the friction forces will also arise, but as they are directed along the tangent to the trajectory of movement, i.e. normal to the coordinate u_3 , they will not be considered in this problem. Deviation $\Delta u_3^R(t) = u_3^R(t) - u_{30}^R$ can be determined in any moment of time t by measuring the appropriate distances $d(t)$ and d_0 by using any sensor between point R and contact surface, i.e. $\Delta u_3^R(t) = d(t) - d_0$. Consequently, it is possible to use the following equality for the synthesis of law of control of force action $F(t)$ according to (1)

$$d(t) - d_0 = -K(F(t) - F_0), \quad (2)$$

where F_0 is the preset value $F(t)$.

The problem of control of force action $F(t)$ will be formulated now in the form of a simple requirement

$$|d(t) - d_0| \leq \varepsilon, \quad (3)$$

guaranteeing the stabilization of force action at the desired level $|F(t) - F_0| \leq \varepsilon K^{-1}$, where ε is the positive value.

The geometric relation (3) specifies the layer of thickness 2ε , located between two planes of level $u_{30} + \varepsilon$ and $u_{30} - \varepsilon$ in the system of Frenet coordinates system, in the 3D space. Therefore, the problem stated above can be interpreted as a problem of stabilization of movement of a characteristic point R inside the specified layer.

Thus, to stabilize the force exerted on the contact surface during the movement of robot along the preset trajectory, it is enough to possess information about the current distance $d(t)$ from the point R to the contact surface, and also the algorithm of correcting control of robot movement along the coordinate u_3 .

The equipping of manipulation robot with a distance sensor does not encounter usually great difficulties. As to the design of algorithm of correction of a force action, so it is mostly defined by the capabilities

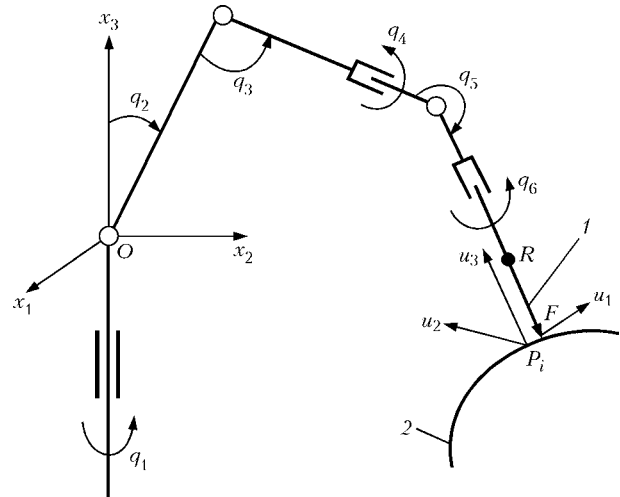


Figure 1. Schematic representation of manipulation robot of anthropomorphic type with six levels of freedom interacting with environment: 1 — working element of robot; 2 — contact surface (for designations see the text)

of software of a definite manipulation robot. In particular, for the robots of PUMA family, the software of which does not support some operations on the coordinates, it is preferably to derive the law of a stabilizing control in the form of a recurrent relationship

$$u_3(k) = u_3(k - 1) + \Delta u_3(k), \quad (4)$$

where

$$\Delta u_3(k) = \begin{cases} h & \text{at } d(k - 1) < d_0 - \varepsilon, \\ -h & \text{at } d(k - 1) > d_0 + \varepsilon, \\ 0 & \text{at } d_0 - \varepsilon < d(k - 1) < d_0 + \varepsilon. \end{cases} \quad (5)$$

Here h is the length of correction pitch ($h \leq \varepsilon$), $k = 1, 2, \dots$ is the index, characterizing discrete time.

The algorithm (4), (5) verification in the laboratory robotic complex confirmed its sufficiently high efficiency. The stabilization of force action $F(t)$ proceeds too simply: according to the results of measurements of distance d on every previous cycle ($k - 1$) according to the expression (4) the current position of working element $u_3(k)$ is corrected relative to the contact surface. Here, taking into account the expression (2) the force action $F(t)$ is corrected accordingly.

It is necessary to note that, if required, the algorithm (5) can be a little improved by introducing a pitch with adaptively changing length instead of a constant correction pitch length h . However, in this case due to the essential increase in quantity of computing operations some limitations for speed of movement of working element along the preset trajectories can appear.

Thus, having used the Frenet reference point on the stage of programming the robot movements it is possible to solve very simply the problem of stabilization of a force action of a working element on the contact surface in the process of its movement along the preset trajectories. The structure of robot control system with a stabilization circuit is shown in Figure 2.

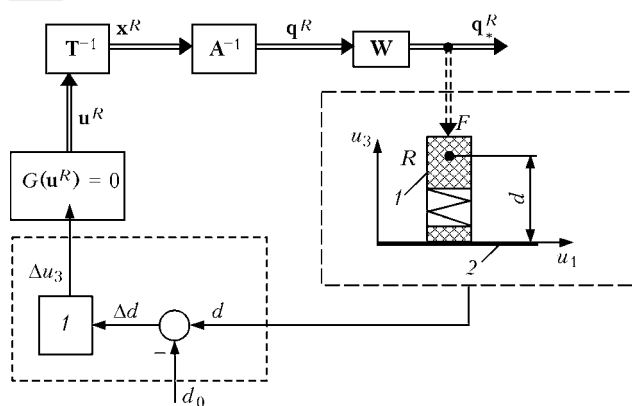


Figure 2. Structure of robot control system with stabilization circuit of force action: 1 — working element of robot; 2 — contact surface; q_s^R — vector of coordinates of actual position of working element; W — matrix of transfer functions of local replicating manipulator systems; $G(u^R) = 0$ — programmed preset trajectory of movement of working element

The distinctive feature of a proposed scheme of stabilization is the fact that, if required, it allows the conductance of simultaneous and independent correction of the robot working element movement trajec-

tory itself in the plane u_1u_2 of system of Frenet coordinates. Such necessity may arise, for example, in the case when due to the large friction forces between working element and contact surface mentioned above, the actual trajectory of movement of working element is inadmissibly deviated from the programmed trajectory.

1. Tsybulkin, G.A. (1995) Two-level coordinating control of manipulation robot with kinematic redundancy. *Problemy Upravleniya i Informatiki*, 3, 143–150.
2. Coife, F. (1985) *Interaction of robot with environment*. Moscow: Mir.
3. Whitney, D.E (1985) Historical perspective and state of the art in robot force control. In: *Proc. of Int. Conf. on Robotics and Automation*, 262–268.
4. Clamroch, H., Wang, D. (1990) Linear feedback control of position and contact force for a nonlinear constrained mechanism. *J. Dyn. Syst. Meas. and Control*, 112(4), 640–645.
5. Zheng, Y.F., Fan, Y. (1991) Robot force sensor interacting with environments. *IEEE Transact. Rob. and Autom.*, 7(1), 156–164.
6. Tsybulkin, G.A. (2000) Situation algorithms of automatic correction of the robot motion path in arc welding. *The Paton Welding J.*, 11, 11–14.
7. Dubrovin, B.A., Novikov, S.P., Fomenko, A.T. (1986) *Current geometry: Methods and propositions*. Moscow: Nauka.

COMPARATIVE TESTS OF WELDING-TECHNOLOGICAL PROPERTIES OF INVERTER AND THYRISTOR POWER SOURCES

V.M. ILYUSHENKO¹, G.A. BUTAKOV¹, A.V. GANCHUK¹, V.A. OSTAPCHENKO² and N.A. GORYAJNOV²

¹E.O. Paton Electric Welding Institute, NASU, Kiev, Ukraine

²SSPE «Objedinenie Kommunar», Kharkov, Ukraine

The approach towards determination of technological properties of power sources based on the results of comparative testing the new and earlier applied models of welding equipment is described. The structure and composition of system of acquisition and recording of data about the main parameters, characterizing the properties of welding equipment, are given. The comparative characteristics of power sources VDUCh-500, VD 506 DK, VDUCh-350 and VS 300 B are shown. The testing methods and methods of processing the statistics information obtained during tests are described.

Keywords: arc welding, welding equipment, welding-technological properties of equipment, acquisition system, data recording

In connection with reorientation of many enterprises to the new nomenclature of welding equipment the quantity of its manufacturers has grown significantly. Currently both large and small enterprises begin production of welding power sources (PS), feeding mechanisms and other equipment, often having no experience in that field as well as specialists of a related profile. The consumer often encounters many difficulties in orienting within the wide range of types of welding equipment and in selection of that type which could provide optimum ratio of price and quality. The choice of welding equipment is based either on the principle of customization (the new equipment is selected of similar type as that operating at the enterprise), or performed for the benefit of a new

nomenclature of models on the basis of subjective reasons, i.e. direct testing in welding and practical evaluation of welding properties. Both methods are justified as a whole, however in the first case it results in refusal from introduction of new promising models, and in the second case it is defined by certain testing conditions, quality of materials being used, methods of samples preparation, qualification and acquired skills of a welder, that may lead finally to taking a wrong decision.

The objective information about the welding-technological properties (WTP) of equipment, and, consequently, its customization for certain production can be obtained by the test results. The only standardized document which regulates methods and procedures of such testing is State Standard GOST 25616–83 [1]. The mentioned document sets forth special requirements for quantity and quality of samples for welding

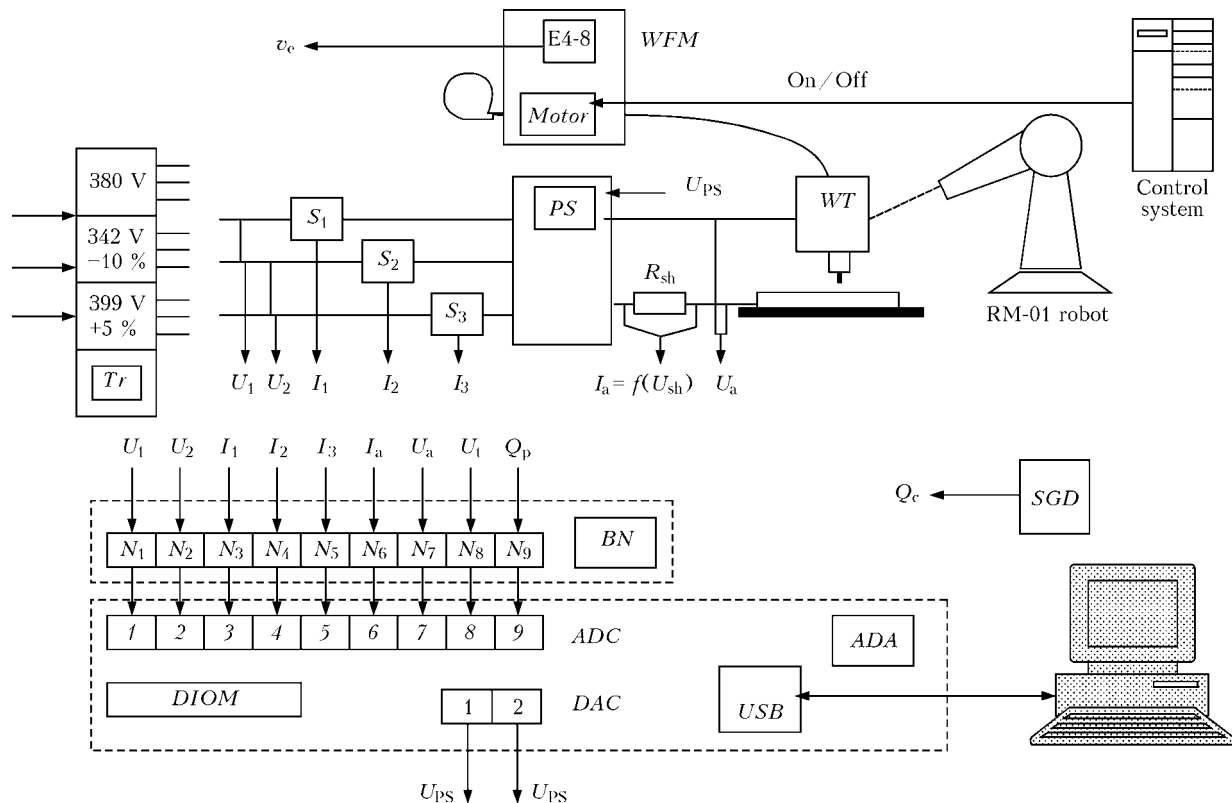


Figure 1. Schematic diagram of measuring and recording test complex: *WFM* — wire feed mechanism composed of feed motor (*Motor*); *E4-8* — encoder to control the wire feed speed; *SGD* — shielding gas device with sensor of gas consumption control; *Tr* — distribution transformer to imitate the decreased by 10 % (342 V) and increased by 5 % (399 V) voltage of mains (according to the requirements [1]); *WT* — welding torch; *RM-01* robot with the control system «Sfera 36» to move the torch along the trajectory of welding; *S₁–S₃* — *PS* current control sensors in three phases; *R_{sh}* — measuring shunt to control the current in welding circuit; *N₁–N₉* — channels normalizer; *BN* — block of normalization signals to bring their level to the values suitable to the input of the analog-digital converter (*ADC*); *ADA* — intermediate device designed to convert the controllable signals into the digital form and their transfer in real time through *USB* channel to a computer for storage, visualization and further processing (composed of *ADC*, digital-analog converter (*DAC*), discrete input-output module (*DIOM*) and *USB*); *1–9* — *ADC* inputs; *U_{PS}* — controllable voltage of *PS*; *U_{sh}* — voltage on the shunt; *U_t* — voltage of tachogenerator

and conditions of its performance at tests and also requires the presence of recording equipment to control parameters of primary and secondary circuits. However conclusions, obtained as a result of tests, bear rather qualitative character according to the quantity of evaluative points — «good», «satisfactory», «bad», while in using the modern recording system only a part of obtained information is used.

The use of specialized means of processing the experimental statistic information about the dynamics of controllable parameters allows obtaining of additional data about WTP of equipment and defining the methods of their improvement.

In our opinion, the *PS* tests by methods given in [1] do not give necessary information on the advantages or disadvantages of a certain model. Comparative tests of a new model with early applied models can be more effective. By processing the statistic data of comparative testing it is possible to obtain the numerical evaluations of WTP (short circuit frequency, average rate of current increment at short circuits, coefficient of slope of static volt-ampere characteristics, etc.) of new equipment and its analogue.

The quality of statistic information analysis and characteristics of properties of equipment, obtained on its basis, significantly depend on the applied re-

ording equipment. Nowadays a number of such systems has been developed [2, 3 and others] differing mainly by the quantity of channels of measurement and recording of information, quick-response, volume of obtained samplings, availability of hardware and software to process information and so on.

To conduct the comparative tests of welding equipment with keeping the requirements of standardized documents, the automated measuring-recording testing complex has been developed at the E.O. Paton Electric Welding Institute (Figure 1). The list of controllable signals is given in Table 1.

The control of the process of information recording is performed using a program, here the operator presets the quantity of channels being questioned simultaneously, frequency of reading, volume of sampling being recorded. The visual observation of variation of signals analyzed in the real time is possible. The robot included into the complex for movement of welding torch allows flexible change in welding direction from the lower to vertical and investigation of the elasticity of arc due to the smooth variation of distance from the torch to workpiece, here the high stability of welding speed is provided.

Let us take the results of comparative tests of inverter *PS* *VDUCh-500* and thyristor rectifier *VD 506*

Table 1. List of controllable signals

Signal description	Designation on the scheme	Place and method of measuring
Voltage: between the first and second phase of mains	U_1	Directly on the terminals of distribution transformer
between the second and third phase of mains	U_2	
Phase current:		Current transformer UTT-5M
first	I_1	
second	I_2	
third	I_3	
Arc current	I_a	Measuring shunt (75 mV, 750 A)
Arc voltage	U_a	Between the workpiece and current conductor to the torch
Electrode wire feed speed	v_e	Encoder E4-8
Shielding gas consumption	Q_c	Reducer-flow meter on the cylinder

DK as an example. The similar tests were conducted for PS VDUCh-350 and rectifier VS 300 B.

Figure 2 shows oscillograms of signal variation proportional to the arc current at the initial zone of welding. It is noticeable that the arc ignition from PS VDUCh-500 has a more stable character, whereas using rectifier VD 506 DK the arc breakdowns occur.

Figure 3 shows the results of recording the current and arc voltage of PS VDUCh-500. The similar data are presented for VD 506 DK, VDUCh-350 and VS 300 B. The Figure shows oscillogram area consisting of 1500 values of current and voltage obtained at reading rate of 1.25 kHz using one channel. The general volume of sampling is 30,000 values. At the analysis of spectral density of current signals and arc voltage in CO₂ welding it was established that 99 % of signal capacity is focused within the frequency range from 0 to 200 Hz. Thus, the selection of reading frequency

of 1.25 kHz predicts the meeting of requirements of Kotelnikov theorem.

In welding with periodical short circuits the important characteristic for evaluation of process stability is their frequency. The moment of a short circuit is characterized by an abrupt drop in arc voltage and jump in current. The frequency of short circuits for the established process is the constant value and little dependent on the type of PS.

According to the obtained experimental data the evaluation of average frequency of short circuits in

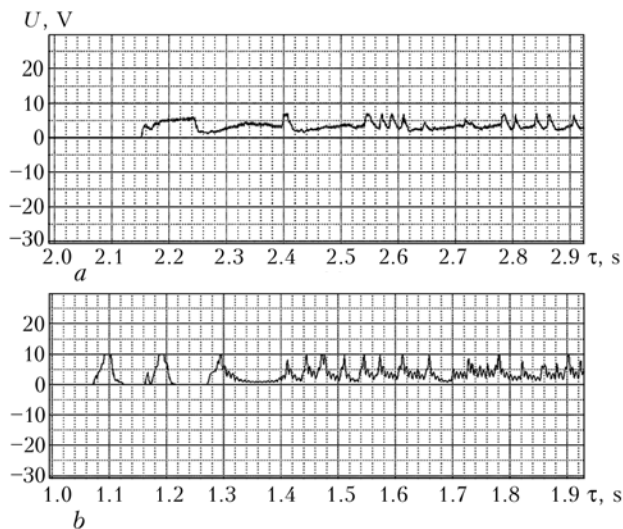


Figure 2. Oscillograms of signal variation proportionally to arc current at the initial welding zone obtained for PS VDUCh-500 (a) and VD 506 DK (b): U --- voltage on the normalizer output in the channel of current measurement; τ --- time

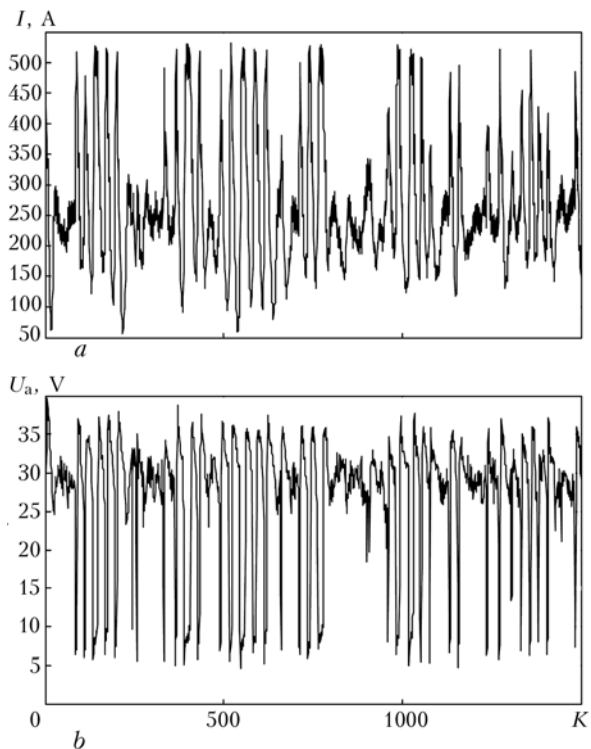


Figure 3. Oscillograms of current (a) and voltage of secondary circuit (b) of PS VDUCh-500 (welding condition (average values): $I = 250$ A; $U = 27$ V; $v_w = 25$ m/h); K --- quantity of measurements with periodicity of 800 μ s

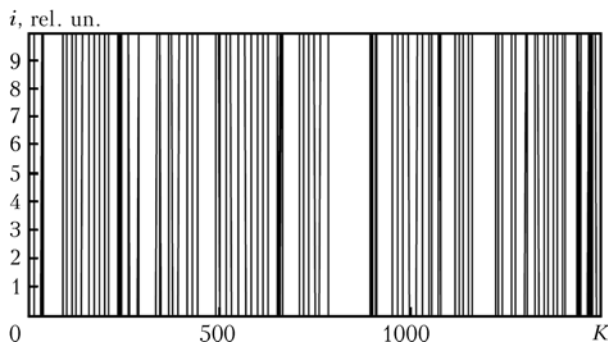


Figure 4. Type of pulsed function i

Table 2. Results of comparative tests of PS

PS type	Frequency of short circuits, Hz	Coefficient of slope of volt-ampere characteristic, V/A	Rate of current increment at short circuits, kA/s
VDUCh-500	48	0.006	68
VD 506 DK	45	0.035	81
VDUCh-350	40	0.008	75
VS 300 B	49	0.018	84

welding using investigated welding PS has been conducted. The algorithm is based on the designing of a pulsed function which is $i = 1$ and 0 at exceeding of preset threshold value of welding current, if the current value is less than the threshold value. The average value of a pulsed function $i = 1$ at equal time intervals is taken as the average frequency of short circuits. As an example, Figure 4 presents the type of a pulsed function plotted at signal processing for PS VDUCh-500. The total values, averaged from 1500 recorded values, are given in Table 2.

The determination of static external volt-ampere characteristics of PS was performed using ballast rheostat with five control steps. The PS voltage was controlled directly on the rheostat terminals. The current was fixed on shunt contacts of the measuring complex. Volt-ampere characteristics of PS VDUCh-500 are given in Figure 5. The coefficients of slope of static volt-ampere characteristics for both types of PS are given in Table 2.

The important characteristic of quality of PS from the point of view of a short-circuit welding process is the rate of current increment at the moment of a short circuiting. The evaluation of an average rate of current increment, made by periods of observation, is given in Table 2. Following the recommendations of [4], the best are the results of PS VDUCh-500, which is the evidence of comparatively small metal spattering (estimated visually).

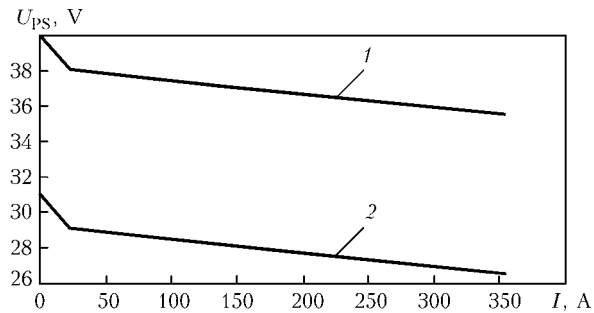


Figure 5. Volt-ampere characteristics of PS VDUCh-500 obtained at the open-circuit voltage 40 (1) and 31 (2) V

The results of comparative tests of welding PS VDUCh-500, VD 506 DK, VDUCh-350 and VS 300 B according to the examined parameters group are given in Table 2.

It should be noted that it is impossible at the present moment to refuse completely the subjective evaluation of all parameters of WTP of PS. For example, the quality of weld formation is evaluated visually by a welder-specialist and does not have distinct digital criteria. However, having a definite practical experience it is possible to predict how the given PS will form a weld performed at low, average and high values of current by knowing the numerical values of its parameters, i.e. the coefficient of slope of volt-ampere characteristic and rate of current increment at a short circuiting.

CONCLUSIONS

1. The results of comparative tests of welding equipment applying modern means of acquisition, recording and data processing represent complete information about advantages and disadvantages of PS models as compared to earlier applied ones, that allows consumer to take a grounded decision for updating the equipment park.
2. Using the means of processing the statistic information obtained during the tests it is possible to determine the additional parameters of WTP of equipment, for example, average frequency of short circuits, etc.
3. The results of comparative tests of PS VDUCh-500, VDUCh-350 and rectifiers VD 506 DK, VS 300 B allow making the conclusion about the advantages, such as arc ignition, rate of current increment at short circuits and negligible spattering of electrode metal, to provide the stable process.

1. GOST 25616-83: Power supplies for arc welding. Methods of testing of welding properties. Introd. 01.01.84.
2. Paton, B.E., Korotynsky, A.E., Skopyuk, M.I. et al. (2002) System of in-process quality control of welding equipment during its manufacturing. *The Paton Welding J.*, **5**, 25-27.
3. Kisilevsky, F.N., Butakov, G.A., Dzyabura, V.A. et al. (1990) Automated complex for study of methods and means of arc welding process control. *Avtomatich. Svarka*, **6**, 24-27.
4. Potapievsky, A.G. (2007) *Consumable electrode shielded-gas welding*. Pt 1. Kiev: Ekotekhnologiya.

LASER-SUBMERGED ARC HYBRID WELDING

U. REISGEN and S. OLSCHOK

Welding and Joining Institute, Aachen University, Aachen, Germany

This paper presents a novel method — laser-submerged arc hybrid welding — for the production of thick-walled parts, for example, structural tubes in pipeline construction or shipbuilding sections. The process-specific advantages and disadvantages are explained. It is further examined whether the welds which have been produced by this method will meet the requirements of the industry and which problems, if any, might occur.

Keywords: hybrid welding, laser beam, pulsed arc, structural steel, edge preparation, penetration, weld formation, energetic efficiency

The laser-arc hybrid welding method has been known for more than 20 years now. This process is characterised by the fact that the laser beam and the arc are, at the same time, acting in one (common) process zone. So far, two variations of laser-arc hybrid processes have been used for industrial application.

The laser-TIG hybrid welding method allows very high welding speeds in welding of aluminium sheets for tail-lifts with, at the same time, a very high surface quality of the weld. The laser-GMA hybrid welding method is, on the other hand, used for steel applications (shipbuilding) and also for aluminium structural designs (automotive engineering).

While working on the Welding and Joining Institute research project, the application of the laser-GMA hybrid process, however, met problems with regard to pores in the root if sheet more than 12 mm thick were applied — this is to be ascribed to the insufficient degasification possibility of deep and narrow laser welds [1].

For this reason, attempts to optimise the hybrid process have been made. Improved degasification pos-

sibilities are expected by substituting the GMAW process for the SAW process since after that the melt is maintained for a longer time.

In laser-GMA hybrid welding, the arc process causes the lowering of the molten pool surface where, through adaptation of the focus position, the weld penetration depth is increased [2, 3]. The penetration depth is mainly determined by the laser beam power and shaping, the weld width is mainly determined by the arc, in particular, by the arc voltage. In contrast to the «pure» laser beam process, a welding speed increase of up to 100 % at a constant laser beam power had, sporadically, been achieved [4, 5]. The energetic efficiency of the process is increased through the application of the arc power source which, in comparison with the laser, is working with a higher efficiency. In the capacity of a non-contact tool, the laser energy input into the workpiece is carried out in a focussed form, thus, the heat input is low. The advantages, for example, a small HAZ or high welding speeds for welds with high aspect ratio are to be mentioned at this point. There are, on the other hand, the disadvantageous high equipment costs and also the low degree of efficiency. The low gap bridging ability is also among the disadvantageous factors.

In laser-GMA hybrid welding, the addition of filler material is ensured via the arc process. The use of the GMAW technology entails the advantage that the filler wire is molten by using relatively inexpensive energy while the high-quality, expensive laser beam energy still causes, unabatedly, a high penetration depth. The positioning of the wire to the laser beam is relatively unproblematic since the guidance of the arc into the keyhole is observable through the common plasma (Figure 1).

The arc is pulsed via customary GMA welding power sources [6] or it is applied as a DC arc, in the most cases in the form of a spray arc. The shielding of the welding zone is, just as in CO₂-laser beam welding, realised with pure helium [2] or with helium-argon gas mixtures. The mainly used welding filler materials are similar and customary solid wires; the same wires as used for «pure» GMA welding of the base materials [7].

For thick-plate welding, mainly CO₂-laser beam sources are used since those provide higher powers than those of Nd:YAG-lasers [8].

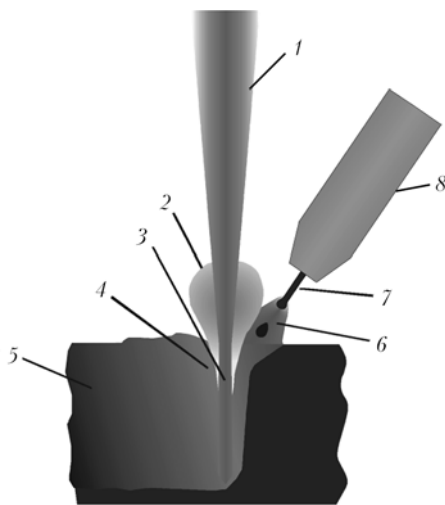


Figure 1. Schematic diagram of the laser-GMA hybrid welding method: 1 — laser beam; 2 — plasma; 3 — keyhole; 4 — molten pool; 5 — material being welded; 6 — GMAW torch; 7 — filler wire; 8 — GMAW nozzle

Apart from the square butt preparation, also V- and Y-groove shapes can be used which are, partially, a result of blanking without any further edge preparation. In contrast to laser beam welding with cold filler wire, the laser beam energy must not be used for melting the filler material since the wire has been fed to the process in an already molten form, thus a reduction of the welding speed can be dispensed with [9]. The filler material allows exerting a defined metallurgical influence on the welded structure [10, 11].

While in laser beam welding mainly parallel welds with a high aspect ratio are produced (Figure 2, *a*), the upper part of hybrid-welded seams is particularly expanded (Figure 2, *c*), which results in a triangular or «mushroom» or «bell-shaped» weld shape [9].

The set-up of the torch relative to the laser beam can be differing; the torch is sometimes positioned in the welding direction in front of the laser (trailing) [12, 13] or it follows the laser beam (leading) [14–17]. Welding with the torch directed away from the weld bead is mostly used for the hybrid welding of aluminium since this offers an arc attachment point without oxide layer (removed by the laser beam) — this again increases the process stability significantly [18].

LSAHW process. From an earlier research project of the Welding and Joining Institute, Aachen University, it is known that the laser-GMA hybrid welding method, particularly in welding sheets of thicknesses of more than 12 mm has a tendency to pore formation, albeit low [19]. Pores are, in most cases, accepted by the user industry, however, this is not consistent with customer fulfilment. A reason for the pore formation is the long degasification channel. A remedy might be a longer maintenance of the molten pool.

This was the reason for the reflection of maintaining the molten pool for a longer time by using the laser-submerged arc hybrid process (LSAHW) and thus to create more favourable degasification possibilities. Both processes are, at this, moved as close as possible (13–15 mm) into one process zone.

SAW is a high-quality, reliable and productive welding process which has been successfully applied for years in shipbuilding, terotechnology and pipe construction. The method belongs to the group of arc welding processes and it is characterised by the fact that the arc is burning invisibly and, shielded from the atmosphere, inside a gas- and metal-vapour filled welding cavity. This cavity is surrounded by liquid slag from the molten weld flux. Besides a high thermal efficiency degree with good molten pool degasification, the slag effects also the forming of a smooth bead and notch-free surface. In connection with a suitable wire-flux combination which has been adapted to the base material the result will be high-quality welding.

Of particular disadvantages, however, are the low penetration depth and the high molten volume quantity which makes it, in most cases, necessary to weld with backing.

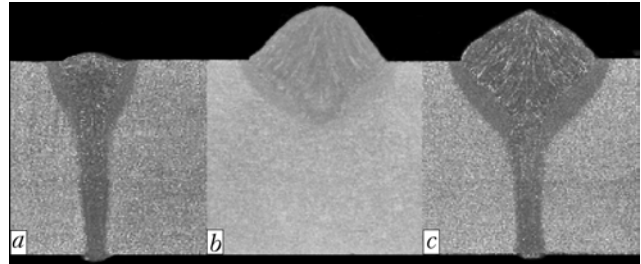


Figure 2. Welds: laser welding (*a*), GMAW (*b*), laser-arc hybrid welding (*c*)

According to the previous state-of-the-art, the variation «combination of laser-submerged arc» has, as a method coupling, not yet been a matter of research. The investigations which have been known so far are restricted to the consideration of the process combination SAW and laser beam welding [20, 21]. As far as previous investigations are concerned, the spatial distance of both processes and the separation of the weld into a laser-welded and a SA-welded area have been noticeable. Those areas have, among one another, not shown any mixing of the weld material. It has just been the preheating, brought in by the laser beam welding process which resulted in the synergy effect of increasing the welding speed of the SAW process.

The coupling of the processes, both the laser beam welding and the SAW process in one process zone proved to be a problem since the flux had been falling into the keyhole of the laser beam and the laser radiation had been absorbed by the flux and not by the component. For that reason, a device which impeded this «falling forward» of the flux had to be designed and built. One starting point is the separating plate (patented by RWTH, Aachen University) which is mounted between laser beam and flux feeder (Figure 3) [22]. The shielding gas which is required for laser beam welding is directed against the welding direction onto the separation plate in order to blow the flux which might fall through the gap between workpiece and sheet out of the laser beam process zone.

This arrangement, however, requires some process-related parameters which have, so far, not been considered in the hybrid technique. The distance between separation plate and workpiece is of particular importance. The distance must be chosen short enough to ensure that smallest possible quantities of flux are falling forward and must be chosen large enough that a slag that might be running ahead does not jam to the sheet. The inclination angle of the sheet is also most important. If the inclination angle is too large, the sheet might be captured by the laser beam, if it is too small, the arc might burn between sheet and filler wire. The shielding gas flow, moreover, must not be too voluminous since then the arc of the SAW process might be blown off which would result in pore formation in the weld. Figure 4 shows the effects of this hybrid process.

As distinguished from laser-GMA hybrid welding, the sheet surface is not reduced by the arc process and

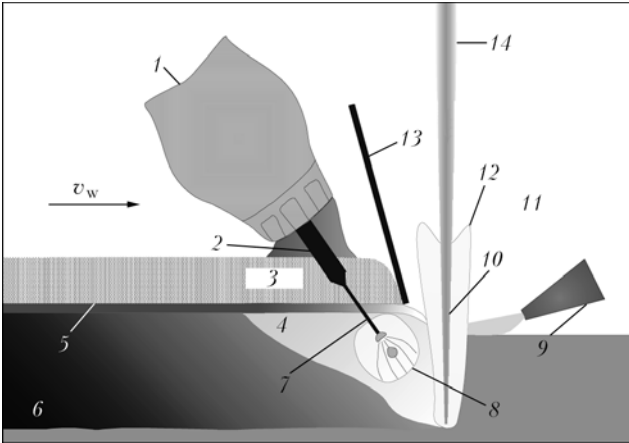


Figure 3. Schematic set-up of LSAHW method: 1 — flux hopper; 2 — contact tube; 3 — flux; 4 — molten pool; 5 — solid slag; 6 — weld metal; 7 — SAW consumable wire electrode; 8 — weld cavity with arc; 9 — helium jet; 10 — keyhole; 11 — liquid slag; 12 — metal vapour plasma; 13 — separating plate; 14 — laser beam

thus no larger penetration depth is achieved. A look at the comparison of the hardness measurements (*HV1*) (Figure 5) shows, however, that a reduction of the hardness peaks in the laser dominated root area occurs. It had also been possible to reduce the hardness in the centre area of the weld.

The microsections show clearly that the heat input into the workpiece using the LSAHW process is higher (Figure 6). In the detailed photograph, streaks of pearlite in the HAZ which are longer than those in the laser weld are very clearly discernible. The structure of the metal in the weld is, in the laser part of the hybrid weld, more fine-grained. This effect is wanted and represents one of the aims of the LSAHW advancement. A higher ductility, compared with the «pure» laser weld, is the result thereof.

The upper LSAH-welded bead is similar to that of a SA-welded; it is characterised by a flat transfer to the sheet without any undercuts, it is possible to influence the weld reinforcement via the suitable selection of the wire feed and the applied voltage. The appearance of the root is different than that of a «pure» laser beam weld: the slag-forming elements from the SAW process are responsible for the narrow, flake-free and also shiny lower bead.

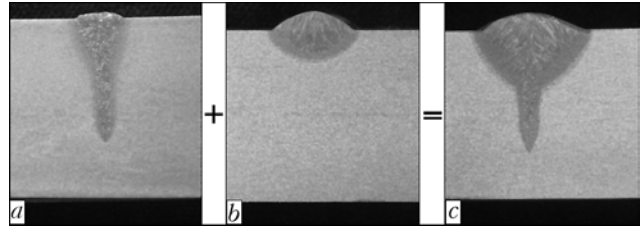


Figure 4. Welds: laser welding (a), SAW (b), LSAHW (c)

Test conditions. For the basic tests with the LSAHW method the following devices were used: a fast axial flow laser (Trumpf Lasertechnik) with unstable resonator TLF 20.000; a fully electronic, secondary-switched, user-programmable and computer-controlled MIG/MAG-precision power source for fully automatic pulsed-arc welding (type Hybrid 6000 MR, AMT); a laser hybrid welding head which had been specially designed by the Welding and Joining Institute. Figure 7 shows the set-up of the equipment in the process area.

The following test materials were used: shipbuilding steels with plate thicknesses of 8.0 and 20.3 mm (AH 36), a structural steel with the plate thickness of 14 mm (S355 J2G3), and also a high-strength thermomechanically rolled fine-grained structural steel with the plate thickness of 38 mm (X65).

Moreover, filler materials, namely SA wire S2Si with a diameter of 1.6 mm and the fluoride-basic SA flux OP 122, were used.

The tests were carried out in the gravity position PC, sometimes backing was used.

Results. For a joining task from the field of shipbuilding, AH 36 steel sheets 8 mm thick and with plasma-cut edges were welded. The aim was to demonstrate that gap bridging is possible in the light-gauge sheet range, therefore, clearances 0–0.4 mm have been set. The welding speeds were 1.6 (zero-width of gap), 1.4 (gap of 0.2 mm) and 1.2 m/min (gap of 0.4 mm) (Figure 8). The molten metal had the tendency to collapse, particularly if the largest gap had been set; if the voltage of the SAW process was reduced, sufficient penetration had not been achieved. With those thin sheet thicknesses, gaps seem to be most critical and difficult to weld. A remedy might be the use of a thinner wire which allows a

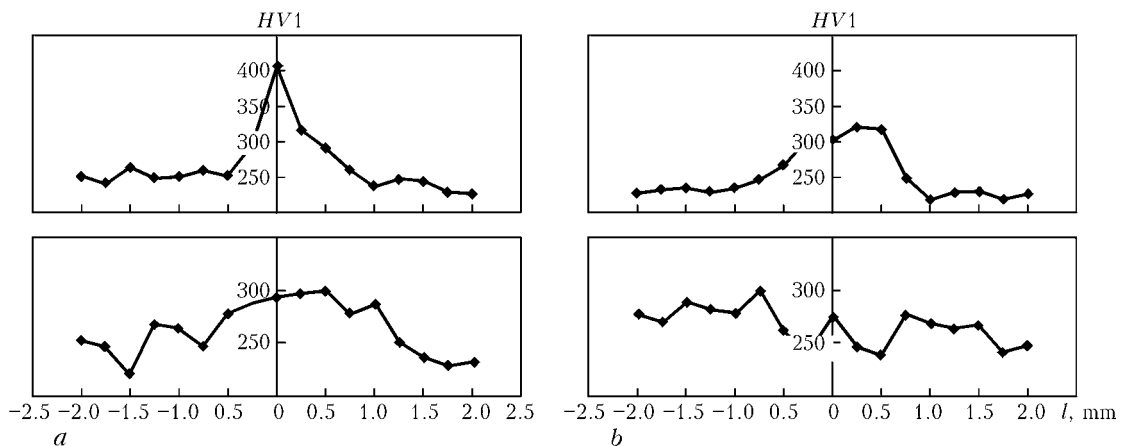


Figure 5. Hardness *HV1* of laser- (a), LSAH-welded (b) joints

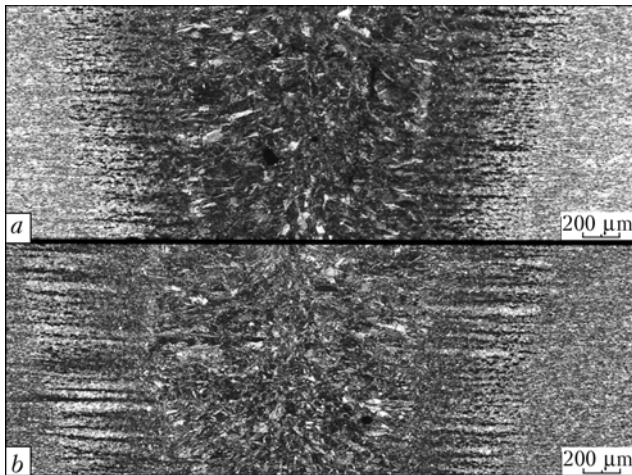


Figure 6. Micro-sections of weld centre: laser welding (a); LSAHW (b)

better dosage of voltage during the welding. LSAHW, however, is in principle, well qualified for this joining task, if clamping has been carried out appropriately, i.e. without gaps.

Type of Y-groove preparation with 16° and 5 mm root face stems from the application field of pipe construction. The edge preparation had, process-induced, not been optimal; the edges were flame-cut and then coarsely ground. Inaccuracies in weld preparation were a result thereof, the root face was, for the most part, lower than 5 mm.

Figure 9 shows the macro-sections of this weld. The welds (Figure 9, a, b) have been welded in the first pass at $v_w = 0.8$ m/min, $P_L = 12$ kW; the back weld pass had been carried out using the «pure» SAW process. This type of double-sided single pass welding had been tested by means of the transverse tensile test and the notch bending test at -20 °C. The tensile test results were normal, all specimens ruptured in the uninfluenced base material besides the weld. In the notch bending test (notch orientation in the weld centre), the values varied between 78 and 152 J, the fracture surfaces indicate the transition zone of the A_V/T curve.

The suitability of the method is, thus, demonstrated also for this case. The weld has fulfilled the requirements of the mechanical-technological properties.

In order to find out the limits of the method, the penetration depth was increased further. It is known from the field of «pure» laser beam welding that, as of a penetration depth of 15 mm the molten metal has the tendency to collapse, which is the reason why, as from this plate thickness onwards, most work is carried

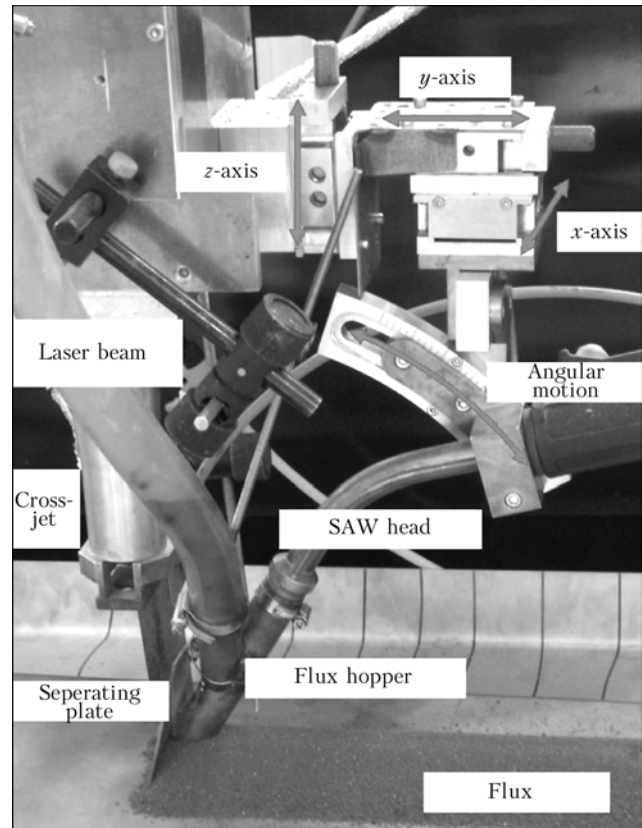


Figure 7. Equipment set-up in the process area

out in the transverse/bank position PC. For those tests, however, flux backing had been used in order to counteract this phenomenon.

Figure 10 shows the plasmacut macro-section of V-weld on steel 20.3 mm thick with zero-width of gap performed with backing. The used laser power was 20 kW, the welding speed was 0.8 m/min. This gives proof that, single-sidedly, it is possible to weld up to a sheet thickness of approximately 20 mm.

For economically proficient welding of thick-walled parts, i.e. welding with as few passes as possible, the consideration of welding a root face which is as large as possible in the double-sided single pass welding technique emerged. First tests of double Y-weld performed on steel 38 mm thick using double-sided single-pass welding, are shown in Figure 11. The X-ray examination confirmed that the metal was free of pores. A high overlapping is noticeable. The method is, in principle, not yet exhausted at this point, further tests with higher root faces are scheduled.

Summary and perspectives. The applicability of the LSAHW method for bead-on-plate welds and joint

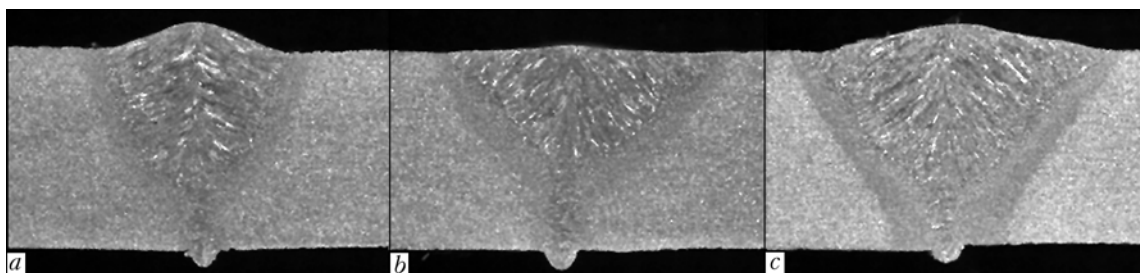


Figure 8. Macro-section of a plasmacut V-weld performed on steel 8 mm thick with width of gap of 0 (a), 0.2 (b) and 0.4 (c) mm

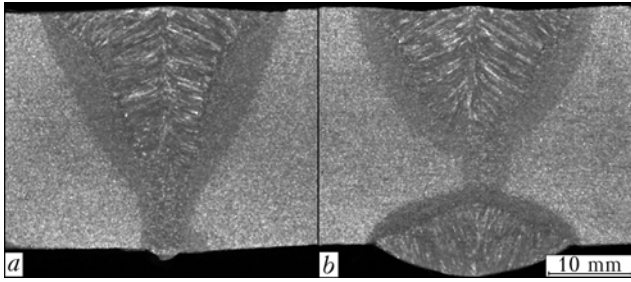


Figure 9. Macro-section of Y-weld with a root face of 16° and 5 mm performed on steel 14 mm thick with zero-width of gap

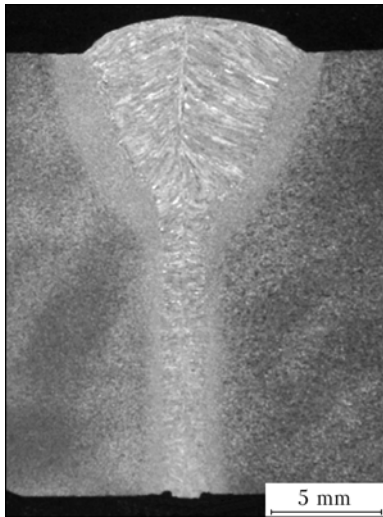


Figure 10. Macro-section of V-weld performed on steel 20.3 mm thick with zero-width of gap

welding with different weld preparation on plates with thicknesses of 8–38 mm had been tested within the scope of this work.

Further improvement of this process and a broader field of application are to be expected from the use of efficient solid-state lasers. Particularly advantageous is the reduced risk of plasma shielding. It is easier to couple the shorter wave length of the solid-state laser into the material to be processed. The flexibility of the equipment would also improve with a shorter wave length since the complicated beam guidance via mirror optics can be dispensed with and the laser beam can be guided via light wave cables into the processing optics. Constant further developments in the field of laser welding methods allow even more ideas for the advancement of the method. For achieving better degasification and a weld which has a pore quantity which is as low as possible or a pore-free weld, the solution may lie in the expansion or stabilisation of the vapour capillary. One possibility for this would be welding and testing with adapted oscillating optics.

The addition of shielding gas and/or process gas is another process parameter which has to be tested for further work in this field. If efficient solid-state lasers, e.g. fibre lasers, can be used the shielding gas could be dispensed with and a compressed air jet could be used for cleaning the laser process zone. Process costs would be reduced this way and the method would become even more economically proficient.

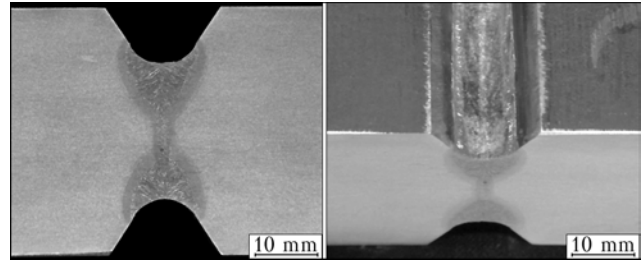


Figure 11. Macro-section of double Y-weld with a root face of 70° and 10 mm performed on steel 38 mm thick with zero-width of gap

So, it is established that LSAHW is a further most interesting variation of laser-arc hybrid welding. The industry shows interest in LSAHW and a possible practical application. This will be further increased through the use of less expensive, more robust and more flexible laser power sources.

Last but not least, the ISF — Welding and Joining Institute wishes to express thanks to the companies whose commitment allowed us our research work. First and foremost we would like to mention the ESAB GmbH and AMT Maschinen- und Geratetechnik.

1. Dilthey, U., Olschok, S. (2004) Untersuchungen zur Nutzung der Synergieeffekte beim Hochleistungs-Laser Hybridschweißen von dickwandigen Rohrkörpern aus C-Mn-Stählen. In: *Abschlussbericht des AiF-Forschungsvorhabens 13.407N*. Aachen, 2004.
2. Abe, N., Hayashi, M. (2002) Trends in laser arc combination welding methods. *Welding Int.*, 16(2), 94–98.
3. Walz, C., Stiebe-Springer, I., El Rayes, M. et al. (2001) Hybrid welding of steel for offshore applications. In: *Proc. of 11th Int. Offshore and Polar Engineering Conf. and Exhibition (2001)*, 263–266.
4. Dilthey, U., Lueder, F., Wieschemann, A. (1996) Laserstrahlschweißen in der Fertigung — Einsatz und Entwicklung. *Baender Bleche Rohre*, 37(11), 26–39.
5. Wieschemann, A. (2001) *Entwicklung des Hybrid- und Hydraschweißverfahrens am Beispiel des Schiffbaus*: Dissert. RWTH Aachen.
6. Dilthey, U., Dobner, M., Ghandehari, A. et al. (1996) Entwicklung. In: *Stand und Perspektiven der Strahltechnik: 4. Konferenz Strahltechnik* (Halle), 1–13.
7. Maier, Ch., Reinhold, P., Maly, H. et al. (1996) Aluminium-Strangpressprofile im Schienenfahrzeugbau, geschweisst mit dem Hybridverfahren Nd:YAG-Laser/MIG. In: *DVS-Berichte*, Band 176. Duesseldorf: DVS, 198–202.
8. Keller, A. (2001) *CO₂-Laserstrahl-MSG Hybridschweißen von Baustählen im Blechdickenbereich von 12 bis 25 mm*: Dissert. RWTH Aachen.
9. Behler, K., Maier, Ch., Wieschemann, A. (1997) Kombiniertes Laser-Lichtbogenschweißen — Erweiterungspotential für die Lichtbogentechnik. In: *Aachener Schweisstechnik Kolloquium*. Aachen: Shaker, 151–172.
10. Dilthey, U., Lueder, F. (1997) Untersuchungen zum Laserstrahlschweißen hochkohlenstoffhaltiger Stähle unter Einsatz von Zusatzwerkstoff. In: *Abschlussbericht des DFG-Forschungsvorhabens Di 434/18-4*.
11. Dilthey, U., Biesenbach, M. (2000) Untersuchung der Randbedingungen für die Bildung von «acicular ferrite» in Schweißgütern bei schneller Abkühlung. In: *Abschlussbericht des AiF-Forschungsvorhabens 11.377 N*.
12. Kutsuna, M., Chen, L. (2001) Research on laser-MAG hybrid welding of carbon steel. In: *Proc. of 7th Int. Welding Symp. of JWS* (Kobe, Japan), 403–408.
13. Abe, N., Hayashi, M. (2002) Trends in laser arc combination welding methods. *Welding Int.* 16(2), 94–98.
14. Yoneda, M., Katsumura, M. (1989) Laser hybrid processing. *J. JWS*, 58(6), 427–434.
15. Hamasaki, M. *Welding method taking laser with MIG*. Pat. 59-66991 Japan. Publ. 1984.
16. Hamasaki, M. *Welding method combining laser welding and MIG welding*. Patent US 4,507,540. Publ. 1985.
17. Makino, Y., Shiihara, K., Asai, S. (2002) Combination welding between CO₂-laser beam and MIG arc. *Welding Int.*, 16(2), 99–103.



18. Maier, Ch. (1999) *Laserstrahl-Lichtbogen Hybridschweißen von Aluminiumwerkstoffen*: Dissert. RWTH Aachen.
19. Dilthey, U., Woeste, K., Olschok, S. (2005) Modern beam-welding technologies in advanced pipe manufacturing. In: *Konferenz-Einzelbericht: EuroSteel*.
20. Coiffier, J.C., Jansen, J.P., Peru, G. et al. (1997) Combination of laser beam and submerged arc processes for the longitudinal welding of large welded pipes. In: *Proc. of Int. Symp. on High Strength Steels* (Trondheim, Norway, 1997).
21. Krivstun, I., Seyffarth, P. (2002) *Laser arc processes and their applications in welding and material treatment*. London: Taylor & Francis.
22. *Verfahren und Vorrichtung zum Schweißen von Werkstücken*. Deutsche Pat. 20 2005 024 457.2. Publ. 2005.

EFFECT OF THE CENTRIFUGAL THERMAL SPRAYING PROCESS ON PROPERTIES OF SPHERICAL TUNGSTEN CARBIDE PARTICLES

V.I. DZYKOVICH

E.O. Paton Electric Welding Institute, NASU, Kiev, Ukraine

Effect of the centrifugal thermal spraying process on structure, microhardness and stoichiometric composition of spherical tungsten carbide granules was investigated. Comparative analysis of initial spraying materials (ingots) and spherical particles was conducted. It is established that the granulated WC-W₂C particles, having the highest microhardness and wear resistance, can be produced only as a result of remelting of a spraying material.

Keywords: tungsten carbides, centrifugal spraying, stoichiometric composition, spherical particles, wear-resistant composite coatings, diffractometry

Fused tungsten carbide in spherical granules has received wide acceptance in the last years. It is advantageous over crushed tungsten carbide in increased hardness (up to *HV* 3000), high strength and flowability. These features made it possible to substantially widen the fields of application of this material. In particular, this concerns plasma-powder and laser cladding, as well as production of wear-resistant composite coatings by the impregnation method.

The most important characteristics of spherical particles of cast tungsten carbides (WC-W₂C) are their microhardness and microstructure. When each particle has stoichiometric composition, which is a eutectic alloy consisting of 78–82 % W₂C and 18–22 % WC (at 3.9–4.1 % C) [1], microhardness amounts to maximal values. Maintaining of the above proportion is a necessary condition for production of the material for composite coatings characterised by the highest wear resistance.

It is a known fact that one of the most efficient methods for production of spherical tungsten carbide particles is centrifugal thermal spraying of ingots, which are cast cylindrical rods with a diameter of 29–30 mm and length of 200–250 mm. The ingots can be made by melting in resistance or induction furnaces. The spraying process is carried out at a high ingot rotation speed (4,000–10,000 rpm). A heat source in this case is energy of the arc plasma jet [2, 3].

The purpose of this study was to investigate the effect on variations in structure and properties of the initial materials (ingots) by such factors as concentrated heating and instantaneous solidification of microvolumes of liquid melts (droplets) formed during the spraying process.

Experiments were conducted on samples of the initial materials (cast ingots) produced by melting in resistance furnaces and by the induction method, as well as on the spherical particles produced by centrifugal thermal spraying of these ingots. In parallel, the carbon content of the ingots and particles was determined by the chemical method. In addition, the tungsten carbide ingots and spherical particles were tested to determine microhardness, and were examined to reveal their microstructure. The spraying process was carried out under the conditions providing the spherical particle size composition within a range of 180–200 μm [4]. A test batch was composed of 10 ingots (15–17 kg), which made it possible to average

Table 1. Results of testing the samples of cast ingots and spherical particles

Sample No.	Carbon content, %	Microhardness <i>HV</i> 100
Cast ingots		
15/03-st.I	4.20	2317 ± 78
14/03-st.P	4.06	2206 ± 424
6/03-st.I	4.20	2394 ± 502
Spherical particles		
15/03-sf-1	3.98	2933 ± 366
15/03-sf-2	3.98	2904 ± 303
14/03-sf-1	3.80	2821 ± 312
14/03-sf-2	3.70	2801 ± 303
6/03-sf-1	3.70	2930 ± 300
6/03-sf-2	3.80	2914 ± 254

Note. In designation of samples taken from the ingots, letter «I» stands for induction melting method, and letter «P» stands for resistance furnace.

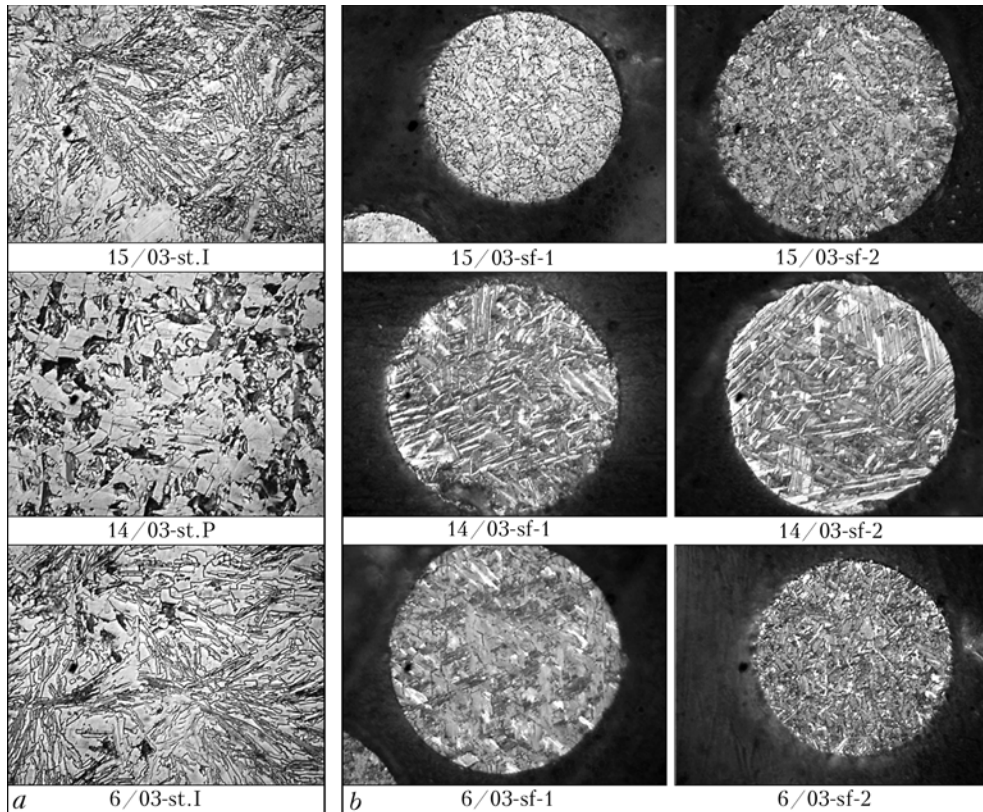


Figure 1. Microstructures ($\times 1000$) of cast ingots (a) and spherical particles (b)

the experimental results. Two samples of the spherical particles, 100 g each, were taken for investigations from each sprayed batch. In addition, 100 g samples

produced by mechanical crushing were taken from each batch of the ingots to test the initial materials.

Results of chemical analysis to determine the carbon content and results of microhardness tests are given in Table 1. Microstructure of the test samples is shown in Figure 1.

It can be seen from Table 1 that the carbon content decreases to some extent after remelting. However, the level of microhardness of the spherical particles is higher compared with the initial material, this allowing prediction of high performance of the wear-resistant coatings produced from the spherical particles (WC-W₂C).

Microstructures of the initial materials (cast ingots) (Figure 1, a) differ but insignificantly. Therefore, it can be concluded that methods used to melt the ingots have no effect on formation of phase components of the spherical particles in centrifugal thermal spraying.

The spherical particles (Figure 1, b) have a finer microstructure. Mechanical mixture of two phases is of a more ordered character. That is, it is remelting that is responsible for refining of structural components, which is attributable to formation of a great number of microvolumes of liquid metal (droplets), their instantaneous detachment and instantaneous solidification in flight. And it is these factors that explain increase in microhardness of the spherical WC-W₂C particles.

The most interesting results were obtained from comparative X-ray diffraction analysis of the ingots and granules produced by the centrifugal thermal spraying method. Results of evaluation of samples

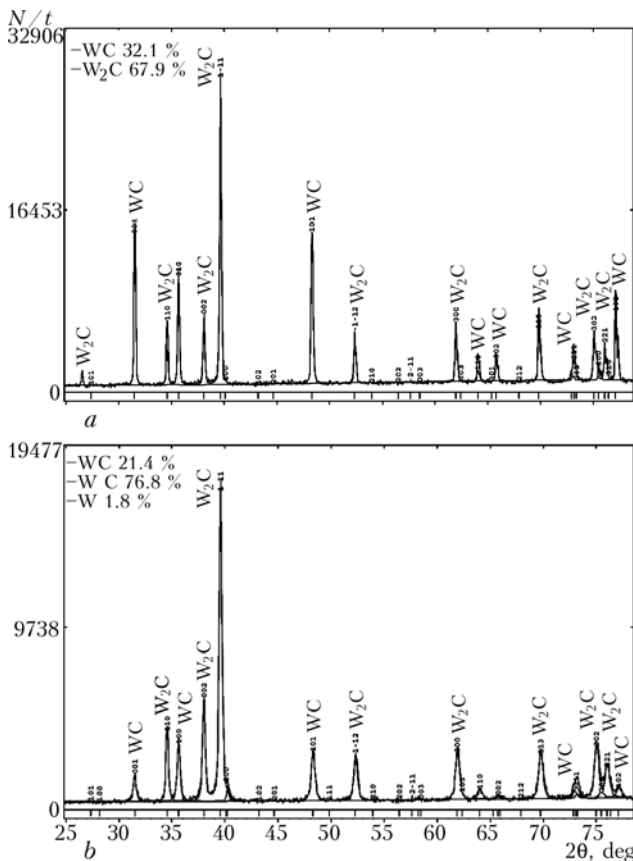


Figure 2. Fragment of full-profile analysis of diffraction pattern of samples 6/03-st.I (a) and 6/03-sf-1 (b)



6/03-st.I and 6/03-sf-1 are presented as the most demonstrative ones.

Diffraction of the samples was carried out by using the DRON-UM-1 diffractometer in monochromatic $\text{CuK}\alpha$ -radiation by the method of step scanning (35 kV, 35 mA; exposure time at a spot --- 3--7 s, step --- 0.05°). Graphite single crystal placed on the diffracted beam was used as a monochromator. A sample during filming was rotated about a normal to the coating plane. The data of diffraction experiment with calculation of the coefficient of texture of the phases were processed by using the PowderCell 2.4 software for full-profile analysis of X-ray spectra of a mixture of polycrystalline phase components [5]. The texture was described by using the March-Dollase model, and profiles of the diffraction maxima were approximated by the pseudo-Voigt function.

As found from evaluation of material of the initial cast ingots, proportion of the WC and W_2C phases is as follows, wt.%: 32.1 WC and 67.9 W_2C (Figure 2, *a*). This can be explained by the fact that despite the technological stability of the process of melting of cast ingots, the circumstances may occur, at which it can be extremely difficult to strictly control the time of holding of the liquid melt in a crucible and its subsequent discharging into a gate (because of dusting of a heating element, impossibility of visually monitoring the process of melting of the charge mixture, etc.). This leads to the risk of violation of the stoichiometric proportion between the considered phases.

As revealed by diffraction of samples of the spherical particles, the WC to W_2C ratio tends to the maximum possible eutectic one, and equals 21.4 WC and 76.8 W_2C (wt.%) (Figure 2, *b*). These data confirm the assumption that the process of centrifugal thermal spraying creates the ideal conditions (instantaneous detachment of a small volume of the liquid phase (droplet) and its instantaneous solidification)

Table 2. Results of calculation of lattice parameters

Sample No.	Phase state	Content of phase, wt. %	Lattice parameters, nm		Lattice orientation
			<i>a</i>	<i>c</i>	
6/03-st.I	WC	32.07	0.29058	0.28373	0.6598
	W_2C	67.93	0.51850	0.47345	--
6/03-sf-1	WC	21.43	0.29078	0.28383	--
	W_2C	76.82	0.51909	0.47311	--
	W	1.76	0.31667	--	--

for refinement of the structure and providing of the eutectic proportion equal to $\text{WC}/\text{W}_2\text{C} = 20/80$. The content of free tungsten is 1.8, wt.%. It is likely to be related to precipitation of an insignificant amount of tungsten on the particle surfaces, according to the theory considered in [6].

Therefore, quality of the tungsten carbide ingots, which are the raw materials for production of the spherical particles, hardly depends upon the method used to produce them. Manufacture of the spherical tungsten carbide particles with a refined and ordered structure, increased microhardness and near-eutectic $\text{WC}/\text{W}_2\text{C}$ ratio equal to 20/80 is possible only under conditions of remelting of cast tungsten carbides.

1. Samsonov, G.V., Vitryanyuk, V.N., Chaplygin, F.I. (1974) *Tungsten carbides*. Kiev: Naukova Dumka.
2. Bely, A.I., Danilchenko, B.V., Goncharenko, V.S. et al. *Machine for centrifugal spraying of refractory material rods*. USSR author's cert. 1381840. Publ. 15.10.1987.
3. Yushchenko, K.A., Zhudra, O.P., Bily, O.I. et al. *Method for manufacturing of granulated refractory materials*. Pat. 20516A Ukraine. Publ. 15.07.1997.
4. Samsonov, G.V., Upadkhaj, T.Sh., Neshpor, V.S. (1974) *Physical materials science of carbides*. Kiev: Naukova Dumka.
5. ftp:ftp.bam.de/Powder_Cell/pcw23.exe
6. Makhnenko, V.I., Zhudra, A.P., Velikoivanenko, E.A. et al. (2004) Mathematical modelling of the process of manufacture of spherical fused tungsten carbide granules. *The Paton Welding J.*, 2, 2--8.



APPLICATION OF PROTECTIVE EXTENSION IN THERMAL SPRAYING OF QUASI-CRYSTALLINE COATINGS

A.P. MURASHOV, I.A. DEMIANOV, A.P. GRISHCHENKO, A.N. BURLACHENKO and N.V. VIGILYANSKAYA
E.O. Paton Electric Welding Institute, NASU, Kiev, Ukraine

The efficiency of application of an extension in plasma spraying of coatings from quasi-crystalline alloy Al–Cu–Fe was studied. It was established that the extension allows increasing the amount of the icosahedral phase in a coating by improving the heating conditions and lowering the degree of oxidation of a spraying material.

Keywords: *thermal spraying, extension, coating, quasi-crystalline alloy, icosahedral phase*

One of the methods to control the plasma-arc spraying process is to apply special protective extensions, with the help of which it is possible to solve the following problems:

- partial cleaning of coatings from contaminations caused by non-controllable reactions of a spraying material and deposited layer with active components of the environment;
- protection from overheating, oxidation and dusting of the substrate surface outside the spraying zone or effective spraying spot;

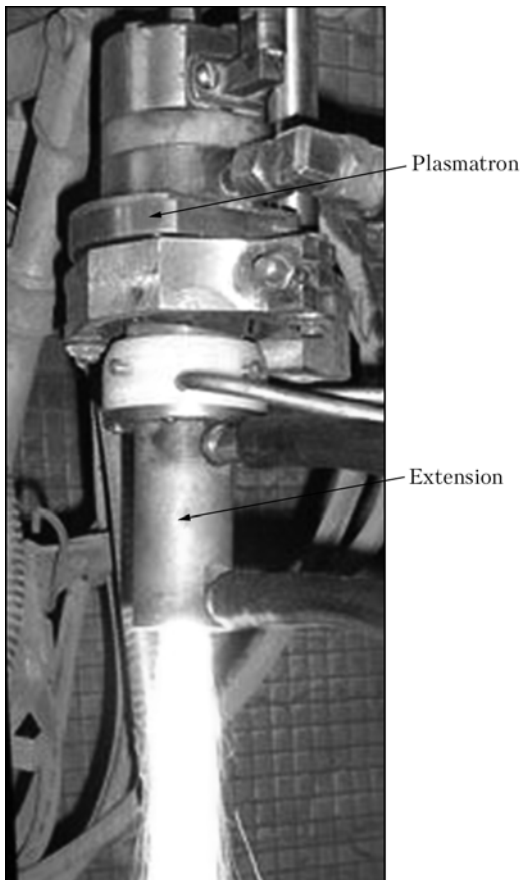


Figure 1. Plasma-arc spraying system comprising an extension

- variation of the coefficient of concentration of the gas-powder jet, size of its high-temperature region, composition and pressure of the environment within the spraying zone [1].

In this study the protective extension was used for plasma-arc spraying of Al₆₃Cu₂₅Fe₁₂ alloy coatings with a quasi-crystalline structure to increase the length of heating of a powder and decrease the degree of oxidation of the spraying material [2]. One of the conditions for providing coatings with a high content of the quasi-crystalline component is a maximum possible preservation of the initial composition, particularly of aluminium as an element having a high affinity for oxygen [3]. The purpose of the study was to preserve to the maximum possible degree the composition of the initial powder in spraying of a coating through extra constriction of the plasma jet by a concurrent gas flow, which limits admixing of air oxygen to the jet, possible reduction of the required power of the plasma jet to provide heating of the spraying material without overheating of surfaces of the powder particles.

The extension (Figure 1) consists of ceramic and copper water-cooled parts. The transportation gas together with the spraying powder is fed into the ceramic sleeve via two connection pipes located opposite to each other. In addition, the concurrent shielding gas (argon or nitrogen) is fed via channels made on the perimeter of the ceramic sleeve from the top, at the boundary with the nozzle. Application of the ceramic insulating sleeve makes it possible to electrically separate the extension from the nozzle, and use it without changing the spraying parameters set for the process without the extension. Feeding of the concurrent shielding gas allows protecting the powder during spraying from oxidation by air oxygen, which is usually drawn into the extension because of a difference in pressure inside the extension and environment. Feeding the powder via the two connection pipes make it possible to raise the spraying productivity owing to the possibility of increasing 1.5–2 times the transportation gas flow rate, this decreasing the risk of powder clogging, especially in the case of powders with low flowability.

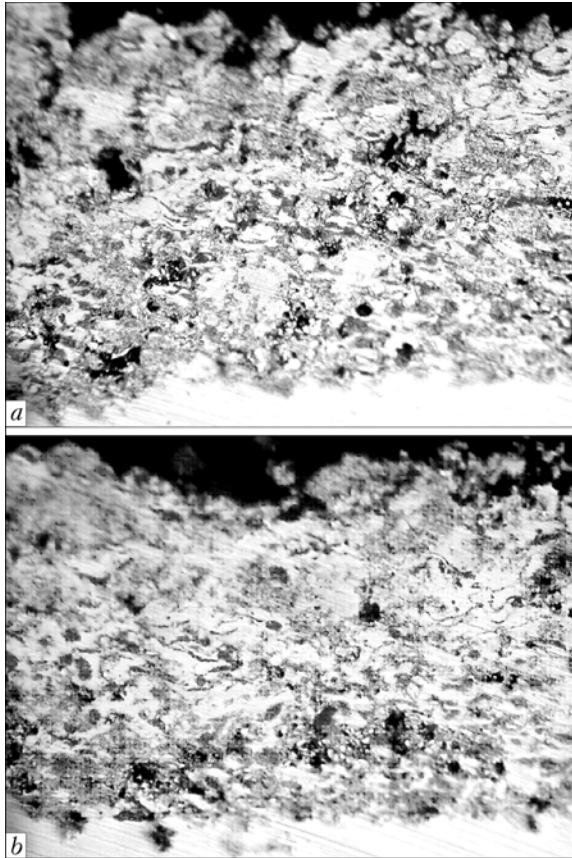


Figure 2. Microstructure ($\times 200$) of $\text{Al}_{63}\text{Cu}_{25}\text{Fe}_{12}$ powder coatings sprayed by the plasma-arc method with (a) and without (b) extension

The total height of the extension is 82 mm, this making it possible to use it to produce coatings from the majority of powders at spraying distance of 90–140 mm or more.

The powder of quasi-crystalline alloy $\text{Al}_{63}\text{Cu}_{25}\text{Fe}_{12}$ was produced by water atomisation. It consists of particles of an irregular, rounded and elongated shape with the developed surface. The powder fraction is from -63 to $+40$ μm . Flowability of the powder is 35 s/50 g, and its apparent density is 2.15 ± 0.01 g/cm^3 . According to the results of X-ray diffraction analysis, its content of the quasi-crystalline icosahedral phase is about 80 wt.%.

Parameters of spraying of $\text{Al}_{63}\text{Cu}_{25}\text{Fe}_{12}$ powder by the plasma-arc method

Parameter	Spraying without extension	Spraying with extension
Spraying current, A	500	350–400
Plasmatron voltage, V	30	30
Plasma gas (argon) flow rate, l/min	26	26
Transportation gas (nitrogen) flow rate, l/min	3.7	4.5
Concurrent gas (argon) flow rate, l/min	--	4.75
Powder consumption, g/min	30	45
Spraying distance, mm	110	110

The Table gives values of the selected spraying parameters.

Figure 2 shows microstructure of the coatings deposited by the plasma-arc method using the $\text{Al}_{63}\text{Cu}_{25}\text{Fe}_{12}$ powder with and without the extension.

The results of X-ray diffraction analysis of the coatings showed that the content of the quasi-crystalline phase in the coatings deposited by using the extension increased by 12 %, compared with the coatings deposited without the extension (62 and 50 %, respectively). The coatings in both cases are dense, contain a small quantity of pores, have a lamellar structure, and exhibit no separation from the substrate.

Therefore, application of the protective extension under conditions of plasma-arc spraying of coatings with quasi-crystalline structure makes it possible to produce coatings with an increased content of the quasi-crystalline phase.

1. Kudinov, V.V., Kosolapov, A.N., Pekshev, P.Yu. (1987) Extensions for local protection in plasma spraying. *Izvestiya SO AN SSSR, Series Tekhn. Nauk*, **21**, Issue 6.
2. Borisov, Yu.S., Korzhik, V.N., Chernyshev, A.V. et al. (1991) Optimisation of parameters and conditions of application of gas-dynamic extensions in thermal spraying. *Avtomatich. Svarka*, **8**, 67–70.
3. Sordelet, O., Besser, M. (1996) Particle size effects on chemistry and structure of Al–Cu–Fe quasicrystalline plasma sprayed coatings. In: *Proc. of 9th National Thermal Spray Conf.* (Cincinnati, Ohio, 7–11 Oct. 1996), 419–428.



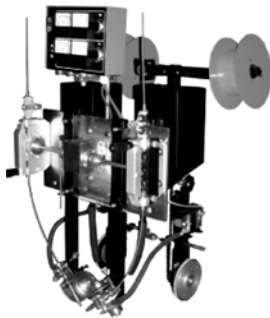
NEWS

TWO-HEAD AUTOMATIC ARC WELDING DEVICE ADF-1002

OJSC «Electric Machine Building Plant SELMA» mastered production of the 2TS-17S type automatic welding device ADF-1002 designed for automatic submerged arc welding of T-joints from carbon and alloyed steels using two inclined electrodes. The automatic device provides welding of stiffeners of the strip type or of the trapezium-shaped profile 160 to 360 mm high to orthotropic plates. The lower limit (160 mm) can be reduced at a special request.

The automatic device moves over a workpiece during the operation process. Welding is carried out with the rectilinear welds at a direct current by the submerged arc method using consumable electrodes over the layer of flux.

The automatic device is equipped with the control unit and two power supplies (welding rectifiers). Measurement of the wire feed speed and welding speed



is carried out in a stepwise manner using removable gears in geared drives. The welding tractor can be supplied either with the complete set of removable gears or with the gears the mating pairs of which are designed for the wire feed speeds and speed of the welding tractor required by a specific consumer.

The welding tractor consists of the following main parts: carriage including an electric motor, feeding mechanism with a camshaft, traveling gear with chain drives and driving wheels; two welding heads, each including straightening and feeding devices, current contact jaws, electrode position adjustment mechanism providing incline and shifting of a current contact jaw relative to the weld; set of follow-up devices; two hoppers for flux with flux feeders; two mechanisms for arrangement of electrode wires; and control panel.

Advantages of the automatic welding device in comparison with analogs are provided by: improvement of the electric circuit allowing an operator to optimally control feed of the electrode wires and operation of the tractor as a whole; upgrading of the geared motor part, including reinforcement of the place of joining of the motor shaft with input elements of the back axle and feeding mechanism reduction gears; increase in hardness of worm screws; improvement of adjustment of engagement of the worm screw pairs; strengthening of outlet part of the feeding mechanism reduction gear; and utilization of an end coupling preventing sliding in the back axle reduction gear.

METRO CARS OF UKRAINIAN PRODUCTION

A new train consisting of cars produced by OJSC «Kryukovsky Car Building Factory» has been started to run on Syretsko-Pecherskaya line of the Kiev metro since January 2009. It visibly differs from the Russian cars, which are now in operation at the Kiev metro line, in design, style, interior and control systems.

The welded body of a car is made from low-alloy steel 09G2S. Panels of side walls, roof and front walls are made from 2.0–2.5 mm thick sheets of steel 09G2S. Thermal straightening of panel structures is applied



to meet high requirements to flatness. The car frame is made from formed and rolled sections. Bent perforated sections are used in elements of the frame, allowing weight of the body to be reduced by 5 %. New technologies of laser and plasma cutting are used for manufacture of the cars. The operations of bending of the sheets and pipes are carried out by using the CNC equipment. The special profile-bending machine is used to bend the roof elements. In-house production trucks are mounted on the cars. The Factory has a ten-year experience in production of frames of the metro trucks, which are supplied to Kiev and Kharkov metro lines as spare parts. Welding of the frame of trucks and their components is carried out in a mixture of Ar + CO₂ gases. Argon arc treatment of the welds is used for critical components of the trucks.

Preparation of production for serial manufacture of metro cars with a program of delivery of 100 cars per year will be completed in April 2009.

UKRAINIAN-BELARUSSIAN MEETING-PRESENTATION OF THE TECHNOLOGY OF LIVE TISSUE WELDING

On January 15, 2009, a working meeting --- presentation of PWI technology of electric welding of live tissues --- was held in the Minsk City Clinical Emergency Hospital. Chief and leading surgical specialists of Belarus participated in the meeting. S.E. Podpryatov Dr. of Sci. (Med.), A.V. Linchevsky, surgeon, and A.T. Zelnichenko, Director of International Association «Welding», took part in the meeting from the Ukrainian side.

Prof. N.V. Zavada (Chairperson of BelMAPO Emergency Surgery Chair) and S.E. Podpryatov (Leading Surgeon of City Clinical Hospital, Kiev) conducted laparoscopic and open surgery using surgical welding electric coagulator EK-300M1.

Simultaneous video transmission of the operation to meeting participants was performed, which highlighted the following advantages of the technology: fast and accurate separation of tissues, reliable hemostasis, absence of necrotized tissues or foreign bodies in the wound. When electric welding is used, there is no need for surgical sutures, or clips, and consumption of gauze, blood preparations, blood substitutes, as well as hemostatic means is markedly reduced.

Presentations on the experience of application of the unit for live tissue welding in Ukraine were also made in the meeting by A.T. Zelnichenko and S.E. Podpryatov. At subsequent discussion of the operation and presentations Prof. V.N. Zavada, Prof. A.V. Vorobej, Prof. Yu.N. Gain, V.T. Kokhnyuk, Prorector of Belarussian Medical Academy of Post-Diploma Education, Deputy Director of the Republican Scientific-Practical Center of Oncology and Medical Radiology, Assistant Professor S.V. Shakhraj (BGMU Chair of General Surgery), Prof. V.V. Troyan (Chair of Pediatric Surgery of BelMAPO) noted the advantages of the electric welding technology compared to the currently available analogs and expressed interest in application of the above unit in their surgical practice. Assistant Professor I.I. Pikirenya, Chief Surgeon of the Ministry of Health, noted the medical and economic rationality of introduction of the technology in the Republic of Belarus, and fitting of the surgical profile wards with the above unit and tools.

Meeting participants unanimously supported the speakers, and suggested that I.I. Pikirenya apply to the management of the Ministry of Health with the proposal to purchase EK-300 M1 units for the country's hospitals.



After the presentation, I.I. Pikirenya, A.T. Zelnichenko, S.E. Podpryatov, A.V. Linchevsky had a meeting with R.A. Chastnojt, First Deputy Minister of Health, during which the presentation results were discussed and a conclusion was made about the good prospects for application of the unit and tools for live tissue welding in the Republic of Belarus.

It is noted that EK-300 M1 unit, batch-produced by International Association «Welding» under license, has received the hygienic certificate of Belarus Republic, but in order to be used, it has to be registered by the Ministry of Health of Belarus Republic. The rationality of setting up a state program for fitting the surgical wards with the above equipment and training the surgeons was stated.

Dr. A.T. Zelnichenko, PWI